AUTOGENIC PROCESSES ON SUPERCRITICAL SUBMARINE FANS

A Dissertation

Presented to

the Faculty of the Department of Civil and Environmental Engineering

University of Houston

In Partial Fulfillment

of the Requirements for the Degree

Doctor of Philosophy

in Civil Engineering

by

Paul Hamilton

May 2015

AUTOGENIC PROCESSES ON SUPERCRITICAL SUBMARINE FANS

Paul Hamilton

Approved:

Chair of the Committee
Kyle Strom, Associate Professor
Civil and Environmental Engineering

Committee Members:

Keh-Han Wang, Professor
Civil and Environmental Engineering

William Dupre´, Associate Professor
Earth and Atmospheric Sciences

Julia Wellner, Assistant Professor
Earth and Atmospheric Sciences

David Hoyal, Research Geologist
ExxonMobil Upstream Research Company

Suresh K. Khator, Associate Dean
Cullen College of Engineering

Roberto Ballarini, Professor and Chair
Civil and Environmental Engineering

Acknowledgements

I would like to express my sincere appreciation to several people who have made this work possible. Firstly, my thanks to my advisor, Dr. Kyle Strom. He has been an excellent mentor and friend over the past few years and has been instrumental toward compiling this research. I would also like to thank Dr. David Hoyal for interesting discussion and help in the lab especially in considering prior experimental work. I would also like to thank my other committee members, Dr. K.-H. Wang, Dr. Julia Wellner, and Dr. William Dupre', for taking time out to serve on my committee. In addition, my thanks go out to Dr. Juan Fedele for always fruitful discussion on stratified flow and Kevin Bowen for his work in setting up and maintaining the lab facilities. Thanks to ExxonMobil Upstream Research Company for funding this work and making their lab facilities available to me. Last, but certainly not least, I would like to thank my loving wife, Kristine. She has been a source of steadfast support and encouragement over the last few years.

AUTOGENIC PROCESSES ON SUPERCRITICAL SUBMARINE FANS

An Abstract

of a

Dissertation

Presented to

the Faculty of the Department of Civil and Environmental Engineering

University of Houston

In Partial Fulfillment

of the Requirements for the Degree

Doctor of Philosophy

in Civil Engineering

by

Paul Hamilton

May 2015

Abstract

Submarine fans are large landforms typically built on the continental slope and abyssal plain. They are a amalgamation of depositional lobes emplaced over time through avulsion cycles. These type of intermediate scale processes, particularly related to the hydraulic and sediment transport properties, are poorly understood and understudied. This research experimentally explores supercritical submarine avulsion cycles primarily from a hydraulic perspective. To do so, a new methodology was developed that is capable of measuring the layer-averaged hydraulic variables of developing density currents. This methodology was applied to a series of submarine fan experiments to quantify hydraulic and sediment transport properties. The ability to calculate these properties is imperative toward understanding the intrinsic processes that give rise to autogenic avulsion. Fans developed over time through repeated avulsion consisting of channel incision and basinward extension, cessation of channel extension and mouth bar formation, bar aggradation and hydraulic jump initiation, and upstream propagation of the channel-to-lobe transition. The transition from erosion or bypass in the channels to deposition in an expanded-flow region downstream of the channels was most related to deceleration rather than dilution, and a choked-flow condition appeared to cause hydraulic jump initiation. Each avulsion cycle was responsible for an associated lobe deposit. Since hydraulic jumps were common during avulsion cycles, they were used to predict the maximum thickness of the lobe deposits as a function of the upstream flow depth and Froude number. The classic sequent-depth ratio equation was roughly representative of the data trend from the submarine fan experiments. The lobes emplaced by discrete avulsion cycles stacked up over time to form the overall fan. Though each cycle contained elements of both basinward extension and upstream backfilling, the fans showed net progradation at a long-term rate that can be representatively modeled using a mass balance

approach based on sediment supply and equilibrium fan slope. Lastly, the properties of these subaqueous avulsion cycles were compared to similar cycles from alluvial fan experiments. Both systems have supercritical-to-subcritical transition at the channel-to-lobe transition region and detain substantial sediment there. Overall, these two systems appear mechanistically similar.

Table of Contents

List of Figures

List of Tables

Chapter 1. Introduction

1.1 BACKGROUND

Submarine fan systems are spatially expansive distributive channel systems which typically form on the continental rise at the base of the continental slope, and are fed by submarine canyons incised into the continental shelf and slope (fig. 1.1). The sedimentary gravity flows responsible for their development can be broadly classified as either debris flows or turbidity currents. Debris flows are distinguished by their high concentration of sediment within the flow and are not considered in this study. Conversely, turbidity currents are more dilute flows propelled by suspended sediment sustained via turbulence. Submarine fans are of interest geomorphically as they can be the final sink for coarse-grained terrigenous sediments, and they are also of interest within the hydrocarbon industry due to their reservoir potential. As such, open questions regarding trends in spatial and temporal evolution have multifaceted appeal.

The morphology of submarine fan systems is classically divided into an upper, middle, and lower portion (e.g., Normark, 1978) (see fig. 1.1). The upper fan is characterized as a highly dissected region with a system of leveed and/or incised channels (e.g., Normark and Piper, 1969; Deptuck et al., 2003; Posamentier and Kolla, 2003). The middle portion is traditionally considered a transition region where flow depth relative to flow width decreases as the flow partitions into distributive channels and transitions to a net deposition state (e.g., Normark, 1970; Posamentier and Kolla, 2003). The lower fan is the portion of the landform farthest from the apex where the available sediment is predominantly mud and the system is less morphodynamically active (e.g., Normark and Piper, 1972). A delineation into an upper, middle, and lower fan is, by necessity, a simplified morphological description that is nevertheless

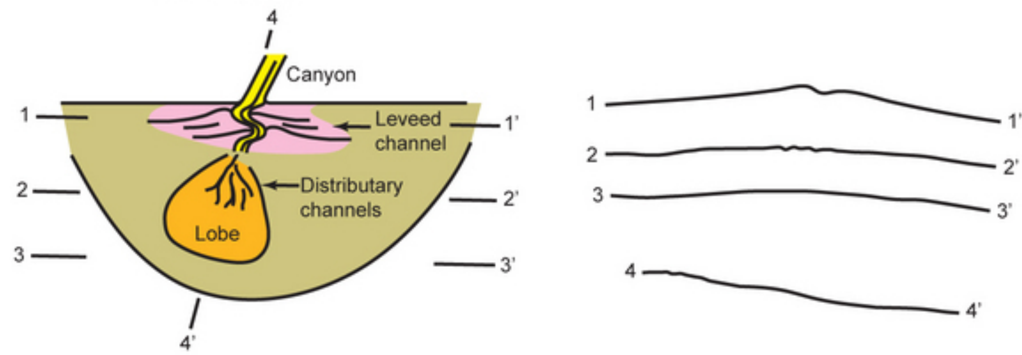

Figure 1.1: Cartoon view of a submarine fan system (after Normark, 1970).

useful in explaining large-scale fan morphology. However, because submarine fan systems appear to be hierarchically organized (e.g., Prelat et al., 2009), there are many architectural elements such as channels, bars, and lobes, that are below the resolution of the proximal, medial, and distal type descriptions (e.g., Deptuck et al., 2008; Straub and Pyles, 2012).

The hierarchy of fan form is a product of a hierarchy of processes. Submarine fan systems, as with other sedimentary systems, evolve over a continuum of spatial and temporal scales from turbulent instabilities and formation of bedforms on the lower end to long-term basin filling processes on the upper end. Diffusion-type models are readily applied to the upper end of these processes (e.g., Paola, 2000). However there are abundant processes intrinsic to dynamic systems, e.g., avulsion cycles, operating below the resolution of these models that generate a high degree of the lithologic heterogeneity. These intermediate scale processes are typified by channel adjustments (e.g., Miall, 1985; Holbrook, 2001) and, for the case of distributary channel systems, interaction with depositional lobes (e.g., Prelat et al., 2009). The evolution of intermediate scale building blocks, and therefore the overall fan, can be characterized as autogenic or allogenic. Autogenic dynamics refer to behavior internally generated by the system, whereas allogenic dynamics are those externally imposed on the system. Though there is no doubt allogenic controls are important in the evolution and preservation of submarine fans and other distributary systems (e.g., Johnson et al., 2001), experiments on submarine fans, deltas, and alluvial fans indicate a high degree of potential autogenic behavior (e.g., Metivier et al., 2005; Hoyal and Sheets, 2009b; Reitz and Jerolmack, 2012).

1.2 AUTOGENIC AVULSION

The sequence of events associated with autogenic avulsion over intermediate time and length scales can be generically described by a system that: (1) forms a distributive channel that extends basinward, (2) channel extension ceases and a mouth bar is deposited, (3) the flow interacts with the mouth bar and the system retreats upstream, and (4) the system reorganizes (e.g., Edmonds et al., 2009; Hoyal and Sheets, 2009b; Hamilton et al., 2013). Hoyal and Sheets (2009a) ran a series of experiments looking at these cycles in supercritical submarine fans where the inferred control is a hydraulic jump at the channel-to-lobe transition. Sediment piles up in the hydraulic jump region, which forces the jump upstream and leads to avulsion and channel re-extension. Their study also revealed that the distance basinward the channels extended is inversely proportional to the underlying slope. They hypothesized that this is due to a shorter distance required to accelerate a given current to a supercritical state on steeper slopes. The role of fan hydraulics, particularly related to super- and subcritical flows, is inferred to be a major part of fan evolution; however hydraulic parameters were not measured to verify these observations and hypotheses.

In the subaerial setting, the alluvial fan study of Hamilton et al. (2013) explored autogenic fan mechanics via hydraulically and morphologically monitored physical experiments. Distributive channels were formed and maintained as a function of grade, i.e., the equilibrium sediment transport condition (Mackin, 1948), and their downstream channel-to-lobe transition was the location of a supercritical-to-subcritical transition that retreated upstream. This channel and lobe behavior is the subaerial supercritical response in the generic cycle outlined above and is shown to differ from the mechanics present in subaerial subcritical distributive systems where the downstream channel-to-lobe transition occurs in a backwater reach modulated by base-level and mouth bar construction (e.g., Hoyal and Sheets, 2009b; Edmonds et al., 2009; Van Dijk et al., 2009; Reitz and Jerolmack, 2012). A common point between the two hydraulic regimes is the reccurrence of autocyclic features. The periodicity of the cycles is governed by simple geometric volumes created by the erosional events at the initiation of a cycle and filled by sediment fed to the lobes via bypass channels (e.g., Reitz and Jerolmack, 2012; Hamilton et al., 2013).

1.3 LOBE GEOMETRY

Each of the autogenic avulsion cycles outlined above has an associated depositional lobe. The geometry of these lobes can be described using a few simple measures such as: maximum length, L_l; maximum width, W_l; maximum thickness, H_l; lobe area, A_l; and lobe volume, V_l (see definition sketch in fig. 1.2). Previous studies considering lobe geometry have typically reported one of these geometric measures as a function of another of these geometric measures, e.g., L_l versus W_l (e.g., Jegou et al., 2008; Saller et al., 2008; Deptuck et al., 2008; Covault and Romans, 2009; Prélat et al., 2010; Fernandez et al., 2014). Geometry has also been cast as a function of confinement. Confinement is considered a binary-type parameter where confined systems have a larger slope in the direction perpendicular to sediment transport than in the direction of sediment transport; the converse is true for unconfined systems (Prélat et al., 2010). Relationships between various geometric properties, along with parameters such as confinement, are potentially specific to particular systems. This approach considers lobes as entities unto themselves rather than as a component in a coupled sedimentary system. Lobe deposition is inseparably linked to distributary channel behavior; channels are the flow and sediment conduit between the sediment

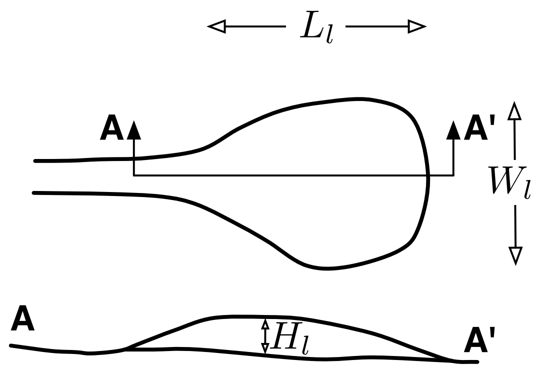

Figure 1.2: Definition diagram of lobe geometry dimensions.

source for the system and the eventual location of deposition. As such the hydraulic properties of the distributary channel should have an effect on the geometry of the deposited lobe. A potentially more universal method of describing lobe geometry is based on the hydraulic and sediment transport processes at work.

1.4 MULTI-AVULSION EVOLUTION

The majority of the preceding discussion is related to the processes associated with individual avulsion cycles and their deposition. Moving up a level of process hierarchy regards how subsequent lobes stack in space and time to form the fan as a whole, and how the evolution of the system impacts hydraulic and sediment transport properties. Compensational stacking, the tendency for deposition to be concentrated at a topographic low, is often invoked as the mechanism for the building of larger hierarchical elements (e.g., Deptuck et al., 2008; Prelat et al., 2009). Straub et al. (2009) developed the compensation index, κ_c, a statistical measure of just how much of a preference a particular system has for filling topographic lows. Straub and Pyles (2012) demonstrated two major findings regarding compensational stacking in submarine fan environments: (1) the tendency for compensational stacking increases with increasing hierarchical scale and (2) compensational stacking increases with increasing distance downstream. The compensation index is potentially most germane to lateral stacking trends as it is based on a transect. Submarine fan systems can also be progradational or retrogradational in time to create complex stacking patterns (e.g., Flint et al., 2011). Much of what we know about the trajectory of submarine fan systems is based on field studies where it may be difficult to disassociate allogenic and autogenic processes (e.g., Flint et al., 2011).

1.5 RESEARCH QUESTIONS AND HYPOTHESES

Herein research questions and hypotheses are posed aimed at better elucidating the interaction between fluid mechanics and morphology of submarine fan systems. They are given by the following:

1. What are the generic hydraulic and sediment transport mechanics associated with autocyclic mesoscale features on submarine fans with supercritical distributaries? This question is investigated by testing three hypotheses: (1) erosional channels incise into the ambient bathymetry and cease extension due to reduced sediment transport capacity from reduced velocity and density; (2) mouth bars aggrade over time to choke the flow and initiate hydraulic jumps; and (3) hydraulic jumps form at the channel-to-lobe transition and retreat upstream over time.

2. What is the relationship between channel hydraulic properties and depositional lobe geometries in submarine fan systems with supercritical distributaries? Are they linked? The hypothesis for this question is that the incoming densimetric Froude number will be a primary hydraulic control on the geometry of lobe deposits associated with individual avulsion cycles due to the observed hydraulic jumps. This should results in two relationships: a higher Froude number will lead to more elongate (higher L_l/W_l) and relatively thicker (higher H_l/h) deposits.

3. How do submarine fans evolve over several avulsion cycles and what is the evolution of hydraulic properties? The hypothesis is that the submarine fans will be progradational over time due to the hydraulic variables trending toward an equilibrium state. It is further hypothesized that the supercritical fan systems will not build strictly compensational due to supercritical flows receiving information only from the upstream direction.

4. How do the processes and mechanics associated with supercritical avulsion compare between subaerial and subaqueous environments? Answering this question will help to better understand the relative importance of ambient fluid density, i.e., subaerial versus subaqueous, and hydraulic regime, i.e., subcritical versus supercritical. The hypothesis is that avulsion cycles in the two environments will be more similar than different due to both having supercritical flow.

A set of autogenic submarine fan experiments were run to investigate the above questions. Autogenic systems were used such that the intrinsic system behaviors were isolated absent external modification. The experiments were instrumented to collect hydraulic and bathymetric data during their evolution. A description of the experiments, along with the data collection and analysis schemes, is presented in Chapter 2. A major component toward exploring the research questions is predicated on quantifying the flow velocity of the system. Since there was no available method to use, one needed to be developed. A brief explanation of the new methodology is included with the rest of the study methods in Chapter 2. The complete details of the methodology is presented separately in Chapter 3 (published as Hamilton et al. (2015c)). With the required methodology developed, the balance of this dissertation is dedicated to answering the research questions posed. The mechanics of supercritical autogenic avulsion cycles (question one) are considered in Chapter 4. Chapter 5 explores potential links between the distributary channel hydraulics and the geometry of lobes they emplace (question two). While questions one and two are mostly related to individual avulsion cycle mechanics and associated properties, question three explores the evolution of submarine fans over several avulsion cycles (Chapter 6). Question four is considered in Chapter 7 where the subaqueous cycles studied in this research are compared to data from their subaerial counterparts. Lastly, the conclusions from this work are presented in Chapter 8.

Chapter 2. Methods

2.1 OVERVIEW

To test the hypotheses, we conducted two series of laboratory experiments in which the hydraulics, sediment transport characteristics, and morphologic development of self-formed channel and lobe systems were measured in space and time. Experiments are a convenient way to observe morphodynamic processes since the time-scales for change are drastically shortened compared to their natural counterparts, boundary conditions can be dictated, and the environment can be carefully instrumented. In studying the spatial distribution of sedimentary bodies, submarine fan experimentalists have generally taken one of two approaches: (1) experimentally created turbidity currents with a range of sediment sizes (Luthi, 1981; Parsons et al., 2002; Yu et al., 2006; Cantelli et al., 2011; Fernandez et al., 2014) or (2) used saline underflows with plastic sediment (Metivier et al., 2005; Hoyal and Sheets, 2009a; Weill et al., 2014). Turbidity current experiments have the advantage of using the same materials as their natural counterparts and as such can replicate grain size patterns and deposition from suspension. However, they are difficult to sustain for long periods of time experimentally and are susceptible to becoming hyper-concentrated at small scales. Conversely, saline flows use dissolved salt to drive the flow and replicate the fluid mechanical properties of turbulently suspended sediment in turbidity currents. They can be easily sustained for long periods of time experimentally and can make features similar to those observed in nature despite bedload being the primary mode of transport (Metivier et al., 2005). The saline underflow and plastic sediment approach was used in this study with steady-state feeding at the boundary to isolate the intrinsic autogenic morphodynamics.

2.2 EXPERIMENTAL SETUP

The experimental domain consisted of a 2.1 m long by 2.1 m wide sloping plate set at an angle of S_p that led to an equally wide by 1.1 m long horizontal plate. This environment was set within a larger 5 m long by 3 m wide by 1 m deep tank (fig. 2.1). A mixture of dyed brine solution and sediment was introduced to the experimental domain from a mixing box with the underflow coming over a broad crested weir. After exiting the mixing box, flows developed over a pre-graded 4.1 cm thick sediment bed covering the entirety of the experimental domain. The sediment used in the experiments consisted of a uniform mixture of 0.20-0.25 mm (#60-#80 sieve) crushed melamine plastic with a specific gravity of 1.55.

The independent variables for each experiment were: plate slope, S_p; initial brine discharge to the mixing box, Q_{in}; sediment supply, Q_s; and initial density excess, $\Delta\rho_{in}$. Q_{in} was the same for all experiments at $Q_{in} = 4.58$ L/min. The combinations of the other boundary conditions, S_p, $\Delta\rho_{in}$, and Q_s, for the various experiments are listed in table 2.1. We selected these boundary conditions because: (1) they produced the channel and lobe mechanics of interest in this study and (2) they did not produce, or produced very few, bedforms.

2.3 DATA COLLECTION METHODS

The experimental domain was instrumented with: (1) an overhead camera (Nikon D90), (2) a second overhead camera (SPOT Insight), (3) a PME micro conductivity and temperature instrument, and (4) a laser scanner with a SICK Ranger E50 3D camera used to measure the reflection of a laser line projected on the deposit. These instruments were used to collect the raw data needed to define the hydraulic properties of velocity, depth, and excess density, and the temporal and spatial changes of the fan bathymetry. The measured hydraulics and changes in the morphology were

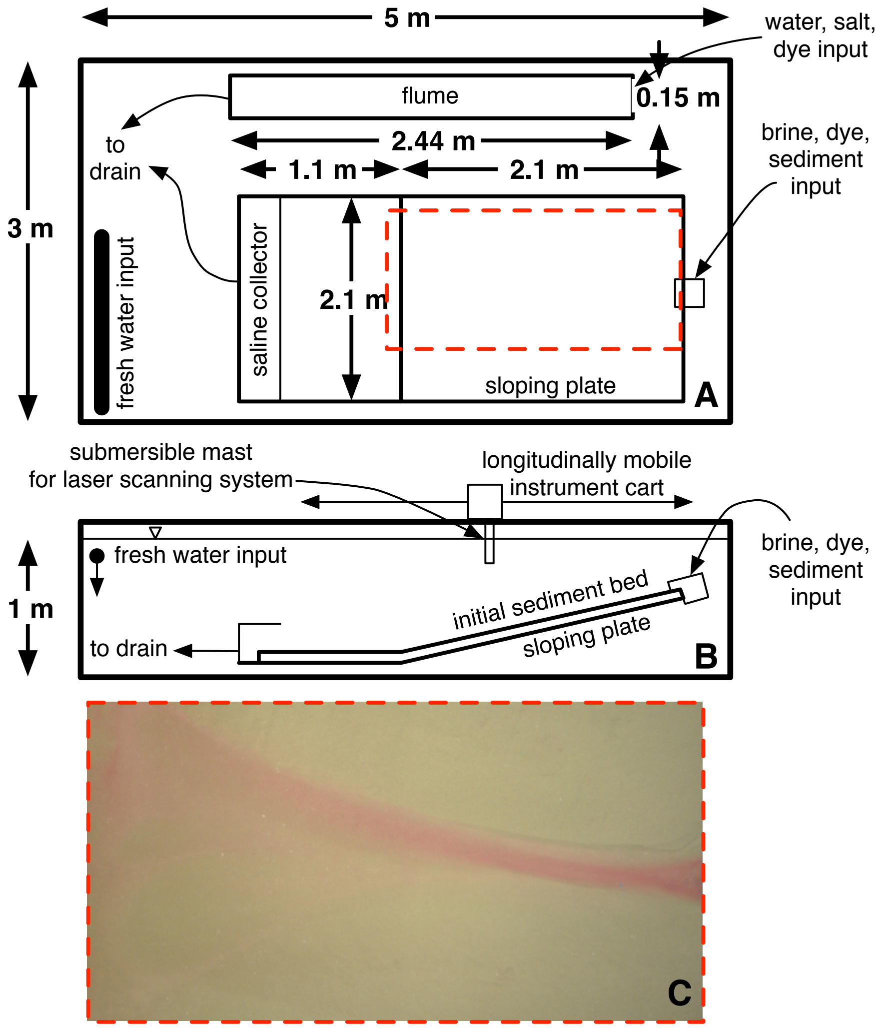

Figure 2.1: Schematic representation of the experimental environment: (A) plan view, (B) profile view, and (C) example submarine fan overhead image.

then coupled with sediment transport calculations to test the three study hypotheses.

The overhead camera Nikon D90 was used to collect images at a frequency of once per minute to monitor the overall morphologic evolution of the fan system. The second overhead camera was used to capture images for computing density current velocity. These images were taken as a sequence of 300 images spaced 0.2 sec apart. Image sequences were collected at minimum once every 20 minutes and more frequently during periods of high morphodynamic activity. The conductivity probe was used to verify the density current concentration at the inlet at least once every 20

Table 2.1: Experimental boundary conditions for set A and set B. The listed parameters are: imposed plate slope, S_p; excess density into the mixing box, $\Delta\rho_{in}$; and sediment discharge, Q_s.

Run	S_p [-]	$\Delta\rho_{in}$ [kg/m^3]	Q_s [mm^3/sec]	Run	S_p [-]	$\Delta\rho_{in}$ [kg/m^3]	Q_s [mm^3/sec]
Fan01-A	0.247	90	1840	Fan01-B	0.107	140	631
Fan02-A	0.247	120	1840	Fan02-B	0.138	140	896
Fan03-A	0.247	134	1840	Fan03-B	0.156	135	820
Fan04-A	0.232	90	1840	Fan04-B	0.171	130	852
Fan05-A	0.232	120	1840	Fan05-B	0.181	125	883
Fan06-A	0.232	134	1840	Fan06-B	0.193	120	1053
Fan07-A	0.201	90	1840	Fan07-B	0.215	120	1262
Fan08-A	0.201	120	1840	Fan08-B	0.228	120	1388
Fan09-A	0.201	134	1840	Fan09-B	0.251	110	959
Fan10-A	0.201	134	1840	Fan10-B	0.171	130	852
Fan11-A	0.201	134	1840				

minutes. These measurements were to quantify the dilution within the mixing box before the current entered the experimental domain and therefore measure the actual boundary condition for the experiment. The laser scanner was used to collect bathymetry data following velocity data collection. After capturing a series of images for velocity measurement, the experiment was paused and the scanning system used to collect bathymetry data over the entire domain. This bathymetry data was used to measure the geometry data of the lobes deposited throughout the experiments. Finally, because a density contrast can also be caused by a temperature gradient, the temperature of the inlet water and the ambient water were monitored throughout the experiments every 20 minutes. The largest difference in temperature observed was 0.7 °C, which results in a density difference of 0.5 kg/m^3 — a value substantially less than the imposed saline density difference of $\geq$ 80 kg/m^3 at the inlet. Temperature differences are therefore neglected.

2.4 DATA ANALYSIS METHODS

2.4.1 Hydraulic Variables

Full details regarding the development and application of the methodology used to characterize current velocity U, current thickness h, and current excess density $\Delta\rho$ ($\Delta\rho = \rho_f - \rho_a$ where ρ_f is the current density and ρ_a is the ambient fluid density), are outlined in Chapter 3 (Hamilton et al., 2015c); a summary follows. The density current velocity field was measured using overhead images taken from the SPOT Insight camera and a particle tracking velocimetry (PTV) algorithm (Brevis et al., 2011). PTV is an image-based technique where the displacement of tracers confined within the flow are measured between images separated by a known amount of time. This gives a velocity data point at the location of all tracers. The velocity was then cross-sectionally averaged to get flow velocity as a function of downstream distance. Flow width, W, was measured from orthorectified (Fujita et al., 1998; Hauet et al., 2008) overhead images of the dyed flow. Given the velocity and width along the flow path, the layer-thickness and excess density were calculated by solving the one-dimensional volume and mass conservation equations for this application,

$$\frac{d}{dx}(UhW) = e_w UW \text{ and} \tag{2.1}$$

$$\frac{d}{dx}(U\frac{\Delta\rho}{\rho_a}hW) = 0, \tag{2.2}$$

where x is the along channel coordinate and e_w is the entrainment coefficient given by Parker et al. (1987) as

$$e_w = \frac{0.075}{(1 + 718F_r^{-4.8})^{0.5}}. \tag{2.3}$$

In the denominator of equation 3.6 is the densimetric Froude number (F_r), a non-dimensional hydraulic variable, given by

$$F_r = \frac{U}{\sqrt{g'h}} = \frac{1}{R_i^{1/2}}, \tag{2.4}$$

where R_i is the Richardson number, $g' = g\Delta\rho/\rho_f$ is the modified gravitational acceleration due to the Boussinesq approximation, and ρ_f is the density of the underflow. The Froude number is an important dimensionless number in describing flow mechanics, as it dictates the propagation of internal or interfacial waves within a flow. For the case in which the inertial forces exceed the gravitational forces ($F_r > 1$), the flow is termed supercritical and waves are propagated solely downstream. If the converse is true ($F_r < 1$), the flow is subcritical and waves are propagated both upstream and downstream. Another important non-dimensional number is the Reynolds number given by

$$R_e = \frac{Uh}{\nu}, \tag{2.5}$$

where ν is the kinematic viscosity. The Reynolds number is the ratio of inertial forces to viscous forces and describes whether the flow is laminar ($R_e < 575$), transitional ($575 < R_e < 1000$), or turbulent ($R_e \geq 1000$) (Lajeunesse et al., 2010).

2.4.2 Sediment Transport

Sediment transport conditions for the experiments were calculated from the measured hydraulic variables and a bed-shear-stress-based bedload transport equation. The bed-shear stress, τ, was calculated using

$$\tau = \rho_f C_f U^2, \tag{2.6}$$

where C_f is the friction coefficient. C_f was empirically estimated to be 0.02 for our shallow density currents flowing over the crushed plastic sediment. This value was obtained by fitting the rough-wall log law to the vertical velocity profile data of Hamilton et al. (2015c) in the inner region of the current while letting shear velocity, u_*, be a regression parameter (Clauser, 1956). By definition, $C_f = (u_*/U)^2$.

The bed-shear stress was then used to calculate the non-dimensional Shields parameter, τ^* as

$$\tau^* = \frac{\tau}{(\rho_s - \rho_f) g d_c}, \tag{2.7}$$

where ρ_s is the density of the sediment and d_c is the characteristic grain size. The dimensionless bedload transport number, q^*, can then be calculated according to a power law relationship taking the generic form

$$q^* = \alpha \left(\tau^* - \tau^*_{cr}\right)^{\beta}, \tag{2.8}$$

where τ^*_{cr} is the critical Shields parameter associated with incipient motion and α and β are coefficients determined by the sediment transport model selected. The dimensionless bedload transport number is given by

$$q^* = \frac{q_t}{\sqrt{R_s g d_c} d_c}, \tag{2.9}$$

where $R_s = (\rho_s - \rho_f)/\rho_f$ is the submerged specific gravity of the sediment and q_t is the sediment transport rate per unit width with total sediment transport given as $Q_t = q_t W$. Here we use the Wong and Parker (2006) revision of the classic Meyer-Peter and Müller (1948) method to calculate bedload transport rates. As such the model parameters in equation 2.8 are $\alpha = 3.97$, $\beta = 1.50$, and $\tau^*_{cr} = 0.0495$. It is worth noting that the Wong and Parker (2006) method is based on steady-state open channel flows and not explicitly for density currents. However, the mechanics of bedload transport should be the same regardless of setting, and the transport relationships (equations 2.7-2.9) include all the parameters that are different between the two settings, e.g., flow density, sediment density, and sediment size. Furthermore, Sequeiros et al. (2010a) showed experimentally that the Wong and Parker (2006) method is reasonable for bedload transport in density and turbidity currents.

Equations 2.6-2.9 can be combined to obtain a relationship for total sediment transport,

$$Q_t = \frac{\alpha U^3 C_f^{3/2} \rho_f W}{(\rho_s - \rho_f) g} = \frac{\alpha U^3 C_f^{3/2} W}{R_s g}, \tag{2.10}$$

which is subject to an assumption of sediment transport well above the incipient threshold, i.e., $\tau^* \gg \tau^*_{cr}$ and therefore $(\tau^* - \tau^*_{cr}) \approx \tau^*$, and also incorporates the Wong and Parker (2006) value of $\beta = 3/2$. α and C_f are assumed constant (though they could be slightly variable), and ρ_s and g are constant. Since ρ_s is constant, ρ_f is the important variable in setting R_s.

One final non-dimensional variable related to sediment transport was calculated for the experiments. The Rouse number is given by

$$z_* = \frac{w_s}{\kappa u_*}, \tag{2.11}$$

where w_s is the sediment settling velocity, calculated using the equation of Ferguson and Church (2004), and $\kappa = 0.41$ is the von Karman constant. In general, z_* is helpful in defining the degree of vertical stratification of sediment in suspension. For these experiments, we use z_* as a measure of how much sediment is transported in suspension versus bedload (Greimann et al., 2008).

2.4.3 Hydraulic Theory

Specific Energy and Conditions for Choke

One of our hypotheses regarding fan behavior is that the vertical growth of a mouth bar can “choke” a supercritical density current and force a hydraulic jump to form just upstream of the bar. Identification of the critical thickness of this mouth bar can be obtained through application of specific energy principles. The specific energy, E, for a density current in a rectangular channel is given by

$$E = h + \frac{U^2}{2g'} = h + \frac{q^2}{2g'h^2}, \tag{2.12}$$

where q is the discharge per unit width. When no change in the bed elevation is present, and the flow is assumed frictionless over a short distance from section 1 to 2, conservation of energy implies that E remain constant, or $E_1 = E_2$. However, if the bed elevation at section 2 is higher than that at section 1, then energy conservation is expressed as, $E_1 = E_2 + \Delta\eta$ where $\Delta\eta$ is the height of a step in bed elevation. The form of E (eq. 2.12) dictates that there is an ultimate minimum value that E can obtain for any fixed value of q and g'. This minimum value can easily be shown to be the specific energy associated with critical flow, E_{cr} (at $F_r = 1$). The existence of a minimum value of E for a given q and g' therefore sets a bound on the maximum change in elevation that can be sustained without altering the flow state at section one. This maximum height is

$$\Delta\eta_{max} = E_1 - E_{cr}. \tag{2.13}$$

For rectangular channels, the critical specific energy is $E_{cr} = 3/2h_{cr}$ where $h_{cr} = (q^2/g')^{1/3}$ is the critical depth. If a step in elevation is larger than $\Delta\eta_{max}$, the flow will become choked and need to adjust to traverse the obstacle. Normalizing $\Delta\eta_{max}$

by the upstream flow thickness gives

$$\frac{\Delta\eta_{max}}{h_1} = 1 + \frac{F_r^2}{2} - \frac{3}{2}F_r^{2/3}. \qquad (2.14)$$

Choked flow initiates a hydraulic jump in supercritical flows.

Hydraulic Jump

The second hydraulic feature associated with supercritical submarine fan avulsion cycles is a hydraulic jump. Hydraulic jumps are a rapidly varied flow phenomenon marking the transition from supercritical to subcritical flow. This physically includes a sudden thickening and slowing of the current. The ratio between the downstream and upstream flow depth on either side of a hydraulic jump, h_2 and h_1 respectively, is known as the sequent depth ratio, h_2/h_1. For the "classic" hydraulic jump, i.e., one occurring in a horizontal rectangular open-channel, the sequent depth ratio is (Chow, 1959)

$$\frac{h_2}{h_1} = \frac{\sqrt{1+8F_r^2} - 1}{2}. \qquad (2.15)$$

This equation comes from conservation of momentum between the upstream and downstream sections.

Critical Slope

Another potential scenario that can give rise to a hydraulic jump is a transition in bed slope from one that is greater than the critical slope, S_{cr}, to one that is less than S_{cr} (Chow, 1959; Komar, 1971; Garcia and Parker, 1989). S_{cr} is defined as the slope at which normal flow conditions match the critical conditions ($F_r = R_i = 1$). To find S_{cr} for a density current, we use the Ellison and Turner (1959) layer-averaged equations and assume top-hat vertical velocity and density profiles. The momentum equation combined with the entrainment equation formulated for downstream variation in Richardson number within the channelized portion of a flow is given as

$$\frac{h}{3R_i}\frac{dR_i}{dx} = \frac{(1 + 1/2R_i)e_w - R_iS + C_f}{1 - R_i}. \tag{2.16}$$

To get to the normal Richardson number, R_{in}, i.e., the R_i in which normal flow conditions persist in the downstream direction, $dR_i/dx = 0$ is imposed leading to

$$R_{in} = \frac{e_w + C_f}{S - 1/2e_w}. \tag{2.17}$$

From here the critical slope, S_{cr}, can be calculated by setting R_{in} equal to unity resulting in

$$S_{cr} = C_f + \frac{3}{2}e_w(1), \tag{2.18}$$

where $e_w(1)$ represents the entrainment coefficient for $R_i = 1$. Using equation 3.6 for e_w and our measured C_f gives a critical slope of $S_{cr} = 0.024$.

2.5 EXPERIMENTAL SCALING CONSIDERATIONS

These experiments were not scaled to any particular natural prototype system but were considered miniature submarine fans in their own right (Hooke, 1968; Paola et al., 2009). A fully scaled model requires geometric, kinematic, and dynamic similarity with a prototype system. As a practical matter this is impossible as the model system would be sufficiently large as to nullify the benefits of using the experimental model in the first place. Geomorphic experiments, despite a large difference in scale with their natural counterparts, have been remarkably effective in emulating natural landscape processes (Paola et al., 2009; Kleinhans et al., 2014). Though our experiments are not strictly scaled, there is value in considering potential scaling relationships between these experiments and natural settings.

As a preliminary note toward comparing a prototype (natural) system and model (laboratory) system, the $(P)_p$ notation corresponds the prototype values of some property P and $(P)_m$ to the model values; $\lambda_P = (P)_p/(P)_m$ will serve as a scaling ratio for the various properties. Our approach is similar to that of other authors considering experimental stratified flows in that it is based on similarity in densimetric Froude number (e.g., Kostic et al., 2002; Yu et al., 2006; Cantelli et al., 2011). The foundation of densimetric Froude number scaling is that $\lambda_{Fr} = (Fr)_p/(Fr)_m = 1$. Other requisite ratios include one for horizontal length, $\lambda_l = (L)_p/(L)_m$, one for vertical length, $\lambda_h = (h)_p/(h)_m$, and one for the density ratio $\Delta\rho/\rho$, $\lambda_\rho = (\Delta\rho/\rho)_p/(\Delta\rho/\rho)_m$. Other studies (e.g., Yu et al., 2006; Cantelli et al., 2011) do not consider the density ratio between prototype and model as their studies use turbidity currents where the prototype and model have similar densities. This is a good assumption for these studies as an amplified concentration in the lab could lead to rheological consequences that are absent in the saline underflows used in this study.

From the scaling ratios established above, we can determine scaling for velocity as $(U)_p = (U)_m(\lambda_\rho\lambda_h)^{1/2}$ and discharge as $(Q)_p = (Q)_m\lambda_\rho^{1/2}\lambda_h^{3/2}\lambda_l$. To extend this analysis from the flow to the sediment bed we assume $\lambda_{\tau^*} = (\tau^*)_p/(\tau^*)_m = 1$ and take $C_f \propto h^{-1/6}$ (García, 2008) which makes $(C_f)_p = (C_f)_m\lambda_h^{-1/6}$. This allows scaling of the sediment size according to $(d)_p = (d)_m\lambda_h^{5/6}\lambda_\rho\lambda_{R_s}^{-1}$ where $\lambda_{R_s} = (R_s)_p/(R_s)_m$. For a comparison between natural silica sand and the crushed melamine plastic used in this study $\lambda_{R_s} \approx 3$. It is of note that other studies (e.g., Yu et al., 2006; Cantelli et al., 2011) based their grain size relationships on the fall velocity of the sediment in suspension whereas here it is based on similarity in τ^*. This makes more sense for this study given the use of dissolved salt as the source of density excess and bedload as the dominant mode of sediment transport.

2.6 ONE-DIMENSIONAL LATERALLY EXPANDING DENSITY CURRENT MODEL

To aid in the data analysis and hypothesis testing, we solve the laterally unconstrained, one-dimensional, steady, layer-averaged governing equations for mass, volume, and momentum conservation along both a channelized section of the flow and in an expansion. In the formulation of the equations, we use the Boussinesq approximation and top-hat flow and scalar profiles. The form and solution procedure follow that of Hetland (2010) and Strom (2014) for a buoyant supercritical river mouth discharge with modifications made to account for a density flow down a slope with bottom friction (see the Appendix for details). Closure for the system of equations is provided through a resistance equation for bed friction (eq. 2.6) specific width and bottom elevation profiles or functions, and the entrainment function (eq. 3.6). Sediment transport and bed evolution are not included in the model. This omission limits the analysis to a snapshot in time for a particular bed and width profile. Under the stated assumptions, the governing equations reduce to the following system of ordinary differential equations:

$$\frac{d\Delta\rho}{dx} = -\Delta\rho\frac{u_e}{Uh}, \tag{2.19}$$

$$\frac{dW}{dx} = 2\tan\alpha_w, \tag{2.20}$$

$$\frac{dU}{dx} = \frac{U}{1-R_i}\left[\left(1+\frac{R_i}{2}\right)\frac{1}{\Delta\rho}\frac{d\Delta\rho}{dx} + R_i\left(\frac{1}{W}\right)\frac{dW}{dx} + \left(R_iS - C_f\right)\frac{1}{h}\right], \text{ and} \tag{2.21}$$

$$\frac{dh}{dx} = -h\left(\frac{1}{\Delta\rho}\frac{d\Delta\rho}{dx} + \frac{1}{W}\frac{dW}{dx} + \frac{1}{U}\frac{dU}{dx}\right), \tag{2.22}$$

where u_e is the entrainment velocity given as $u_e = e_wU$ and α_w is the expansion half angle. These equations were solved using the fourth order Runge-Kutta method. The flow variables were then used to calculate sediment transport rates from equations

2.7-2.9. The boundary conditions for this model are: initial Froude number, initial discharge, initial width, initial density difference, the bed slope, the friction factor, and the expansion half angle. Also used to calculate sediment transport rate were the sediment size, submerged specific gravity, and volumetric supply rate. Calculations from this model are shown in Chapter 4 to help contextualize observed fan behaviors and answer questions that arise from analysis of the data.

2.7 AVAILABLE LOBE GEOMETRY DATA IN THE LITERATURE

Our physical data collection was limited to measurements taken during submarine fan experiments. However, with a study of this sort it is important to consider other available geometric data and how they relate to our experimental data. Fortunately, there are several studies that have considered lobe geometry (e.g., Jegou et al., 2008; Saller et al., 2008; Deptuck et al., 2008; Covault and Romans, 2009; Prélat et al., 2010; Fernandez et al., 2014). We used data from the following studies for comparison with our data: Fernandez et al. (2014), Deptuck et al. (2008), and Covault and Romans (2009). Fernandez et al. (2014) is an experimental study that offers a comparison with a system of similar spatial scale though with two principle differences: (1) their study used turbidity currents instead of the saline density currents we used and (2) their study sustained subcritical flow ($F_r \approx 0.5$). The other data sets are from natural settings that we consider to roughly be natural prototypes for our experimental fans. Deptuck et al. (2008) is a study of the Golo Fan system off the eastern coast of Corsica and Covault and Romans (2009) a study of the California Borderland. These are used to make comparison to the natural systems our experiments simulate.

The next chapter contains the full details regarding the development of the hydraulic data compilation methodology. For readers interested in proceeding directly to the results, Chapter 3 can be skipped without loss of continuity.

Chapter 3. Non-invasive Methods for Hydraulic Characterization of Density Currents with Application to Submarine Fan Experiments

3.1 INTRODUCTION

Dense underflows are a stratified flow phenomenon established when there exists a density contrast between an ambient fluid and an underlying fluid of greater density. Density stratification of this kind can be derived from a difference in salinity, temperature, or suspended sediment concentration. When sustained by suspended sediment, such density currents are called turbidity currents and can form in freshwater lakes and reservoirs as well as in shallow and deep marine settings (Kneller and Buckee, 2000). They supply sediment and rework deposits and channel distributaries to form, maintain, and alter subaqueous fans. The morphodynamics of these systems are of interest as they represent the ultimate sink for most terrigenous sediments, and as such, are important in understanding landscape evolution. In addition, they impact the sedimentation and sediment routing patterns in reservoirs, and older deposits can contain significant hydrocarbon resources.

The large spatial extent of submarine fans and the sporadic and violent nature of turbidity currents at the field scale has meant that much of what we know about such system dynamics comes from laboratory experiments. Even so, capturing the full dynamics of the system can be challenging and has led investigations to focus primarily either on the gravity current structure within laterally confined flumes (e.g., Middleton, 1966; Parker et al., 1986, 1987; García and Parsons, 1996; Martin and García, 2009; Sequeiros et al., 2010b) or on the deposits in laterally unconstrained settings (e.g., Luthi, 1981; Yu et al., 2006; Hoyal and Sheets, 2009a; Cantelli et al., 2011). However, submarine fans are coupled fluid and sediment systems wherein changes in the fluid structure impact the deposition and erosion patterns at the boundary, which then feedback to alter the fluid structure of the current. The importance of the intertwined fluid and sediment dynamics in laterally confined open channel flows at the bedform scale have long been known and studied experimentally (e.g., Kennedy, 1969). But, such feedbacks in laterally unconstrained systems at larger spatial scales have also more recently been recognized as a key component in the system dynamics of developing alluvial fans and deltas (e.g., Van Dijk et al., 2009; Reitz and Jerolmack, 2012; Hamilton et al., 2013).

Characterization of a sedimentary system morphodynamics requires measurement of both the change in topography and channel hydraulics in space and time. Methods for hydraulic characterization of evolving channel and fan systems exist for subaerial alluvial fans and deltas (e.g., Hamilton et al., 2013). However, as of yet, no method exists for hydraulically characterizing flows in submarine fan experiments. The objective of this paper is to present a new technique for remotely obtaining the layer-averaged hydraulics of thin saline density currents that, over time, build laterally unconstrained submarine channel and lobe complexes through internal system morphodynamics.

3.2 METHOD DEVELOPMENT OVERVIEW

Through internal morphodynamics, the fan system creates channels and terminal lobate deposits that migrate, aggrade, and degrade with time to create a fan surface. To characterize the hydraulics of the system so that they can be linked with deposition and erosion processes, one needs to know, at a minimum, the layer-averaged flow velocity, excess density, and depth along the length of the channel with time.

Several factors complicate the measurement of hydraulic properties in these flows. A major challenge is that the flows are thin and the channels are actively manipulating their boundaries. This makes probe-based measurements less than ideal, since one would need to constantly reposition the probes just to make measurements of velocity and depth at the same relative location down channel, and no spatial trends could be captured. Because of this, image-based techniques capable of capturing spatial information remotely are far better suited for such environments.

In alluvial fan experiments, Hamilton et al. (2013) were able to characterize the depth and velocity in actively evolving shallow distributaries using image-based methods. For depth, they used an apparent dye-intensity method (e.g., Gran and Paola, 2001; Carbonneau et al., 2006), and velocity was obtained using large-scale particle image velocimetry (LSPIV) (Muste et al., 2008). While these techniques work well for subaerial flows, neither method can be directly applied to subaqueous density currents due to the soft density gradient between the current and the overlying water. For example, the dye-intensity method for depth relies on a fixed dye concentration throughout the current so that a particular color intensity can be linked to a particular depth. However, in density flows, entrainment and mixing of the overlying ambient water into the density flow means that the concentration of any dye injected at the inlet would change as a function of distance and current velocity, making it impossible to link an overhead color intensity with a particular depth. Likewise, the LSPIV method relies on a sharp density contact at the free surface between air and water to fix buoyant particles to a particular plane in the flow, i.e., the free-surface. In density flows, a density gradient of that magnitude does not exist, and tracer particles must be neutrally buoyant to remain within the density current. Furthermore, LSPIV relies on an abundance of particles attached the free surface that are well lit with ambient lighting. Obtaining such conditions with neutrally buoyant particles is not possible without the introduction of a laser-generated light sheet. The need for a laser generated light sheet would restrict the field of view that could be captured and would make positioning of the light sheets difficult since the channels actively migrate.

Instead of using LSPIV or PIV to characterize density current velocity, we use Particle Tracking Velocimetry (PTV) and neutrally buoyant tracers. PTV is similar to LSPIV in that both use the time between subsequent images to calculate velocity based on tracer displacement; however PTV uses the measured displacement of individual tracers between sequent images as opposed to a clump of tracers. This allows for a drastic reduction in the number of tracers needed relative to LSPIV or classic PIV methods, which is a major advantage given that introducing a large number of tracers to the flow would be troublesome. As with LSPIV, the PTV method uses standard consumer-grade cameras with ambient lighting to image a large field of view. To obtain depth and excess density, we use simple 1D volume and mass conservation principles along with the measured channel width profiles from the overhead cameras, layer-averaged velocity from the PTV analysis, and boundary conditions at the inlet.

To use the PTV method, a link must be made between the tracer-measured velocity and the layer-averaged current velocity. The section below discusses a small flume experiment that was designed and conducted to determine if neutrally buoyant tracers released in a density current would go to a characteristic location in the vertical and whether or not a reliable calibration relationship could be found between tracer velocity and layer-averaged velocity. Following this, we present the details for the calculation of flow depth and excess density and present an example integrating the techniques using data from an experimental fan.

3.3 VELOCITY MEASUREMENT

3.3.1 Methodology

PTV is a non-invasive velocity measurement method in which particles within the flow field are tracked in subsequent images separated by a known amount of time. In our PTV implementation, a series of color images were captured under volume illumination conditions from overhead the tank and prepared for analysis by extracting the color band that resulted in the highest contrast between the tracers and the surrounding fluid. The isolated band for each of the images in the series was subtracted from an image without tracers to remove the background. A threshold was then applied to the result of the image subtraction to give a binary indicator of tracer/non-tracer throughout the image. The resulting sequence of tracer locations was then run through the PTV algorithm of Brevis et al. (2011) to calculate the displacement of each tracer. Image coordinates were associated with their physical locations via orthorectification procedure (Fujita et al., 1998; Hauet et al., 2008). From there, knowing the time interval between subsequent images within the series, a velocity field with both magnitude and direction can be mapped over the traced area. This gives $u_M = u_M(x, y)$ where u_M is the velocity measured by this PTV procedure.

To use this method in density currents, a suitable tracer needed to be identified. Unlike open channel flows, which can be traced with anything on the free-surface, density currents require a tracer confined to the dense undercurrent. Tracers for this study were small squares (approximately 5mm x 5mm) cut from biodegradable flagging tape soaked in a saline solution matching the density of the inlet water to make them nearly neutrally buoyant.

Beyond a neutrally buoyant tracer, the vertical structure of density currents, which is complicated by interfacial mixing, necessitates a set of small-scale flume experiments to calibrate the PTV measurements (u_M) to the actual velocity profile, i.e., peak (u_p) and layer-averaged (U) velocities. Tracers were added to the current in a calibration flume and observed by a series of overhead images, images from the side, and velocity and concentration profiles such that the characteristic peak and layer-averaged flow conditions could be calculated.

3.3.2 Flume Experiments

A set of 41 flume experiments were run across a range of conditions similar to those anticipated in the submarine fan experiments. The 2.44m long, 0.15m wide, and 0.20m tall flume was set at a uniform slope inside the larger 5m x 3m x 1m tank (fig. 2.1). The upstream boundary condition consisted of a broad-crested weir while the bed of the flume was lined with an immobile layer of uniform plastic sediment with diameter 0.20mm - 0.25mm to simulate the roughness in the application fan experiments. Independent variables for the flume experiments were discharge, the inlet specific gravity of the denser fluid, and bed slope which each had respective ranges of 3.79-7.57 L/min (1.0-2.0 gpm), 1.07-1.15, and 0.002-0.201.

Underflows were seeded with tracers near the inlet and observed at a control section 1.25m downstream where the density current body had become fully developed and steady long after the initial head of the current had past. The control section was instrumented with: (1) a camera mounted overhead of the experiment above the ambient water free surface, (2) a video camera mounted to the side of the tank viewing a profile of the current, (3) a Sontek MicroADV, and (4) a PME micro-scale conductivity probe.

The images taken from overhead were used to emulate images which would be collected in submarine fan experiments where it would not be possible to view the currents from the side. The side-looking camera was used here to examine the elevation of tracer transport within the vertical flow profile. This is an important aspect of the exercise given that velocity and concentration are non-uniform in the vertical direction.

The ADV was used to collect the velocity profile at the control section. Data were collected at 25 Hz over a time-averaging window of 180 sec at each point in the profile. The data was post processed using WinADV (Wahl, 2000) where data points with correlations (COR) of less than 70 or a signal-to-noise ratio (SNR) of less than 15 were excluded from the filtered time-series. The data were also phase-spaced despiked using the approach of Goring and Nikora (2002).

The conductivity probe, calibrated per manufacturer specification, was used to measure fluid conductivity over the vertical flow profile. The fluid conductivity was related to a particular volumetric salt concentration and fluid density. The fractional excess density profile was then calculated from these data. Data collected from this probe consisted of a time-series output at 50 Hz which was averaged over the same 180 sec averaging window used for the velocity data.

3.3.3 Data Analysis and Results

Non-dimensional velocity profiles and entrainment data from the flume experiments in this study are shown in figure 3.1 alongside data from several other stratified flow experiments. The data sources for the non-dimensional profiles in figure 3.1A are: [1] subcritical flows in this study, [2] supercritical flows in this study, [3] subcritical flows in García (1993), [4] supercritical flows in García (1993), [5] subcritical flows in Sequeiros et al. (2010b), [6] supercritical flows in Sequeiros et al. (2010b), [7] Parker et al. (1987), [8] Xu (2010). The other data sources in figure 3.1B are: Parker et al. (1987), Ashida and Egashira (1975), Ellison and Turner (1959), Fukuoka and Fukushima (1980), and Lofquist (1960). Though the flows in this study are very small compared to natural conditions and larger flume studies, the currents maintain non-dimensional similarity (fig. 3.1A) with similar entrainment coefficients (fig. 3.1B). These non-dimensional profiles were calculated using the measured velocity and fractional excess density profiles which were integrated over the vertical using the equations of Ellison and Turner (1959) given by

$$Uh = \int_0^\infty u \, \mathrm{d}z, \tag{3.1}$$

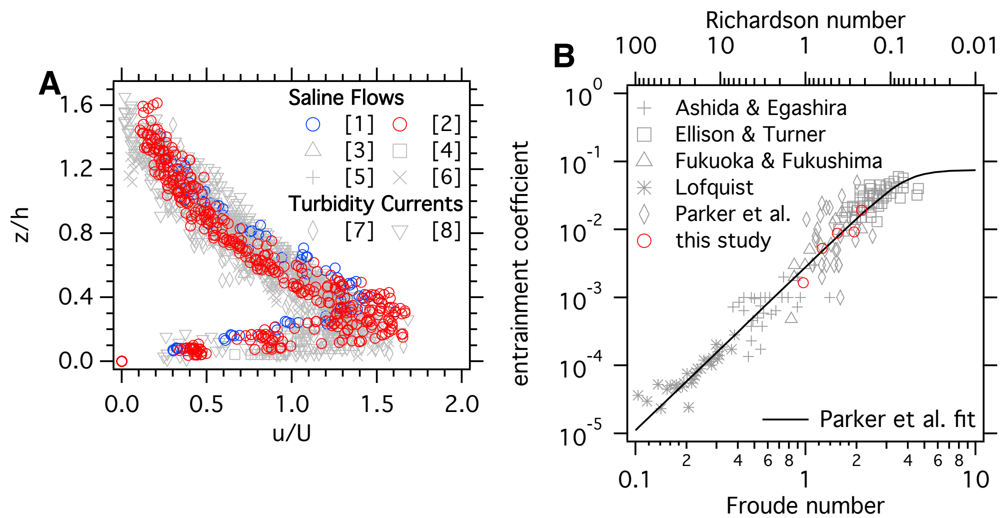

Figure 3.1: Experimental results: (A) non-dimensional profiles from; and (B) entrainment coefficient as a function of densimetric Froude number.

$$U^2h = \int_0^\infty u^2 \, \mathrm{d}z, \text{ and} \tag{3.2}$$

$$UF_eh = \int_0^\infty uf_e \, \mathrm{d}z, \tag{3.3}$$

where u, f_e, and z are the local velocity, fractional excess density, and upward normal coordinate respectively, and U, F_e, and h are the layer-averaged velocity, fractional excess density, and layer-thickness respectively. These quantities are needed in the control section for comparison with the PTV tracer measured velocity u_M. The range in conditions within the control section for the experiments were: $3.5 < U < 22$ [cm/s]; $4.8 < u_p < 32.2$ [cm/sec]; $1.0 < h < 3.9$ [cm]; $0.0030 < F_e < 0.0912$ [-]; $0.41 < F_r < 3.11$ [-]; $430 < R_e < 3880$ [-].

In looking at the development and calibration of the PTV method, the first question to address is the elevation where and how the tracers traveled within the stratified flow. The small square tracers were transported aligned with the flow, i.e., with their planform shape oriented parallel with the longitudinal flow path. Furthermore, from the side-looking camera it was found that the tracers reliably travelled near the peak velocity region (fig. 3.2A). This relationship persisted across the majority of experimental conditions. Each tracer transport elevation, h_t, measured from the side looking camera shown in figure 3.2A is the average of the 30-50 tracers seeded to an experiment. The average sample standard deviation for h_t was 0.08 cm and was not dependent on any of the independent variables or flow properties at the section of interest. The only exception to tracer transport in the peak velocity region was for conditions that were not able to keep the tracers in suspension due to the fact that the tracers were slightly more dense than the flow. This was a relatively isolated occurrence reserved for experiments with dilute currents and low velocities ($U < 2.5$ cm/sec) and laminar conditions (R_e<500). However, there were two instances of laminar flow (of four total) with $500 < R_e < 575$ where the tracers were transported similarly to those in turbulent conditions (included in fig. 3.2). The tracer settling observed in two experiments appeared to be more a function of reduced velocity and laminar conditions than a dilute current considering that similarly dilute currents transported tracers at higher velocities.

Knowing that the tracers were dependably located at a particular elevation within the flow was important; however the velocity calculated from the tracers needed to be related to a physically relevant velocity, i.e., the mean (U) or maximum (u_p), for hydraulic analysis. The velocity calculated through the particle tracking method tends to be closely correlated to the maximum velocity ($u_M = -0.49 + 0.91u_p$, fig. 3.2B). This is a reasonable outcome considering the location of particle transport within the flowing layer was near the maximum. It is hypothesized that tracers tend toward the peak velocity region because this region also corresponds with a minimum in vertical turbulent intensity (e.g., Kneller et al., 1999). The vertical turbulence diffusion gradient therefore converges at the point of maximum downstream velocity, tending to funnel particles to this zone of high downstream drag. Because the tracers are slightly more dense than the current, the density helps tracers settle through the outer region and the higher vertical turbulence between the peak flow and wall helps to keep the tracers from settling out along the channel. This hypothesis is supported by the settling of tracers solely in laminar flow experiments. Though the tracer velocities seemed to track the maximum velocity, they tended to lag the maximum velocity by a fraction. This is hypothesized to be a product of a very sharp peak in the velocity profile and imperfect transport at that point, i.e., tracers were not always at the point of maximum velocity. Nevertheless, the relationship was dependable across expected fan conditions. The average sample standard deviation for u_M in figure 3.2B is 0.7 cm/sec and showed no significant trend as a function of independent variables or layer-averaged flow properties at the section of interest. The close association between tracer transport and the vertical velocity profile, both in terms of transport elevation and transport velocity, combined with the relative insignificance of current density provided the tracers are near neutral buoyancy, suggests that this methodology is applicable for currents with a range of densities beyond that tested here.

In addition to the correlation between u_M and u_p shown in figure 3.2B, it is desirable to have a relationship which creates a link to layer-average velocity, U, as this is the velocity scale used to calculate quantities such as densimetric Froude number, Reynolds number, and average bed shear stress. Over the range of experimental conditions, there was a relationship between u_p and U ($u_p = 1.51U$, fig. 3.2C). This seems to be a product of the similarity of non-dimensional velocity profiles, i.e., u/U vs. z/h, across various density and turbidity currents (fig. 3.1A).

3.4 DEPTH AND EXCESS DENSITY CALCULATION

3.4.1 Methodology

The hydraulic data collected on the experimental fan consisted of a velocity field (U), flow width (W), and inlet boundary conditions. As such, the methods do not provide a full characterization of the flow field given we can not measure depth and excess density over the fan surface. To obtain those values, the 1D mass and volume

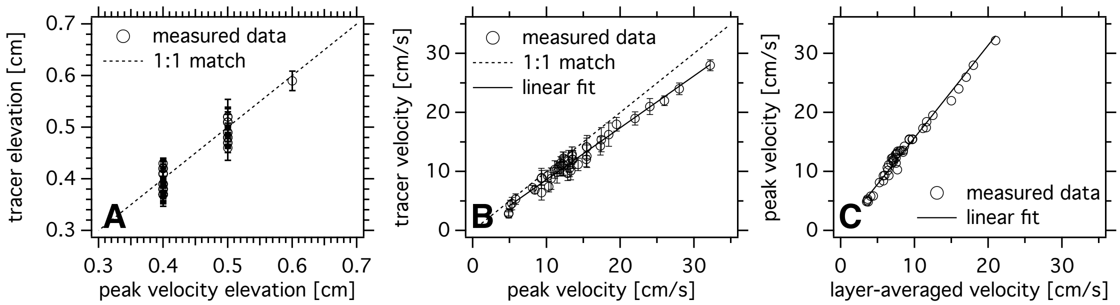

Figure 3.2: Results from flume experiments: (A) relationship between h_t and h_p; (B) empirical relationship between u_M and u_p; and (C) the relationship between u_p and U. Error bars are plus and minus one standard deviation.

conservation equations are solved in the streamwise direction. These equations are given by,

$$\frac{\partial UhW}{\partial x} = e_w UW \text{ and} \tag{3.4}$$

$$\frac{\partial UF_e hW}{\partial x} = 0, \tag{3.5}$$

where e_w is the entrainment coefficient given by Parker et al. (1987) as

$$e_w = \frac{0.075}{(1 + 718F_r'^{-4.8})^{0.5}}. \tag{3.6}$$

Eq. 3.6 was verified for use in this study through a set of 5 flume experiments by calculating e_w from the 1D conservation of fluid mass equation ($\mathrm{d}Uh/\mathrm{d}x = e_w U$) between two measured vertical profiles. The data, presented in figure 3.1B, fell well within the scatter presented by Parker et al. (1987) (i.e., Ellison and Turner, 1959; Lofquist, 1960; Ashida and Egashira, 1975; Fukuoka and Fukushima, 1980) and is in good agreement with the fit proposed by Parker et al. (1987).

Given this procedure, if overhead imagery can provide the layer-averaged velocity field and flow width, then, layer thickness and fractional excess density can be calculated along the flow path provided known upstream boundary conditions.

3.5 TEST OF CONCEPT: INTEGRATION OF METHODS

In the following, we demonstrate the integration of the presented methods using data from one fan experiment run in the tank shown in figure 2.1. The boundary conditions for the experimental fan to test the method were: a discharge of 4.58 L/min (1.21 gpm), an inlet salt concentration of 0.17 g/cc, a volumetric sediment concentration of 0.01, and a plate slope of 0.186 (10.5°). In the experiment, all inlet conditions where held constant and the fan was allowed to develop autogenically over time. One of the primary morphologic features that developed in the experiment was a self-formed channel that terminated in a flow expansion and zone of significant deposition (e.g., fig. 3.3). During the formation of one such channel, overhead images were used to map the width down channel and to collect images for the PTV analysis (fig. 3.3). The various panels in figure 3.3 show: (A) an overhead image (red band only) showing the submarine fan flow field delineated by the dashed line and the flow tracers as dark particles within the flow; (B) and (C) a zoomed-in view of tracers

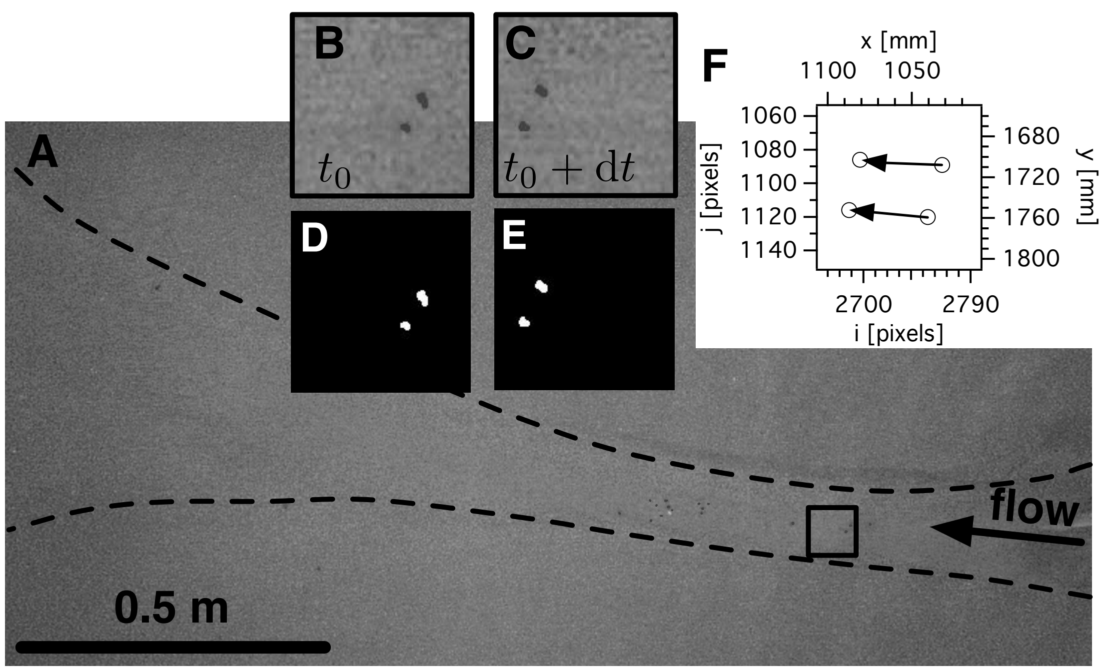

Figure 3.3: Overview of method application.

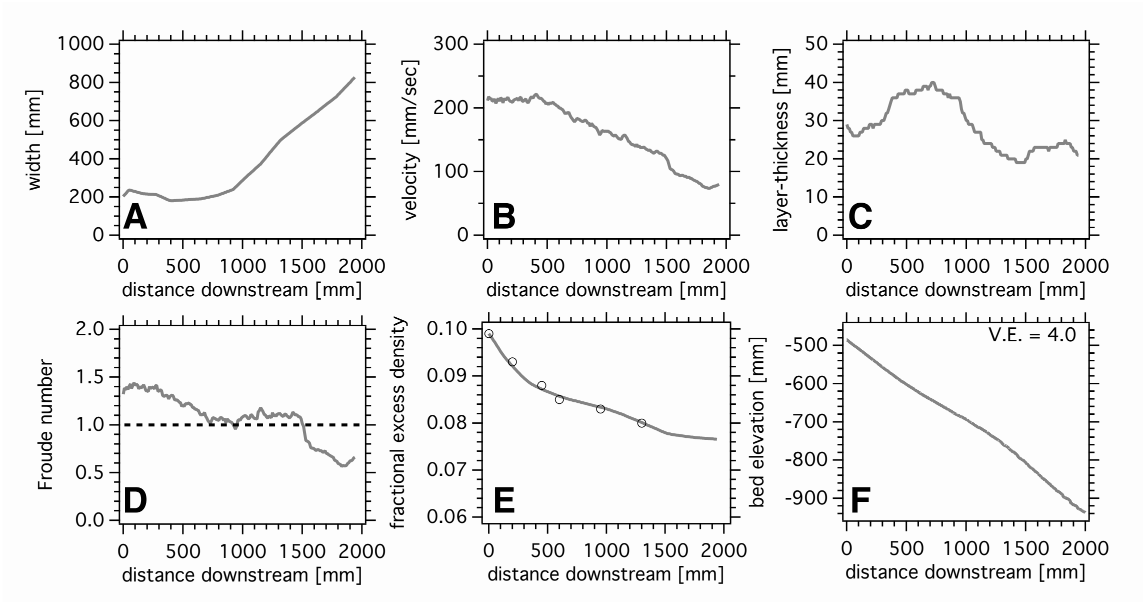

Figure 3.4: Downstream trends in: (A) flow width, (B) cross-sectionally averaged velocity, (C) density current layer-thickness, (D) densimetric Froude number, (E) fractional excess density, and (F) bed elevation.

in subsequent images at the identified channel location; (D) and (E) post-threshold binary indications of tracer/non-tracer; and (F) the location of the tracers in panels B and C and what the resulting velocity vector would be for these given tracers in this pair of images. The channel width profile, $W = W(x)$, and velocity down the centerline of the channel can then be used along with the boundary conditions and equations 3.4, 3.5, and 3.6 to calculate the hydraulic properties of the flow (fig. 3.4).

Overall, integration of the method using the procedures outlined works exceptionally well. Spot checks of the fractional excess density were made with the conductivity probe along the length of the channel, and measured and calculated values match nicely (fig. 3.4E). Given the calibrated PTV method and the auxiliary values measured, submarine fan experiments can be hydraulically quantified as a function of downstream distance.

3.6 SUMMARY

A new method for monitoring the velocity of laterally unconstrained density currents is presented wherein the velocity is monitored by non-invasive PTV techniques, width is constrained from overhead images, and layer-thickness and excess density are calculated along the flow centerline by solving the balance of volume and balance of mass equations. This concept is potentially applicable across a wide range of transparent density current flows, however the exact trends are potentially specific to this study due to the effect of bed roughness and the particular tracer. Unfortunately, because the methodology is predicated on observing within-current tracers the methodology is restricted to transparent gravity flows and not suitable for turbidity currents. In summary, the methodology presented here is capable of hydraulically characterizing submarine fan experiments which when combined with bed elevation data, provides a new approach to form complete picture of morphodynamic feedbacks that is a unique to the experimental geomorphology community.

Chapter 4. Hydraulic and Sediment Transport Properties of Autogenic Avulsion Cycles on Submarine Fans with Supercritical Distributaries

4.1 RESULTS

4.1.1 General Morphodynamic Description

Here we describe the observed morphodynamic evolution from a general perspective ahead of a more detailed description in a subsequent section. The beginning of each experiment consisted of a channel incising into the initially unchannelized sediment bed and prograding basinward while feeding a frontal splay. Eventually this channel stagnated and aggraded a mouth bar ahead of itself that created an obstacle to the flow. Though the experimental domain included a slope break, incipient mouth bars were emplaced on the more steeply sloping portion of the domain, i.e., the slope break did not play a role in restraining the system. Following mouth bar deposition, a hydraulic jump formed on the upstream side of the incipient bar which subsequently retreated upstream over time and avulsed to create a new channel extending from the upstream direction. By tracing the distance from the inlet to the channel-to-lobe transition, L_{clt}, over time, it is easy to see these cycles (fig. 4.1A and C). Increases in time of L_{clt} correspond to progradation, constant values to stagnation, and decreases to retreat. Figure 4.1 shows several of the experimental runs. Average cycle periodicity, T_c, ranged between 12 and 18 min for the experiments shown in figure 4.1.

Cycles were qualitatively more prominent in those experiments with higher densities, velocities, and sediment transport rates, i.e., Fan03-A, Fan06-A, Fan09-A, and

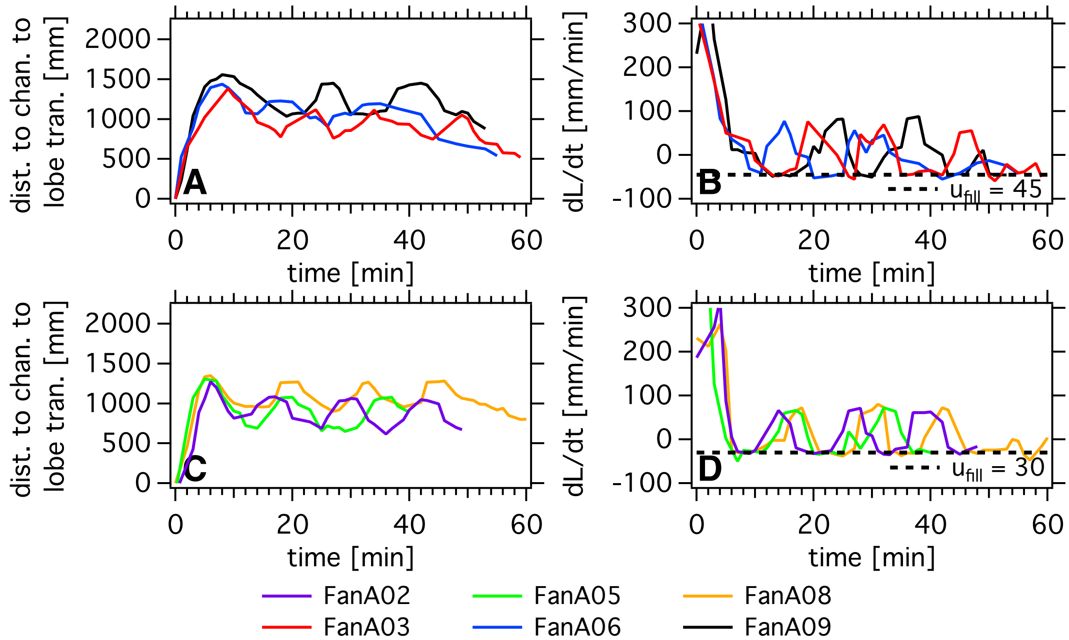

Figure 4.1: Time series showing: (A) L_{clt} in the high density experiments; (B) time derivative of L_{clt} in the high density experiments; (C) L_{clt} in the medium density experiments; (D) time derivative of L_{clt} in the medium density experiments.

were weak to largely suppressed in those with lower densities, velocities, and transport rates, i.e., Fan01-A, Fan04-A, Fan07-A. This is primarily a qualitative observation based on the perceived "strength" of the cycles. One quantitative way this observation can be described is with the time rate of change in L_{clt}, $\mathrm{d}L_{clt}/\mathrm{d}t$, where the more aggressive cycles have higher rates of basinward extension during channel carving as well as faster rates of upstream retreat before avulsion (figure 4.1B and D).

4.1.2 Distributary Channel Hydraulic and Sediment Transport Context

Throughout the evolution of each fan experiment, we measured the hydraulic properties of the system and then used these to calculate the sediment transport properties. The characteristic hydraulic and sediment transport variables for the channels feeding the lobes in each experiment are presented in table 4.1. The values

Table 4.1: Observed channel hydraulic and sediment transport properties averaged from the inlet up to the channel-to-lobe transition.

Run	U [mm/s]	W [mm]	F_r [-]	R_e [-]	Q_t/Q_s [-]	τ^*/τ^*_{cr} [-]	z_* [-]	L_{ext} [mm]
Fan01-A	182	157	2.08	3780	1.1	7.5	1.9	1070
Fan02-A	237	130	2.16	4050	3.3	13.2	1.4	1350
Fan03-A	248	121	2.27	3080	3.8	15.7	1.4	1450
Fan04-A	185	160	2.01	3820	1.0	7.6	1.8	1160
Fan05-A	227	138	2.14	3430	1.9	11.2	1.5	1370
Fan06-A	234	122	2.21	3290	2.7	13.0	1.5	1460
Fan07-A	151	201	1.76	2890	0.8	5.6	2.3	-
Fan08-A	180	141	1.81	3220	1.1	7.1	1.9	1350
Fan09-A	212	124	1.88	3270	1.4	9.5	1.6	1560
Fan10-A	215	123	1.89	3380	1.3	9.6	1.6	1570
Fan11-A	209	124	1.86	3367	2.6	9.5	1.6	2080

reported represent an average along the length of the channel from the inlet up to the channel-to-lobe transition throughout the duration of the experiment. In this table h and $\Delta\rho$ are omitted as they were highly variable along the length of the channel due to ambient entrainment. U, F_r, W, Q_t/Q_s, and τ^*/τ^*_{cr}, on the other hand, were relatively constant from the inlet to the flow expansion point. R_e changed along the flow path due to changes in h, so average values are presented for context. F_r also includes h, but changes in $\Delta\rho$ counteracted changes in h such that F_r stayed relatively constant. Beyond consistency in the downstream direction within the channel, hydraulic conditions remained relatively constant in time.

In terms of sediment transport, all channels, except those in Fan07-A, were erosive or bypass ($Q_t/Q_s \geq 1$). Fan07-A eroded a small channel but was never erosive enough to incise a channel accommodating the entirety of the flow. Those experiments with Q_t/Q_s values substantially above 1.0 are a little misleading as once the channel was eroded down to the non-erodible plate, i.e., once no more sediment was available to be eroded, they were essentially bypass channels. In general, values for Q_t are perhaps slightly over-predicted in that subsequent bathymetric scans showed little bed variation in time for Q_t/Q_s values in the range of $1.0 \sim 1.4$.

The width of the self-formed channels varied from experiment to experiment. The boundary condition that most strongly influenced the width was the excess density, $\Delta\rho_{in}$. Larger density anomalies led to higher velocities down the slope and narrower channels. Though there was some difference in channel width between the experiments, the channel width did stay nearly constant throughout the duration of each experiment. After being incised, channels appeared to quickly reach equilibrium, evidenced by consistency in both channel geometry and hydraulic properties in time. Furthermore, the behavior of the channels was consistent among experiments with the same boundary conditions, i.e., Fan09-A and Fan10-A.

4.1.3 Avulsion Cycle Mechanics

In this section, each segment of the avulsion cycle is reviewed using an example from Fan10-A which was measured at a 2 min temporal resolution (fig. 4.2). A particular example is used as representative of the behavior observed across all experiments and cycles since the behavior was quite consistent. This was especially true with respect to non-dimensional variables and the downstream transitions in these variables. An overview of the cycle is shown in figure 4.2 while the hydraulic variables and bathymetry transects are in figure 4.3. The panels in figure 4.3 show: (A) densimetric Froude number, F_r; (B) sediment transport capacity to sediment supply ratio, Q_t/Q_s; (C) flow width, W, with an inset of rate of change in width with respect to downstream distance, dW/dx; and (D) Shields stress ratio, τ^*/τ^*_{cr}. Bathymetric data from Fan10-A at: (E) section A-A' (orange line in fig. 4.2), (F) section B-B' (magenta line in fig. 4.2), and (G) along the centerline of the flow path at each time.

Channel Extension and Stagnation

The initial action in the avulsion cycle was the basinward extension of the channel. This was most easily observed and measured during the first few minutes of each

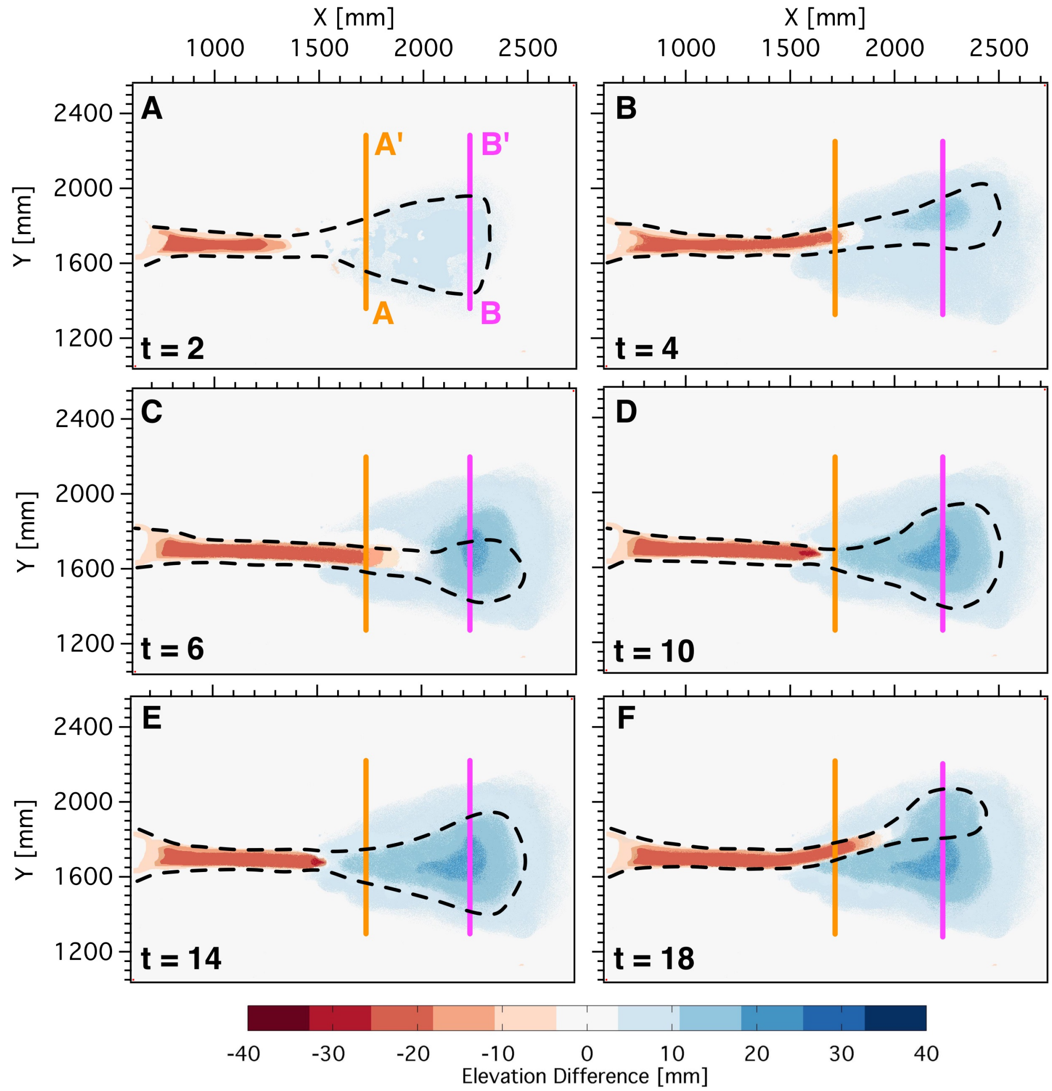

Figure 4.2: Bathymetric difference from the initial setup showing the sequence of events within the avulsion cycle. The dashed lines identify the flow field at each time. Note that the inlet is at the left of each graph.

experiment as the system extended into the undisturbed basin. This removed any complications due to uneven pre-cycle bathymetry. As the channel extended, it fed a frontal splay that developed ahead of the intersection point, the point where the incised channel becomes dechannelized (fig. 4.2A). The channel continued to prograde by incising through sediment ahead of the intersection point. At the start of the experiment, the sediment through which the channel incised was only the initial pre-graded bed. However, with time and distance downslope, the channel also had to incise into material that had previously been deposited in association with the frontal splay (fig. 4.2B). At some point down the slope, channel extension ceased (fig. 4.2C). While there was a slope break in the experimental domain, all channels except one (Fan11-A) stagnated well before reaching the break leaving lobes perched on the sloping fan surface. Note that the slope break is not shown in figure 4.2 or figure 4.3 as it is further downstream.

Along the actively prograding channel, the hydraulic and sediment transport variables were relatively consistent in the channelized flow up to the expansion (fig. 4.2A and 4.3 at $t = 2$ min). Just downstream of the intersection point, the flow began to expand laterally and there was a short distance over which the velocity, and therefore sediment transport capacity, increased downstream ahead of the prograding channel (fig. 4.3B at $t = 2$ min). This appeared to provide the impetus for sustained progradation. Beyond the initial increase, velocity and sediment transport capacity continuously decreased. The reduction in Q_t/Q_s below unity was important to the cycle as the transition from bypass or erosion to deposition set the eventual lobe location. The increase in transport capacity ahead of the expansion was not seen later in the cycle (fig. 4.3B at $t = 4$ and $t = 6$ min). This was likely due to a less abrupt expansion (fig. 4.3C inset) and a reduced slope from the sediment deposited ahead of the channel (fig. 4.3G). In this way the distance from dechannelization to deposition was reduced. While the area downstream of the intersection point was net depositional, there was still active sediment transport, i.e., $\tau^* > \tau^*_{cr}$. This allowed the ensuing lobate deposit to extend slightly beyond the initial point of deposition.

It is of particular note that an erosive channel is requisite for the morphodynamic feedback outlined above with our experimental approach. Because the material we were working with was non-cohesive and traveling as bedload, channel building came through erosion of the substrate rather than through levee building, as may occur when fine material is carried in suspension.

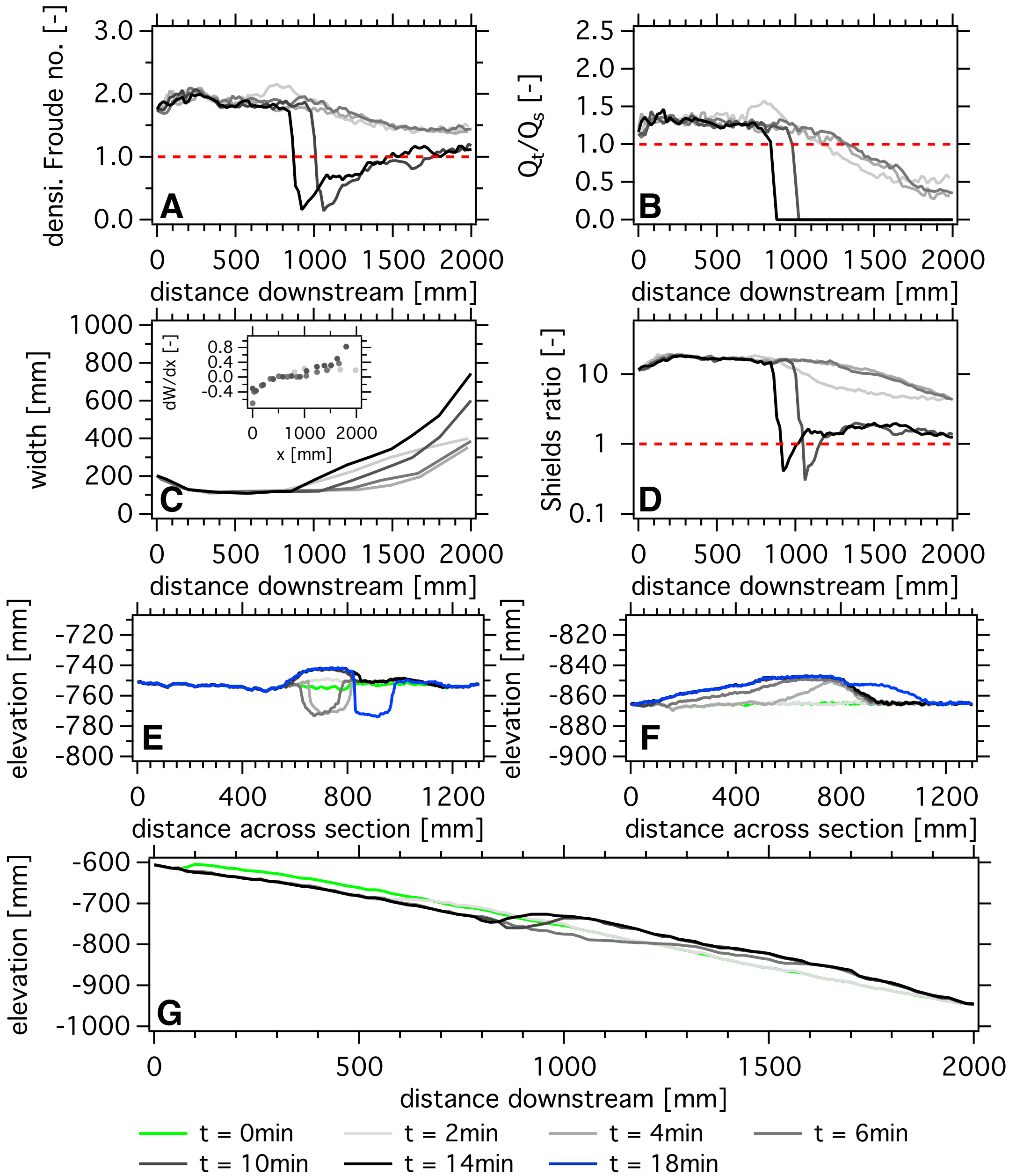

Figure 4.3: Downstream trends for hydraulic and sediment transport parameters during Fan10-A.

Bar Aggradation and Jump Initiation

With a drop in Q_t/Q_s below unity, a mouth bar ahead of the channel aggraded to create an obstacle growing with time that the flow had to pass over. Any relocation of the depocenter at this point was due to lateral migration of the channel-to-lobe transition (e.g., fig. 4.2C). Lateral migration was common, though not ubiquitous, during the bar aggradation phase of the cycle. At some point a hydraulic jump formed upstream of the aggrading mouth bar (fig. 4.2D and 4.3A between $t = 6$ and $t = 10$ min). It is important to note that the jump occurred after a mouth bar had already begun to form.

Though there was already an expanded flow region beyond the intersection point as the channel prograded basinward (e.g., fig. 4.2A, B), the expansion angle increased following hydraulic jump initiation. This can be seen by an increase in the spatial rate of change of width (inset of fig. 4.3C). The rate of change in width continued to increase in the downstream direction after jump formation while it leveled off prior to jump formation.

We hypothesized that a choked flow condition was responsible for initiating the hydraulic jump observed in each avulsion cycle. To test this, the parameter space for the critical step height, $\Delta\eta_{max}$ (eq. 2.13), is explored in figure 4.4 as a function of current velocity and excess density for a flow thickness of $h = 25$ mm (a reasonable average value for the experiments). The location of U and $\Delta\rho$ from just upstream of the jump in our experiments is also shown in the parameter space. The critical step height predicted by this analysis was compared to elevation change in our experiments to see whether or not the aggrading bar could have produced choked flow and triggered a jump. One difficultly in the analysis is that even with velocity and bathymetric scans at 2 min intervals, as in Fan10-A, the exact bar height at the time the jump was triggered was very difficult to catch. Nevertheless, the data seem to point to the bar height at the time of jump initiation being approximately equal to $\Delta\eta_{max}$. For example, at $t = 6$ min during the Fan10-A experiment, the predicted step height needed for a local choked flow condition was $\Delta\eta_{max} = 22$ mm. The maximum observed bar thickness at that time was 18 mm. This could easily have been aggraded to the choked flow condition and triggered the jump that occurred around $t = 7.5$

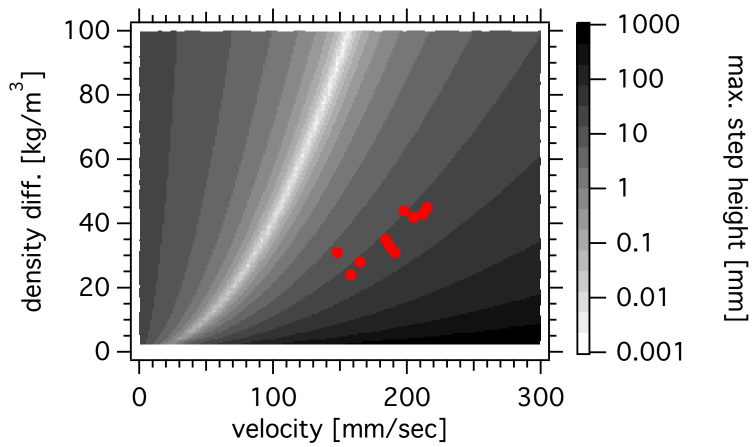

Figure 4.4: The velocity vs. excess density parameter space as it pertains to the critical step height for a particular flow with a layer-thickness of $h = 25$ mm.

min. Furthermore, the theoretical $\Delta\eta_{max}$ value for all experimental conditions, 10-30 mm, was well within the vicinity of observed bar thickness, 18-26 mm.

There is one potential competing hypothesis regarding jump initiation that bears testing. It is that the mouth bar ahead of the channel has a slope below the critical slope and therefore a subcritical normal flow depth. If this were the case, then there would necessarily be a hydraulic transition in the form of a jump from the upstream supercritical section to the downstream subcritical section (Chow, 1959). However, the calculated critical slope ($S_{cr} = 0.024$) is lower than the slope attained anywhere in the channels or on the mouth bars in our experiments. In general, mouth bar slopes ranged from 0.08 to 0.14. This means that a downstream subcritical normal flow boundary condition was not responsible for the hydraulic jump formation in this study.

Upstream Retreat

After a hydraulic jump initiated (just upstream of the locus of deposition associated with a decay in Q_t/Q_s), the region upstream of the initial depocenter and just downstream of the hydraulic jump became the primary locus of deposition. This caused the within-channel portion of the deposit to retreat upstream over time, which forced the hydraulic jump to retreat farther upstream. A majority of sediment was detained in this jump region with a limited amount transported through the jump and further downstream onto the lobe (fig. 4.3B). Though there was active sediment transport downstream of the jump ($\tau^* > \tau^*_{cr}$; fig. 4.3D), the lobe-scale morphologic impact was negligible given that the bulk of sedimentation occured in the near-jump region.

The hydraulic jump continued to retreat upstream at a rate, u_{fill}, dictated by sediment supply and the cross sectional fill area A_{fill}. Because the hydraulic jump allowed some sediment to escape up onto the lobe and the surrounding area, the fill area is characterized by the sum of the channel body area, A_{cb}, and the sediment cap area, A_{cap} (fig. 4.3E and F). A_{cb} is well approximated by a trapezoidal channel and A_{cap} by a circle segment. From there the rate of upstream retreat and channel filling, u_{fill}, can be approximated as $u_{fill} = Q_s/A_{fill}$. Because the flow depths were relatively similar between experiments, differences in the rate of upstream retreat and channel filling, u_{fill}, can largely be explained by differences in channel width. This is reflected in figure 4.1 where those with higher initial densities, and therefore higher velocities and smaller widths (fig. 4.1A and B) have faster rates of retreat than those with lower densities (fig. 4.1C and D). The difference in width also appears to be a control on the rate of channel advance, u_{adv}, during the channel extension phase of the cycles.

One distinct aspect of this phase of the cycle compared to the channel progradation and bar aggradation phase was a change in the areal extent of the flow downstream of the transition, and therefore a change in the shape of the region of deposition. Prior to stagnation, flow downstream of the channel-to-lobe transition expanded abruptly and then leveled off (fig. 4.2A, 4.3C inset). After stagnation, the expansion was more gentle but continued expanding downstream (fig. 4.2B and C and4.3C inset). Finally, after the hydraulic jump the expansion continued but at a higher rate than before. This led to a flow field that covered most of the lobe deposit downstream of the jump, i.e., the entire lateral extent of the initial mouth bar, not just the most recently active area.

Avulsion Location

As the jump retreated upstream, there was a point where the flow abandoned its present path in favor of another. This point of avulsion was rapid and very difficult to experimentally measure. However, qualitatively, we observed that the new flow path was often along the margin of the previous lobe deposit. This was the case for the event shown in figure 4.2F. We hypothesize that avulsion was, at least partly, a function of rill formation along the lobe margin. The transverse velocity over the lobe increased with time as the center of the lobe built up and shed flow away from the downstream centerline. As flow was shed off the deposit, it collected along the edges of the lobe as it continued to flow down slope. Rills then began to form and grow over time along the lobe margin, initiating a deepening feedback. With time, one such rill captured the majority of the flow and the cycle of basinward extension began anew. One important note about this behavior is the absence of levees in these experiments. Presumably overtopping a levee as a means of avulsion would be more difficult than avulsion by means of reincision through non-cohesive sediment as was the case here.

4.1.4 One-dimensional Model Results

During channel progradation, the channel-to-lobe transition moved progressively downslope before eventually stagnating. However, at any particular time, both before and after the progradation ceased, there was a transition in the downstream direction from an erosional or bypass zone to a region of net deposition. This transition was associated with a drop in the transport capacity to supply from a value of $Q_t/Q_s \approx$

1.25 down to and below a value of 1 (fig. 4.3B). Based on equation 2.10 one can see that U, ρ_f (or R_s), and W are the variables controlling transport capacity for a given value of C_f. Since $Q_t \propto W$ and channel width does not narrow in the experiments, we conclude that reduction in capacity has to be associated with downstream changes in U and ρ_f.

Two mechanisms that could produce these changes are the entrainment of less dense ambient fluid within the channel and the flow expansion downstream of the channel-to-lobe transition. Therefore, it is of interest to examine the following two questions: (1) is the effect of downstream dilution due to entrainment sufficient to cause a transition to deposition within the channel, and (2) if not, what are the relative effects of dilution and velocity decay on transport capacity within an expansion? To answer these questions, we examine a series of solutions of the 1D density current model (eqs. 2.19-2.22) for a range of laterally confined and unconfined conditions. The boundary conditions used for the laterally confined case were: $F_{r0} = 2.0$, $Q_0 = 0.0003$ m^3/s, $\Delta\rho_0 = 80$ kg/m^3, $S_0 = 0.17$, $C_f = 0.02$, and $Q_s = 1.84 \times 10^{-6}$ m^3/s (results in figure 4.5A and B). The boundary conditions used for the laterally unconfined case were: $F_{r0} = 2.0$, $Q_0 = 0.0005$ m^3/s, $\Delta\rho_0 = 45$ kg/m^3, $S_0 = 0.17$, $C_f = 0.02$, and $Q_s = 1.84 \times 10^{-6}$ m^3/s (results in figure 4.5C and D). Figure 4.5 shows model results as a function of downstream distance for U/U_0, $\Delta\rho/\Delta\rho_0$, R_s/R_{s0}, Q_t/Q_s. The density difference is smaller and the discharge greater in the expanding scenario relative to the laterally confined case. This is done to better match the actual conditions in the experiments since entrainment occurs along the length of the channel. Changes in the boundary conditions can change the magnitude of the hydraulic and sediment transport parameters, but such changes do not result in any fundamental difference in the functionality or conclusions drawn from the analysis.

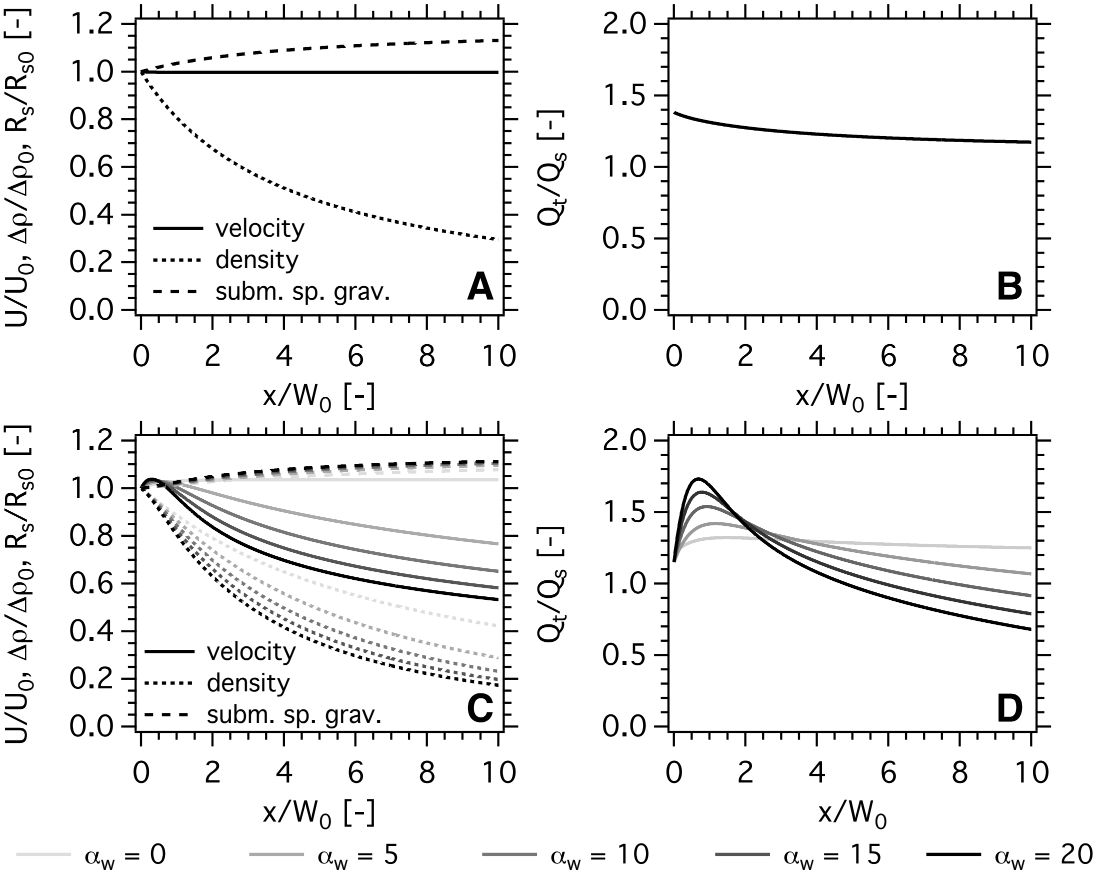

Figure 4.5: Dependence of Q_t on U and ρ_f from model results. Panels (A) and (B) are for the laterally confined case and (C) and (D) are for the expansion cases.

The effect of entrainment alone, and hence dilution of the current, on the transport capacity of the flow can be examined by setting $dW/dx = 0$ in equations 2.19-2.22. Doing so for any reasonable range of boundary conditions results in velocity quickly adjusting to a normal flow condition where the driving and resisting forces are balanced. Once reached, U and R_i remain constant in the downstream direction while h and ρ_f both continually change (fig. 4.5A). The decay in ρ_f results in an increase in R_s and hence a decrease in Q_t downstream. While there was a substantial decrease in the calculated ρ_f along the channel (an approximate 70% reduction after 10 channels widths), figure 4.5B shows that the reduction has little impact on the transport capacity. The reason for this is that a one-half reduction in the density anomaly only produces a fractional increase in R_s of 0.13, which in turn leads to a decrease in capacity to supply ratios of 0.14. Based on the experimental data, reductions in Q_t/Q_s on the order of 0.25 or more were associated with the zone of significant deposition. This demonstrates that it is unlikely that dilution within the channel was alone responsible for the significant drop in the carrying capacity of the flow. It is interesting to note that the dilution effect on Q_t becomes stronger for larger $\Delta\rho_o$ and lower R_s values. Since natural turbidity currents would likely have smaller $\Delta\rho_o$ values and larger R_s values, it is expected that the changes in transport capacity due to entrainment are even less significant in the field.

If the decrease in transport capacity cannot be fully explained by dilution alone within the channel, then the major component of the Q_t/Q_s reduction must be an outcome of the expanding flow downstream of the channel-to-lobe transition. In an expansion, the increase in width drives a general deceleration in the flow. Deceleration alone would lead to a decrease in the rate of ambient entrainment and hence a decrease in the rate of density reduction and flow thickening. However, the expansion also drives an increase in entrainment by increasing the top-width of the current with each step downstream. Solution to equations 2.19-2.22 for various α_w values therefore provides a nice way to examine the change in U, ρ_f, and Q_t in an integrated way. The results are plotted in figure 4.5C and D and show the influence of the expansion on the key parameters. By comparing figures 4.5C and D, one can see that the shape of the $Q_t = Q_t(x)$ curve (fig. 4.5D) more closely resembles that of $U = U(x)$ than it does $\rho_f = \rho_f(x)$ or $R_s = R_s(x)$ (fig. 4.5C). This is reasonable given that $Q_t \propto U^3$ whereas $Q_s \propto R_s$, and it indicates that the decay in transport is more strongly influenced by the expansion-generated decrease in velocity than the expansion-enhanced entrainment. The relative insensitivity of R_s to changes in expansion angle and entrainment, which is the density-relevant control on Q_t, can further be seen in figure 4.5C despite the larger variability in ρ_f.

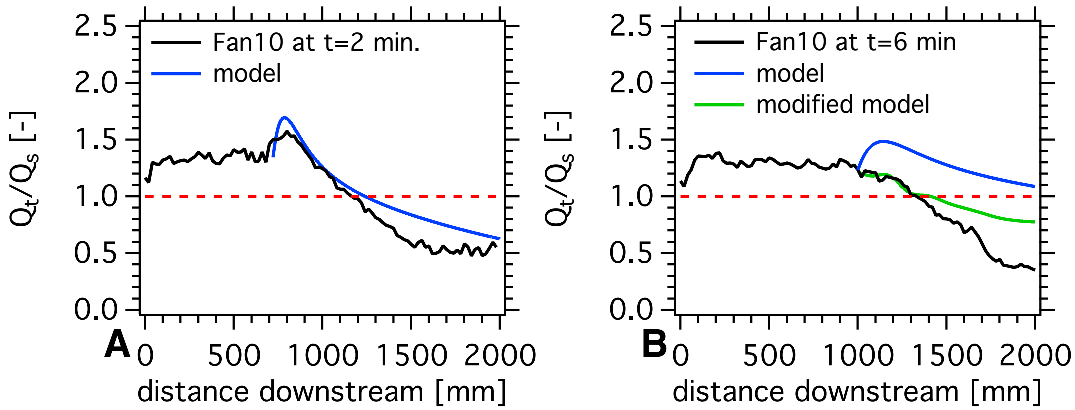

Figure 4.6: Comparison of Q_t/Q_s between the expanding density current model and data for Fan10-A.

The 1D model also gives some insight into a possible mechanism for the initial progradation of the channel. Solution to equations 2.19-2.22 with a fixed angle of expansion indicates that, for supercritical flows, just downstream of an expansion on a continuous slope there will be: (1) a decrease in flow thickness and (2) a corresponding increase in velocity. This occurs when the width expands at a rate high enough to keep entrainment from imposing the converse through increasing the thickness and decreasing velocity. The model-predicted increase in velocity just downstream of an expansion was indeed observed in the flow data during initial channel progradation (fig. 4.6A), and it led to a corresponding increase in Q_t/Q_s. As mentioned before, it seems likely that the predicted and observed increase in transport capacity just within the expansion helped to sustain the basinward extension of the channel.

During the initial progradation phase, the simple model was able to well match $Q_t/Q_s = Q_t/Q_s(x)$ data using a constant basin slope and a fixed expansion angle (fig. 4.6A). However, once the channel stagnated and started to fill space down slope, as in figure 4.2B and C, the local expansion hydraulics changed and the initial increase in transport capacity within the expansion disappeared. During this phase, use of a constant basin slope and expansion angle resulted in a mismatch between the calculated and observed behavior for $Q_t/Q_s = Q_t/Q_s(x)$ downstream of the intersection point (fig. 4.6B). This mismatch can be attributed to the change in the local bathymetry and flow expansion behavior created by the aggrading mouth bar. The aggrading mouth bar created a shallowing of the bed slope within the expansion and a more subtle and less abrupt expansion of the flow (e.g., figs. 4.2A-C and 4.3G). The model can be modified to incorporate this behavior by using the measured data to calculate the width expansion rate, dW/dx, and local slope, $S = -d\eta/dx$. Incorporating measured dW/dx and $d\eta/dx$ in the calculations improved model behavior substantially, but the distance to deposition was still slightly over-predicted (fig. 4.6B). It is possible that this is a result of the model's inability to capture the increased lateral velocity, and therefore decreased downstream velocity, driven by the mounded lobe.

4.2 DISCUSSION

4.2.1 Experimental Scaling Considerations

As mentioned before, our experiments were not scaled *a priori*. Instead, the objective was to explore the autogenic cycles over the range of boundary conditions that produced the channel and lobe features while suppressing bedforms. Despite a lack of strict scaling rules, experiments have been shown to be effective tools in recreating natural geomorphic behaviors despite small size (Paola et al., 2009; Kleinhans et al., 2014). Having previously established scaling relationships based on densimetric Froude number similarity, here we consider the hydraulic and sediment transport properties of our experiments.

Two of the more important hydraulic non-dimensional numbers are Froude number and Reynolds number. All of the distributary channels in this study were supercritical ($F_r > 1$, table 4.1) as was the goal at the outset. While supercritical flow is not particularly common in subaerial flows, it is potentially much more widespread in subaqueous environments due to the modified gravity term g' in lieu of g. As to the Reynolds number, all experimental channels were fully turbulent ($R_e > 1000$) though not substantially above the typical threshold (table 4.1). This is not particularly bothersome for two reasons: (1) even if there are patches of transitional or laminar flow, sub-turbulent flows have been shown to produce realistic behavior (Metivier et al., 2005; Lajeunesse et al., 2010) and (2) the dominant mode of sediment transport is bedload for which turbulence is not a prerequisite. Additionally, though they are much smaller than their natural counterparts, the flows in these experiments retain similar non-dimensional vertical velocity profiles and entrainment coefficients (Hamilton et al., 2015c).

In considering the prevalence of bedload in these experiments, the Rouse number is reported in the second last column of table 4.1. These values are all less than the $z_* \geq 6$ demarcation for exclusive bedload transport as given in the Greimann et al. (2008) equation developed from the experimental data of Guy et al. (1966). Based on the experimental z_* values, estimates of the average fraction of material traveling as bedload from the equation of Greimann et al. (2008) is $\approx 70\%$. However, based on visual observation, one would expect that nearly all of the sediment moves as bedload, except within the hydraulic jump where there is substantial suspension. Beyond visual observation, there are further reasons to consider that calculated z_* values may under predict the degree of bedload dominance. First, the generic formulation for z_* assumes a Schmidt number, $Sc = \nu_T/\epsilon_s$ equal to unity, i.e., the turbulent driven fluid momentum, ν_T, and sediment mass diffusivities, ϵ_s, are equal. This assumption may not strictly hold for bedload grains that likely have Schmidt numbers > 1 (Schmeeckle, 2014). Secondly, the vertical structure of density currents is distinct from open channel flows in that there is substantially more interfacial stress (Sequeiros et al., 2010b). The increase in interfacial stress results in a peak velocity and a corresponding minimum in the turbulent kinetic energy (Kneller et al., 1999) where vertical momentum exchange is suppressed well within the core of the flow. The current is therefore segmented into two layers with different vertical mixing characteristics, and this may result in mobile coarse bed sediment tending to be confined to the lower region below the peak velocity. Therefore, based on these lines of reasoning and visual observation we consider channels to be bedload dominated even though $z_* < 6$. Since bedload is the dominant mode of sediment transport and the density contrast is imposed via dissolved salt, these experiments do not simulate the morphodynamic interaction of suspended sediment. Natural systems driven by turbidity currents by definition transport substantial sediment in suspension though this does not preclude bedload transport (e.g., Sequeiros et al., 2010a). Large-scale coarse-grained bedforms found in nature indicate that bedload is perhaps an important component of submarine fan morphology (e.g., Winn and Dott, 1977; Wynn et al., 2002).

4.2.2 Channel Incision and Stagnation

The focus of the study is on the mechanics associated with autogenic avulsion cycles. Therefore, we did not focus particularly on the properties of the first incisional channel. Nevertheless, the properties of this incipient channel are worth discussing. Weill et al. (2014) showed that channel width and depth are positively correlated with discharge and that rate of incision is dictated by slope. In our experiments, we observed that channel width was most strongly a function of, in terms of boundary conditions, density at the inlet. This appears to be an indirect association as the inlet density dictates the velocity of the current, with density and velocity being positively correlated. The progression of the channels down the slope, i.e., an incisional channel feeding an unconfined flow ahead of it, is similar between the two sets of experiments. One major difference though is that the channels created by Weill et al. (2014) extend all the way to the slope break in their basin whereas our channels typically stop short. The types of incisional channels observed by us and Weill et al. (2014) are distinct from the leveed channel observed by Yu et al. (2006) or Cantelli et al. (2011). The primary difference is the lack of levees in our incisional channels due to the lack of suspended sediment.

In contrast to the study of Weill et al. (2014), our incipient channels stopped prograding and switched to a mouth bar aggradation phase before reaching the basin slope break, i.e., the system restrained its progradation which left lobes perched on the slope. The one exception to this was the initial incisional channel of Fan11-A that extended all the way down to the basin slope break. The only difference between Fan11-A and Fan10-A was that the sediment feed rate for Fan11-A was one-half that of Fan10-A. Comparison of the channel extension length and boundary conditions between these two experiments seems to suggest that the ratio of current capacity to inlet supply helps to dictate how far into the basin the channel can prograde. This seems to fit with the overall observation from the avulsion cycles that channel stagnation and bar aggradation results from a reduction in Q_t/Q_s associated with the velocity and slope reduction as the laterally unconfined part of the channel progrades over the previously deposited frontal splay (fig. 4.3).

For Fans 01-A through 10-A, the initial channel did not reach the basin slope break, and the length of the extension from the inlet to the intersection point, L_{ext}, varied from experiment to experiment (table 4.1). A natural question following this observation is, what governs the initial channel length, L_{ext}? Does it vary as one might expect after comparing the L_{ext} and the boundary conditions of Fan10-A and Fan11-A? This question is briefly considered here but primarily remains the subject of future work. Counterintuitively, the L_{ext} from Fan01-A through Fan10-A is generally inversely correlated with initial basin slope, S_p, when all other boundary conditions are the same, similar to the observations of Hoyal and Sheets (2009a). In general, one would think that increasing the slope while keeping inlet sediment supply constant would only further increase transport capacity and push the initial channel to prograde farther downslope. We think that the inverse relation of L_{ext} and S_p is, at least in part, due to the fact that the current can erode down into the slope substrate and entrain bed material. Bed material entrained into the bedload layer during channel construction can therefore act as an extra supply of sediment to the material being fed at the inlet. The two sources then work together to feed the frontal splay ahead of the channel and taper channel extension. Data from repeat bathymetric scans showed that the total volume and rate of eroded bed material both increased with increasing slope. We therefore hypothesize that the addition of the extra bed material creates a sediment overloading condition were the capacity to move sediment is overwhelmed in the downstream direction by supply, and that the rate of increase in supply, and therefore slope reduction in the frontal splay, increases with slope.

The hypothesized overloading ahead of the extending channel is suggested as the primary mechanism limiting channel progradation in these subaqueous experiments. However, other mechanisms that could not be isolated or tested could be at work here and in other experiments. For example, it is possible that steeper slopes and the associated larger F_r numbers could work together with the sediment overloading to produce a fast decay in Q_t/Q_s by diluting the flow at a faster rate downstream through increased entrainment (eq. 3.6). Additionally, similar experiments in subaerial environments on fan-deltas (Sheets et al., 2007; Sittoni et al., 2014) have observed channel-to-lobe transitions triggered by channel-emergent bedforms that push the flow and sediment up out of the channel onto the laterally unconfined fan surface. Potentially yet another mechanism is seen in the alluvial fan experiments of (Hamilton et al., 2013) where channels extended to the fan front and initiated deposition from there. This underscores the potential variety of mechanisms at work in supercritical distributary systems to restrain channel extension and transition to deposition.

4.2.3 Hydraulic Jump Initiation

Hydraulic jumps have been considered important features on submarine fans, particularly at dramatic breaks in slope (e.g., Komar, 1971; Garcia and Parker, 1989; García, 1993; Gray et al., 2005). External slope breaks certainly have an important impact on the evolution of submarine fan systems (e.g., Fernandez et al., 2014). However, they were unnecessary in these experiments as hydraulic jumps formed upstream of the imposed basin slope break. Instead, the jumps was generated by the aggrading mouth bar causing a choked flow condition. The important aspect here being that the hydraulic jump feedback was initiated via a downstream boundary condition that was self-imposed by the system.

Other data that points to a deposit-forced choked flow condition comes from the similarity in the theoretical $\Delta\eta_{max}$ among experiments (fig. 4.4) and the regularity of the cycle timing. If the bars are indeed causing a choked flow condition, then the value of $\Delta\eta_{max}$ and the sediment supply rate should be important controls on cycle timing. All experiments in this study plot in a similar location with regard to $\Delta\eta_{max}$, and given the same sediment supply rate, would be expected to take a similar amount of time to reach the critical state for jump initiation. This appears to be reflected in figure 4.1 where the duration of channel stagnation before retreat is similar among experiments. An interesting aspect of figure 4.4 is that it shows that there is a large range of potential $\Delta\eta_{max}$ values in the velocity/density parameter space, ≈ 0 to 100 mm. Additionally, near the center of the plot, there is a narrow band of $\Delta\rho$ and U values where a jump could theoretically be triggered with a step height as low as fractions of a millimeter. Conversely, the region in the lower right of the plot, i.e., dilute flows with high velocities, would require a very large step, many times the flow thickness, to trigger a jump.

The values in figure 4.4 are specific to these experiments. For an example of a potential field-scale values, we estimate the step height needed to cause choke on the Golo Fan of the coast of Corsica (e.g., Gervais et al., 2004, 2006; Deptuck et al., 2008). Based on steepness of the basin and the Froude number estimation methods of Komar (1971) and Sequeiros (2012), it is very likely that the flows on the Golo would be supercritical. If we assume reasonable values for the densimetric Froude number, $F_r \approx 1.3$, and current thickness, $h \approx 20$ m, the critical step height estimate is $\Delta\eta_{max} \approx 1.2$ m. A deposit of this thickness is not that large considering the potential flow depths. Therefore it seems reasonable that a choke flow condition may be partially responsible the location of the Golo lobes.

The observed hydraulic jump features distinguish these experiments from other small-scale laterally unconstrained subaqueous fan experiments (e.g., Yu et al., 2006; Cantelli et al., 2011; Fernandez et al., 2014). These other experiments maintain subcritical flow and as such would not initiate hydraulic jumps even with a slope break (e.g., Fernandez et al., 2014). Furthermore, if a similar choked-flow condition was imposed on a system with subcritical flow, the response would be backwater, i.e., a raising of the upstream flow thickness, rather than hydraulic jump. This is potentially the behavior described by Cantelli et al. (2011) where downstream channel filling is said to drive increased levee building upstream.

4.2.4 Hydraulic Jump Scour and Deposition

Hydraulic jumps were a source of two distinct features: scour and substantial deposition. Scour occurred just upstream and within the hydraulic jump itself, while deposition occurred in the adjacent subcritical region downstream. Scour within the jump makes sense, as Sumner et al. (2013) pointed out that the vertical velocity fluctuations within a hydraulic jump are sufficient for sediment suspension, presumably of grains otherwise transported as bedload. The same was true in this study. The dominant transport mechanism in the channels was bedload based on observation z_* values. However, in regions of non-uniform flow, such as hydraulic jumps which are rapidly varied flow phenomena, u_* is not an indicative measure of velocity fluctuations (Schmeeckle and Nelson, 2003) which makes z_* a poor measure of vertical mixing conditions. Based on observation, grains were suspended up into the flow through the hydraulic jump and then rapidly deposited immediately downstream in the zone of subcritical flow. The deposition downstream was similar to what is observed in cyclic steps (e.g., Alexander, 2008; Kostic et al., 2010; Cartigny et al., 2014).

In our experiments, channel filling occurred as hydraulic jumps migrated upstream and created steep backsets that filled the channel as quickly as the jump retreated (fig. 4.3E). These deposits were mounded on top, forming a "steer-head" type capping geometry in cross-sectional view (fig. 4.3G). This depositional style stands in contrast to the style associated with backwater conditions in subcritical flow. Under backwater conditions, beds still accrete upstream, but they do so over a much longer reach and at a much lower angle (e.g., Hoyal and Sheets, 2009b).

Hydraulic jumps quarantined a large amount of the sediment and comprised a large amount of the total deposition in a particular lobe. A small portion of sediment was sometimes transported through the entire jump region, i.e., through the subcritical tailwater and out onto the lobe deposit, but was typically deposited quickly as in Macdonald et al. (2009). The flow downstream of the jump was initially completely depositional, but regained some sediment mobility as $\tau^* > \tau^*_{cr}$ on the lee of the lobe (fig. 4.3D). Though there was a slight ability to move sediment, the transport capacity was so small compared to the sediment supplied to the system (fig. 4.3B) as to be relatively unimportant over intermediate length scales. Once a location was passed over by the hydraulic jump the morphologic change was negligible (fig. 4.3E and G).

Chapter 5. Linking Hydraulic Properties in Supercritical Submarine Distributary Channels to Depositional Lobe Geometry

5.1 RESULTS

The experimental fans evolved over time through repeated avulsions which tended to behave consistently both within and among experiments. The data acquisition system and procedures allowed us to measure the resulting lobe geometric scales of width, length, and thickness as well as the hydraulic and length scales of the channels and currents feeding the deposits. A listing of all hydraulic and geometry data for the channels and lobes is given in table 5.1. Here we present the lobe geometry data resulting from avulsion cycles across experiments in both set A and B (table 2.1). We examine the relationships between key geometry length scales and test whether inclusion of channel hydraulic information can provide a link between the channel processes and the resulting deposit, and whether or not inclusion of this information can help to refine understanding of geometric length-scale relations.

5.1.1 Comparing Vertical Scales

Since both choked flow and hydraulic jumps are present during supercritical avulsion cycles, and both are responsible for deposition and lobe building, it is of interest to compare the vertical length scales associated with each. We hypothesized that lobe thickness would be a function of densimetric Froude number, and both the critical step height and sequent depth ratio can be expressed as a length scale normalized by the upstream flow depth as a function of Froude number (eqs. 2.14 and 2.15). It is of interest to determine the vertical scale we would expect to observe in depositional lobe components associated with choked flow and hydraulic jumps.

Table 5.1: Data gathered on lobe geometry and the associated channel hydraulics for all experiments.

F_r [-]	h_1 [mm]	L_l [mm]	W_l [mm]	H_l [mm]	θ_{exp} [deg]	L_l/W_l [-]	H_l/h_1 [-]
2.08	18	663	467	56	44	1.42	3.07
2.16	25	795	703	66	48	1.13	2.64
2.17	22	833	615	57	49	1.35	2.59
2.27	16	1025	890	50	54	1.15	3.17
2.01	15	1018	512	37	47	1.99	2.50
2.14	13	998	573	35	46	1.74	2.75
2.13	15	910	575	37	43	1.58	2.55
2.12	14	1026	545	38	39	1.88	2.65
2.21	17	1068	829	51	54	1.29	3.04
2.23	18	1161	891	48	45	1.30	2.67
1.81	22	1292	867	55	34	1.49	2.50
1.88	23	958	822	64	53	1.17	2.78
1.87	22	1053	821	60	49	1.28	2.73
1.75	14	1009	731	34	39	1.38	2.42
1.74	23	882	611	44	39	1.44	1.91
1.77	21	860	685	39	50	1.26	1.86
1.71	13	963	759	29	49	1.27	2.15
1.65	14	806	472	22	37	1.71	1.57
1.68	20	595	430	42	21	1.38	2.10
1.62	16	493	281	28	33	1.75	1.75
1.86	18	974	753	34	39	1.29	1.92
1.84	12	734	671	32	61	1.09	2.60
1.89	18	1199	812	42	45	1.48	2.33
1.75	15	873	507	35	27	1.72	2.33
1.75	16	807	554	29	25	1.46	1.81
1.71	14	679	371	36	26	1.83	2.57
1.67	18	766	633	31	60	1.21	1.72
1.20	12	773	477	16	22	1.62	1.30
1.18	12	649	397	14	29	1.63	1.17
1.48	21	864	538	32	35	1.61	1.52
1.51	13	939	622	22	39	1.51	1.70
1.47	19	665	351	31	27	1.89	1.63
1.43	16	847	553	26	44	1.53	1.63
1.44	12	593	306	23	21	1.94	1.92
1.41	15	681	317	24	22	2.15	1.60
1.38	15	951	568	21	40	1.67	1.40
1.41	15	848	461	23	36	1.84	1.55
1.67	14	1057	774	25	43	1.37	1.82
1.62	13	854	537	26	22	1.59	1.96
1.66	14	566	314	27	28	1.80	1.99
1.62	13	632	357	24	25	1.77	1.90

Continued on Next Page...

Table 5.1: (continued)

F_r [-]	h_1 [mm]	L_l [mm]	W_l [mm]	H_l [mm]	θ_{exp} [deg]	L_l/W_l [-]	H_l/h_1 [-]
1.55	12	677	407	26	28	1.66	2.17
1.50	12	801	593	17	43	1.35	1.42
1.46	10	984	631	20	45	1.56	2.05
1.48	14	868	551	26	35	1.58	1.86
1.38	15	929	500	25	35	1.86	1.67
1.42	15	677	373	26	37	1.82	1.73
1.48	20	670	373	42	44	1.80	2.10
1.46	17	682	283	28	29	2.41	1.65
1.31	16	941	499	23	37	1.89	1.44
1.25	17	511	251	26	33	2.04	1.53
1.87	16	1148	584	34	44	1.97	2.13
1.82	15	857	439	33	46	1.95	2.20
1.83	16	1034	635	37	48	1.63	2.31
1.78	15	781	485	34	45	1.61	2.27
1.80	15	836	364	32	47	2.30	2.13
1.72	14	1188	561	26	43	2.12	1.86
1.67	21	1016	439	35	33	2.31	1.67
1.61	18	458	219	33	38	2.09	1.83
1.58	16	726	417	28	49	1.74	1.75
1.59	12	710	337	22	46	2.11	1.83
1.62	10	451	220	19	38	2.05	1.90
1.63	12	477	345	26	51	1.38	2.17
1.61	10	713	429	18	52	1.66	1.80
1.92	17	775	438	32	51	1.77	1.88
1.96	18	826	371	38	44	2.23	2.11
1.67	12	1121	561	22	50	2.00	1.83
1.31	10	431	263	12	33	1.64	1.20
1.87	13	624	312	27	47	2.00	2.08
1.62	13	564	270	22	44	2.09	1.69
1.45	14	790	338	20	32	2.34	1.43
1.35	10	782	368	18	40	2.13	1.80
1.36	11	704	312	16	34	2.26	1.45
1.38	13	758	550	18	29	1.38	1.38

Both equation 2.14 and 2.15, for normalized critical step height and sequent depth respectively, are plotted in figure 5.1. The sequent depth from hydraulic jumps observed by García (1993) for both density currents (DC) and turbidity currents (TC) along with the field-observation of Sumner et al. (2013) are also shown. It is

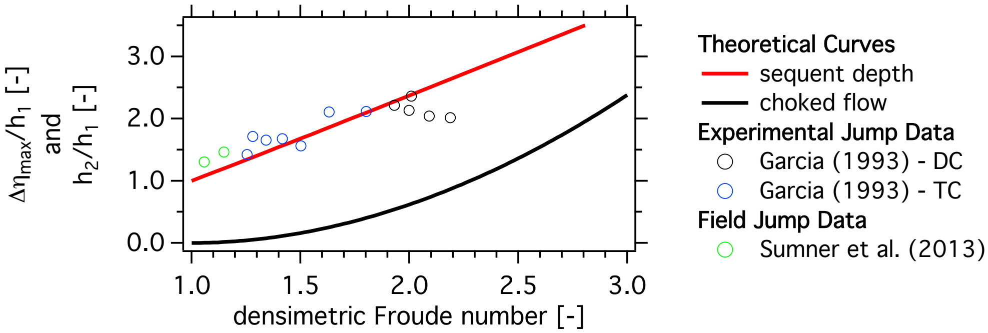

Figure 5.1: Relationship between Froude number and: (1) maximum obstacle height for choked flow normalized by upstream flow depth, $\Delta\eta_{max}/h_1$, and (2) hydraulic jump sequent depth ratio, h_2/h_1.

evident that a hydraulic jump creates a larger tailwater depth than the thickness of an obstacle associated with the choked flow criteria. This is a relatively obvious outcome, the jump must be larger than the obstacle since the only reason a jump forms is to traverse the obstacle, however this plot gives nice context as to how much larger a jump is than the obstacle causing it. This also tells us that if a hydraulic process is responsible for setting the maximum lobe thickness, the hydraulic jump is most likely responsible provided sediment is suspended in the jump.

5.1.2 Geometric Relationships

Here we present the overall lobe geometries measured during these experiments and their relationship to other experimental and field studies. Figure 5.2 shows the relationship between various geometric properties. Other data sets included are: Fernandez et al. (2014) (experiments), Covault and Romans (2009) and Deptuck et al. (2008). Solid lines correspond to trend-lines published by the authors with markers of the same color. Note that the trend-line in panel A for Fernandez et al. (2014) and Deptuck et al. (2008) plot in the same location. Looking first at the lobe planform dimensions, figure 5.2A shows L_l versus W_l. Regression analysis on our data gives a relationship of $W_l = 0.60L_l$. This is very near the relationships in other studies. The trendlines published by Fernandez et al. (2014) (experiments; $W_l = 0.58L_l$) and

Deptuck et al. (2008) (Golo Fan; $W_l = 0.59L_l$) are very similar to each other and to this study. The trend published by Covault and Romans (2009) deviates from the others at experimental scales because they use a non-zero y-intercept in calculating the fit ($W_l = 0.2595L_l + 11.677$, in kilometers). Regression was done on this data with a forced intercept of zero and the relationship is $W_l = 0.61L_l$, again very near the other published values. This is an interesting outcome given that systems that are four orders of magnitude apart in spatial scale.

Figures 5.2B-E show various relationships between the vertical lobe dimensions and horizontal lobe dimensions. H_l versus A_l is shown in figure 5.2B for this study along with others. The data from this study does not fit with any of the trends and is even set apart from the experimental data of Fernandez et al. (2014). The results are similar when comparing H_l to L_l (fig. 5.2C) or H_l to W_l (fig. 5.2D). This makes sense as the components of A_l are L_l and W_l. Regression on the interrelationship between the linear vertical and planform dimensions gives $H = 0.056W$ ($R^2 = 0.71$) and $H = 0.034L$ ($R^2 = 0.37$) for this study. Unlike the similar relationship between L_l and W_l across scales, H_l versus W_l or L_l have relationships approximately an order of magnitude different. For instance, $H_l/W_l = 0.056$ for the case of our study but is $H_l/W_l = 0.0016$ for the Golo Fan data (Deptuck et al., 2008). Finally, figure 5.2E shows the relationship between H_l/A_l and L_l/W_l. Because the dimensions on the vertical axis are [1/L] this type of plot becomes an effort in considering the scale of the system. Each data set shows a range of L_l/W_l values with a segregation along the vertical direction based on system scale. Prélat et al. (2010) used this type of plot to discriminate between confined and unconfined lobes; here it is solely an indication of scale. Overall, relationships between the vertical lobe dimension and planform lobe dimensions are not as strong as the relationship between the two planform variables.

A potential way to consider a connection with distributary channel properties is to relate the lobe thickness, H_l, to the upstream channel thickness, h_1. This

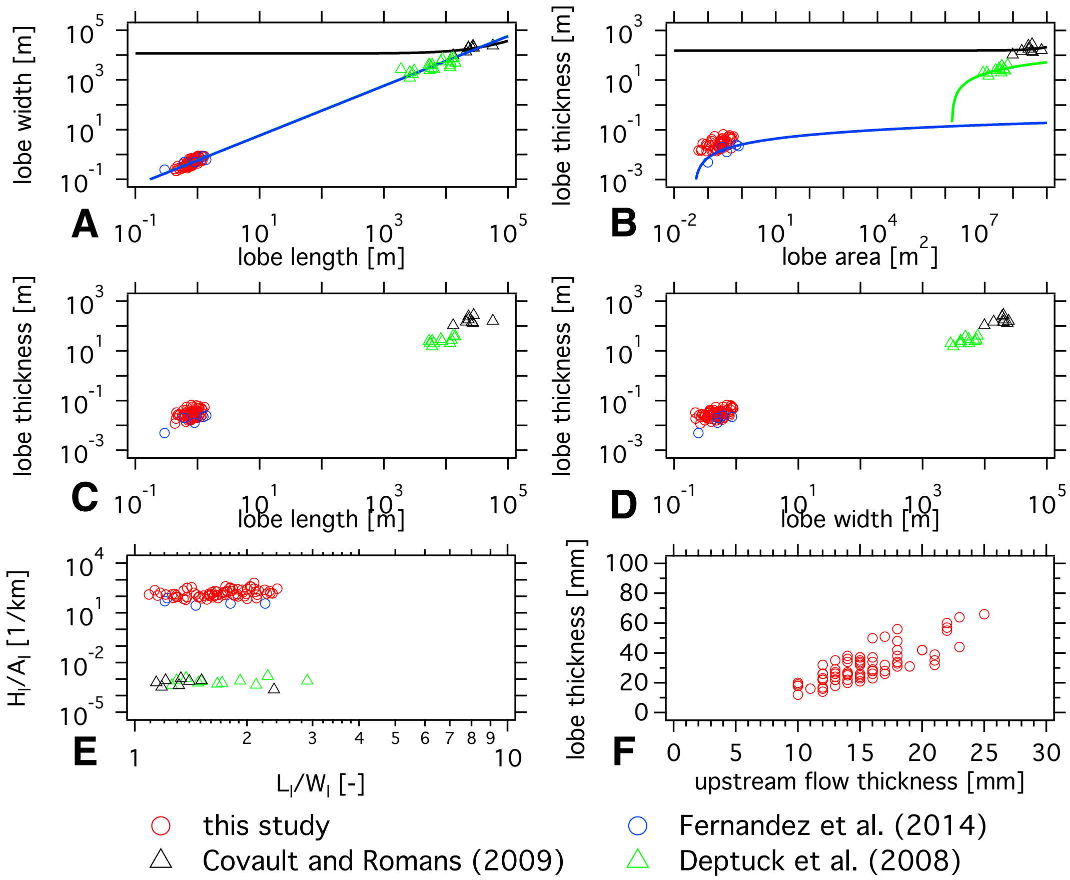

Figure 5.2: Various geometric relationships of lobe deposits: (A) W_l vs. L_l; (B) H_l vs. A_l; (C) H_l vs. L_l; (D) H_l vs. W_l; (E) H_l/A_l vs. L_l/W_l; and (F) h_1 vs. H_l.

relationship is shown in figure 5.2F. There is an obvious positive correlation between h_1 and H_l, though there is scatter. Since this is only a relationship between the thickness of two architectural elements of submarine fan systems, the relationship can potentially be refined by including hydraulic variables and the associated processes that relate channels and lobes.

5.1.3 Hydraulics-based Geometric Relationships

Instead of considering only interrelated geometric properties, the goal of this study was to consider how lobe geometries are potentially controlled by process-based parameters. Hydraulic jumps were common features in observed avulsion cycles and here we give an overview of the jumps observed during the submarine fan experiments and their relationship to lobe deposits. As mentioned in a previous section, the vertical scale associated with hydraulic jump is substantially greater than that associated with the choked flow condition that is also present in avulsion cycles (fig. 5.1). This by no means should minimize the importance of the choked flow bar height; without this condition the hydraulic jump would not initiate. Instead, it highlights the importance of the post-jump deposition with respect to the total lobe composition.

Hydraulic jumps formed at the channel to lobe transitions and constituted the bulk of sedimentation throughout avulsion cycles. Figure 5.3 shows a schematic view of the observed hydraulic jumps. A hydraulic jump typically had four regions of morphologic interest in these experiments as numbered in figure 5.3. The first was the channelized supercritical flow upstream of the hydraulic jump. Because the flow was supercritical, the current had no information regarding the upcoming jump and thus persisted at approximately steady and uniform conditions. The second region was the hydraulic jump itself. Two important things happened here: (1) the current interface increased in elevation and (2) the bed was scoured. The third region was the downstream subcritical section where the majority of sedimentation occurred. Sediment otherwise transported as bedload in the upstream channel was suspended in the hydraulic jump and could not continue as suspended load in the subcritical region and was therefore deposited. The fourth and final region was the sheet-like flow field that persisted downstream of the jump. Because of the small current thicknesses and still high slopes on the front of the lobe, the flow typically became again supercritical.

As shown in figure 5.3, much of the subcritical tailwater section became deposited sediment, i.e., much of the vertical length h_2 was filled with sediment. Since hydraulic jump related deposition was the most significant source of avulsion cycle deposition, we hypothesize that the maximum lobe thickness, H_l, should be near the post-jump subcritical flow depth, h_2. Conservation of momentum tells us that the sequent depth

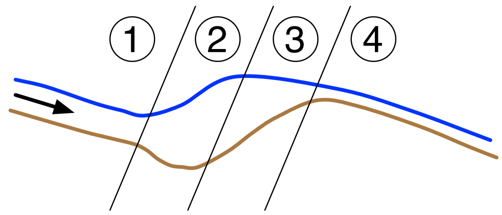

Figure 5.3: Cartoon depiction of hydraulic jump region: (1) upstream supercritical flow; (2) the actual hydraulic jump; (3) downstream subcritical zone; (4) the expanded flow region over the lobe.

ratio, h_2/h_1, scales with F_r, so H_l/h_1 should also scale with F_r. Figure 5.4 considers the relationship between H_l/h_1 and F_r. The data shows a positive correlation between H_l/h_1 and F_r as would be expected. The solid line in figure 5.4 is that of equation 2.15 which is not a data fit, but the analytical solution for an open channel flow hydraulic jump. Our experimental data approximately tracks equation 2.15. Base on this outcome, we can confirm our hypothesis regarding lobe thickness as a function of Froude number as there is indeed a positive correlation.

While figure 5.4 shows the relationship between Froude number and deposit thickness, figure 5.5 shows two planform relationships. There is a weakly negative relationship between L_l/W_l and F_r (figure 5.4A) given by $L_l/W_l = 2.44 - 0.44F_r$, $R^2 = 0.13$. This means that for a given L_l, as F_r increases, W_l increases. In this same sense, there is a positive relationship between the expansion angle, θ_{exp}, and F_r (fig. 5.4B) given by $\theta_{exp} = 7.4 + 19.3F_r$, $R^2 = 0.28$. Given the low coefficient of determination values and the relatively low slopes of the best-fit lines, the trends in planform geometry variables as a function of densimetric Froude number appear to be relatively weak in comparison to the vertical direction. This also refuted the hypothesis set forth regarding F_r vs. L_l/W_l in that the correlation was negative instead of positive.

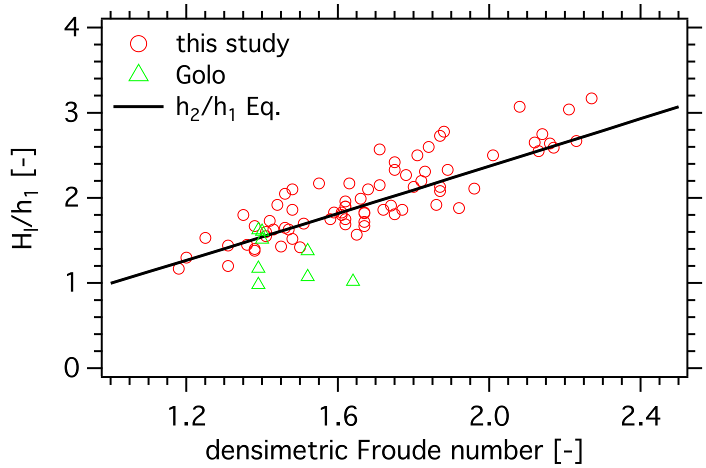

Figure 5.4: Ratio between maximum lobe thickness and upstream flow depth, H_l/h_1, as a function of F_r. Approximate H_l/h_1 data for the Golo system (Gervais et al., 2004; Deptuck et al., 2008) is also shown.

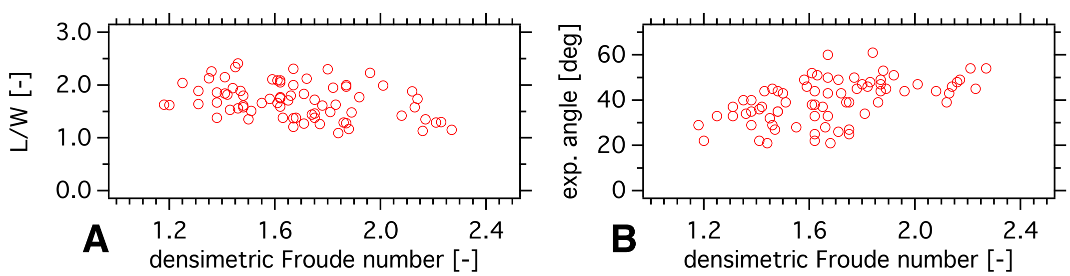

Figure 5.5: Planform geometric properties as a function of densimetric Froude number for: (A) L_l/W_l and (B) θ_{exp}.

5.1.4 Jump Equation at Field Scale - An Example from the Golo Fan

Figure 5.4 includes data from a field-scale case alongside the experimental data. A natural system that seems particular apt for comparison with these experiments is the Golo fan (Gervais et al., 2004, 2006; Deptuck et al., 2008). This system has a high enough slope such that it is assuredly supercritical and provides a good basis for comparison given the previous work on lobe geometry by Deptuck et al. (2008). Here we use this system to show an example application of this method for estimating lobe thicknesses based on available channel data. The thickness of lobe C1 from Deptuck et al. (2008) will here be estimated and compared to the known value.

The methodology is based on three important variables: h_1, F_r, and H_l. The flow thickness, h, was estimated from the St. Damiano channel in profile 7 of figure 5 in Gervais et al. (2004) to be 15.6 meters. This estimate assumes the channel body thickness mimics that of the flow thickness, i.e., bankfull conditions. The other important parameter needed to estimate H_l is Froude number. The Froude number was estimated two ways: (1) by the normal flow approximation (Komar, 1971) and (2) the method published by Sequeiros (2012). The latter is given by

$$F_r = [0.15 + \tanh(7.72 S^{0.75})][1 + w_s/u_*]^{1.1}[C_f(1+\alpha)]^{-0.21}, \tag{5.1}$$

where S is the slope, w_s is the sediment settling velocity for turbidity currents and $\alpha = \tau_i/\tau_b$ is the ratio between interfacial stress (τ_i) and bottom boundary stress (τ_b). Sequeiros (2012) also established a relationship for α as a function of Froude number given by $\alpha = 0.15 F_r^{3.95}$. A second Froude number estimate was made using

$$F_r = \sqrt{\frac{\sin\theta}{C_f(1+\alpha)}}, \tag{5.2}$$

where θ is the angle of bed inclination above horizontal. This is a normal flow approximation which assumes the driving gravitational force is in balance with the resisting forces at the upper interface and the bottom boundary. This is a specialized case but is nonetheless the hydraulic state which systems tend toward. The slope for this example was estimated from the contours in Deptuck et al. (2008) figure 1 to be 0.014 making θ equal to 0.802 degrees. The friction factor was taken to be $C_f = 0.005$. Using equation 5.1 we get $F_r = 1.34$ and using equation 5.2 we get $F_r = 1.36$, two similar estimates.

Based on the F_r estimate, H_l/h_1 was calculated from equation 2.15, using H_l as a surrogate for h_2, to be 1.48. This makes the estimate for H_l to be 23.2 which is near the actual value of 25.2. Though the example here shows the estimation of H_l

given h and F_r, the method could also be used to estimate channel flow conditions, primarily Froude number, based on h and H_l estimates from the sedimentary record.

5.2 DISCUSSION

5.2.1 Hydraulic Jump Sensitivity

Equation 2.15 is a relatively good representation of lobe thickness data from our experiments (fig. 5.4). However, the "classic" hydraulic jump equation is subject to several restrictive assumptions: $S = 0$, zero friction, rectangular channel, and open channel flow. Natural environments along with morphologically active experiments such as this study are clearly much more complicated. Potential complications can include bed discontinuities, bed slope, bed friction, and/or expansions or contractions. Conservation of momentum holds through a hydraulic jump regardless of circumstances, however the other momentum sources and sinks should be considered. Here we look at modified hydraulic jump equations to consider the effects of various complications on the sequent depth ratio. This is not meant to be an exhaustive examination, but a brief look at potential sources of deviation from the "classic" hydraulic jump equation.

First, considering the effects of bed friction, Carollo et al. (2007) developed a sequent depth ratio equation which is given by

$$\frac{h_2}{h_1} = \frac{\sqrt{1 + 8(1 - 2/\pi \arctan(0.8(k_s/h_1)^{0.75}))F_{r1}^2} - 1}{2}, \tag{5.3}$$

where k_s is the roughness length scale and k_s/h_1 is therefore the relative roughness. Their study used a horizontal flume with a gravel bed which created relative roughnesses within the range 0 to 2.0. The sequent depth ratio calculated from equation 5.3 is plotted for a variety of relative roughness values in figure 5.6. h_2/h_1 is not appreciably different across a range of Froude numbers and relative roughness values.

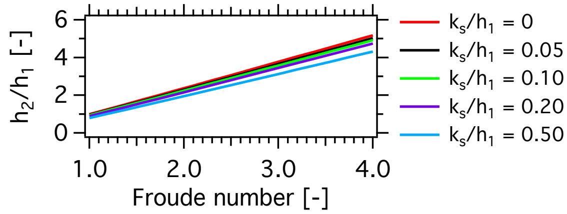

Figure 5.6: Hydraulic jump sequent depth ratio as a function of Froude number for different relative roughness values.

If we take conditions from our experiments where the effect of including roughness would be greatest, $h_1 \approx 10$ mm, $k_s/h_1 = 0.025$, and $F_r \approx 2.3$, equation 2.15 would calculate $h_2/h_1 = 2.79$ while equation 5.3 calculates 2.74, a difference of 0.05. Given that the maximum difference we would expect from these experiments due to the exclusion of skin friction is small, its omission in the classic jump formulation is not a significant source of error.

Beyond the inclusion of bed roughness, the momentum balance between the upstream and downstream section can be further generalized to include other complicating factors mentioned above. Here we consider the effects of a channel bed step, a channel expansion or contraction, and bed inclination (fig. 5.7). We take $\lambda = L_j/h_1$, $D = h_d/h_1$, and $B = b_1/b_2$, where L_j is the hydraulic jump length, h_d is the step height, and b_1 and b_2 are the upstream and downstream channel widths respectively. The basic formulation for conservation of momentum as applicable for the expanded analysis can be written as

$$F_1 - F_2 - F_f - F_d + W_w \sin\theta = \rho Q(U_2 - U_1), \tag{5.4}$$

where $F_i = 1/2\gamma h_i^2 b_i$ ($i = 1, 2$, for the upstream and downstream section respectively), $F_f = 1/2\rho C_f U_1^2 \lambda(b_1 + b_2)$, $F_d = 1/2\rho C_d h_d b_1 U_1^2$, W_w is the weight of the water, Q is the volumetric flow rate, $\gamma = \rho g$ is the fluid unit weight, C_f is the skin friction factor, and C_d is a form friction factor associated with the step. After plugging in these expressions and simplifying, an implicit combined equation for sequent depth ratio,

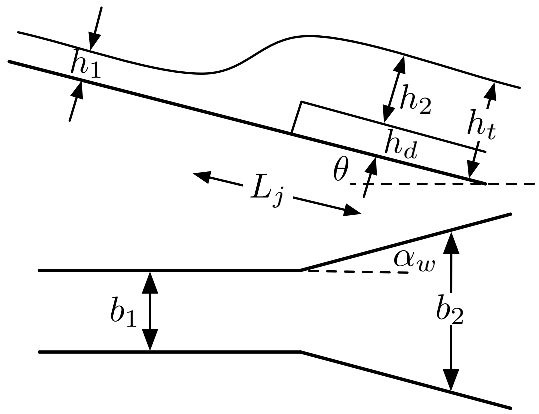

Figure 5.7: Definition sketch for analytical treatment of hydraulic jumps in longitudinal section (top) and plan-view (bottom).

h_2/h_1, can be written as

$$\left(\frac{h_2}{h_1}\right)^3 (2B^2\cos\theta) - \left(\frac{h_2}{h_1}\right)^2 ((1+B)B\lambda\tan\theta) + \left(\frac{h_2}{h_1}\right)[2C_f F_r^2(1+B)B\lambda\sec\theta + 2C_d DBF_r^2 - 2B\cos\theta - (1+B)\lambda B\tan\theta - 4BF_r^2] + 4F_r^2 = 0. \tag{5.5}$$

Given the conditions of the classical hydraulic jump, i.e., horizontal bed, no expansion, no obstacle, equation 5.5 reduces to equation 2.15.

Given an equation which includes several parameters absent in the "classic" hydraulic jump relationship, we consider how the different parameters in equation 5.5 affect the sequent depth ratio. Figure 5.8 shows the effects of S, B, and D on h_2/h_1. Slope can become important with higher slopes especially at lower Froude numbers (fig. 5.8A). This makes this relationship less significant given that higher slopes typically sustain higher Froude numbers were the deviation is diminished relative to equation 2.15. The effects of a change in channel section (fig. 5.8B) are much more obvious than those of slope. For $B > 1$, i.e., a jump occurring through an expansion, h_2/h_1 is substantially smaller than predicted by equation 2.15. Conversely, for $B < 1$, i.e., a jump occurring through a contraction, h_2/h_1 is substantially higher

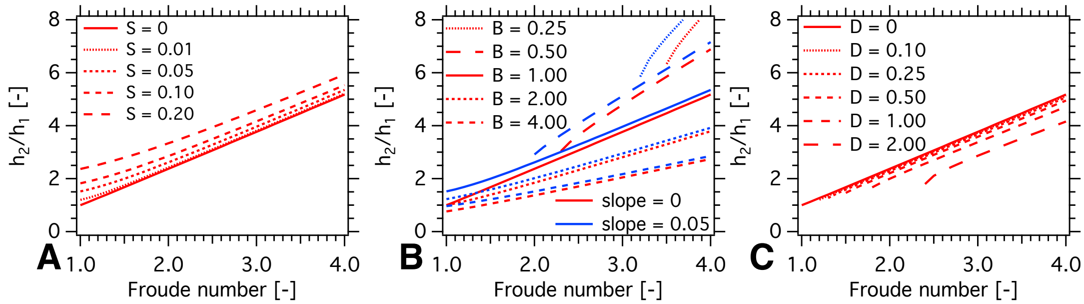

Figure 5.8: The effect of various parameters on the h_2/h_1 vs. F_r parameter space: (A) as a function of bed slope; (B) as a function of expansion/contraction ratio; and (C) as a function of relative step height.

than predicted by equation 2.15. Finally, the effects of a bed step within the hydraulic jump are shown in figure 5.8C. A step does not have a large effect on the sequent depth but does restrict the range of Froude numbers where a solution exists. One aspect of note regarding the presence of a step is that the downstream depth is h_2 in figure 5.7 meaning the total rise in water-surface elevation is more than solely $h_2 - h_1$.

The major outcome from this sensitivity exercise is that it helps to confirm the behavior shown in figure 5.3. Looking at hydraulic jump solutions from equation 5.5 and experiments it appears the hydraulic jump sets the step height rather than the other way around. This is to say that the sediment is trapped in the downstream subcritical flow resulting from the jump rather than in the jump itself. Because of this, the mounded deposit does not act as a step within the hydraulic jump. In essence the jump is a channelized jump that forces an expansion because of water surface elevating outside the channel. This means that the important aspects of the hydraulic jumps are Froude number and slope and the less significant aspects are step size, expansion, and jump length (fig. 5.8).

That there is no step or expansion is perhaps the reason why equation 2.15 fits the data so well despite the violated assumptions. As shown before, the balance of momentum equation (eq. 5.5) containing all potential terms is far more sensitive to changes in channel section and bed discontinuities than bed inclination and bed friction. Hydraulic jumps are observed to be channelized features, both in the jump itself and in the immediate tailwater. In this way the steeply inclined backset beds are emplaced as a function of the jump though the beds themselves do not impact the jump.

Of note is that the relationships discussed thus far regarding hydraulic jumps have been for open-channel flows with modifications for stratified flows coming only from replacement of g with g'. The major difference between open channel hydraulic jumps and density current hydraulic jumps is the role of entrainment. Because density currents entrain ambient fluid into the top of the current the sequent depth ratio of a hydraulic jump should be larger than in the open channel case. For normal or gradually varying stratified flow there exists an entrainment coefficient, e_w, typically reported as a function of densimetric Froude number (Ellison and Turner, 1959; Parker et al., 1987). Rapidly varied flow is a significant deviation from a developing density current on a slope and as such presumably has its own entrainment coefficient that is higher than e_w. Obviously the effects of density stratification are an important aspect for hydraulic jump behavior. However, for the sake of simplicity, hydraulic jump behavior will be considered to be similar in density currents to open channel flows under the assumption that the added effects of entrainment will be relatively minor compared to the increase in flow depth associated with the jump itself.

5.2.2 Process-Based Geometric Relationships

Studies that have previously undertaken a geometric consideration of depositional bodies have frequently forwarded relationships among different geometric properties, e.g., L_l, W_l, H_l, A_l (e.g., Saller et al., 2008; Deptuck et al., 2008; Covault and Romans, 2009; Prélat et al., 2010). Current methods for estimating sub-seismic geo-body dimensions consists largely of analog-type studies. An analog system with similar features to that of the system of interest is identified and the dimensions and ratios of the analog system are attributed to the system of interest. This is a reasonably valid exercise given that similar systems should have similar features, but would typically not be general enough to accommodate the range of possibilities in many other systems. Here we consider a relationship between the process enacting landform development and the ensuing sedimentary product. This is perhaps a better way to create a general characterization of landform scaling on a process-to-product basis. It also provides a more ubiquitous predictive power than interconnected geometric properties in that it overtly incorporates the processes at play.

As mentioned before, hydraulic jumps are a common phenomena during supercritical avulsion cycles and a primary contributor to lobe deposition. Figure 5.4 shows the relationship between H_l/h_1 and the F_r in the channel. These values are positively correlated and are surprisingly similar to the sequent depth prediction of equation 2.15. This appears to work given the physical current thickness downstream of the jump, i.e., that on top of the deposit, is a fraction of that the total jump height and that the balance of vertical space is comprised of deposition. The relationship between normalized lobe thickness and Froude number is perhaps the most reliable of geometric relationships we observed given that it is tied to the flow properties. This is also a reason for optimism in extending this type of relationship to field scales.

It makes sense that the lobe thickness should be related to the channel depth, a small channel would not deposit a big lobe, but our data indicates that for these supercritical systems h_1 is not sufficient information to predict H_l (fig. 5.2F). Instead it is dependent on the hydraulic regime in the channel and associated hydraulic process. As an example of this considered here, equation 2.15 would predict $H_l/h_1 = 1.27$ and 1.96 for $F_r = 1.2$ and 1.7 respectively. For a natural channel with a thickness of 20 m this equates to an H_l value of 25.4 and 39.2 respectively - a 13.8 m difference. Knowing, or at least having an estimation of F_r can help refine an estimation of H_l based on channel depth.

It is imperative to note that the relationships between H_l, h, and F_r shown here are only valid for systems with supercritical flow. The method is predicated on the hydraulic jump behavior observed on these fans which will not occur where subcritical flow persists locally.

5.2.3 Planform Relationships

Though the vertical lobe dimensions appear well constrained by the upstream flow properties, the planform geometry does not appear to be as strongly tied to Froude number (fig. 5.5). We originally predicted that L_l/W_l would be positively correlated with F_r. The logic was that more inertial flows, i.e., those with higher F_r, would lead to more elongate lobe deposits. This was not the case here. One longitudinal length scale that is a function of F_r is hydraulic jump length, L_j. Though there is a positive relationship between L_j and F_r (analogous to open-channel flows), the hydraulic jump length is only a small fraction of the total lobe length. Overall lobe length appears to be a weak function of Froude number and more strongly controlled by how far the hydraulic jump retreats upstream prior to flow avulsion. Within each avulsion cycle, after the hydraulic jump initiates at a basinward location, the jump propagates upstream before the channel is eventually relocated. Each lobe therefore had a length that was approximately bounded on the downstream end by the location where channel extension ceased at the beginning of the cycle, and at the upstream end by the farthest upstream the jump retreated prior to avulsion. Width, as with length, appears to be a weak function of Froude number and more related to how much lateral migration there is prior to jump initiation. The lateral migration ahead of jump initiation sets at least a minimum width that a particular lobe will attain at its most downstream location.

Despite the dependence on lateral migration and upstream retreat, L_l/W_l and θ_{exp} still have a weak dependence on F_r that has a potential physical explanation related to the hydraulic jump behavior. The vertical displacement of the density current interface within the jump is a function of the incoming Froude number. Also, the majority of this space is filled with sediment. If we assume bankfull conditions just upstream of the jump, the distance above the channel bank the sequent depth reaches is a function of F_r. As noted, the majority of the sequent depth is quickly filled with sediment. The greater the emergence from the channel, the greater the local transverse slope, the greater the initial lateral velocity, and the wider swath over which sediment is quickly cast. Another potential consequence of greater channel emergence is a higher rate of lateral buoyant spreading of the density current just downstream of the jump. The greater the residual current thickness outside above the channel, the greater the lateral gravitational component of the buoyant spreading force and the quicker the width will increase. Either of these processes, topographic shedding or buoyant spreading, or a combination of both, would create larger lateral velocities just outside the hydraulic jump and could explain the positive relationship observed between θ_{exp} and F_r (fig. 5.2B). This relationship for θ_{exp} transitions to the linear dimensions of the deposit in that for a given L_l, an increase in θ_{exp} would correspond to an increase in W_l. This would then explain the observed negative relationship between L_l/W_l and F_r in figure 5.2A. The relationships between θ_{exp} and L_l/W_l and F_r persist across the range of observed F_r but with scatter. Perhaps the linear dimensions L_l and W_l were not dictated by F_r, but retained an imprint of the jump behavior as a function of F_r in θ_{exp} and L_l/W_l.

The negative relationship observed between F_r and L_l/W_l stands in contrast to the work of Hoyal et al. (2003) where they were positively correlated. The difference between the two experimental trends can potentially be attributed to the difference in dominant sediment transport mode and the prominence of hydraulic jumps in our experiments. Sediment transport in our experiments is primarily bedload and the bulk of sedimentation is associated with hydraulic jumps. The difference in the Hoyal et al.

(2003) experiments is that there was substantial suspended sediment transport and hydraulic jumps did not detain considerable sediment quantities. Instead, sediment is dispersed within the expanding jet over a wide area and a length dependent on initial inertia. In our experiments, the distance from the inlet to sediment deposition is restrained by the hydraulic jumps encountered along the way.

In terms of interrelated geometric properties absent the hydraulic process, the relationship between L_l and W_l in figure 5.2A seems to work well. As with other published data sets, L_l and W_l are positively correlated. This is perhaps a bit of a self-fulfilling prophecy in that large sedimentary bodies are large in multiple directions, they'd look weird if they didn't. This is similar to saying people who wear large shirts often wear large pants, they'd look weird if they didn't. Though this is potentially helpful geologically in that one dimension could constrain a different dimension, it is not informative regarding the hydraulic conditions of the system. Here we look at relationships between the formative hydraulics and emplaced sedimentary bodies with an eye toward the mechanistic causation rather than correlations between geometric properties. This arises most strongly in the vertical direction.

5.2.4 Grain-size Limitations

The hydraulic jump behavior described here, scour in the jump and deposition in the subcritical tailwater, must have grain-size limitations. The grain size must be large enough such that the sediment is not simply transported through the jump as much of the fine sediment driving a turbidity current would be (e.g., Woods et al., 1998). The grain size must also be fine enough such that it is suspended by the jump for this jump scaling to work. If the sediment is not fully entrained, the expected sequent depth scaling will not hold and the resulting deposit will be less thick than the tailwater. The experiments here show the situation where sediment is transported as bedload but is entrainable in the jump and is rapidly deposited in the tailwater.

This results in a very thin flow on top of the mounded lobe deposit downstream of the jump which is further evidence of sediment being deposited within most of the tailwater depth.

Chapter 6. Hydraulic and Morphologic Evolution of Supercritical Submarine Fan Systems

6.1 RESULTS

Herein we present the results of the set B experiments outlined in table 2.1. The various experiments tended to exhibit similar behavior in terms of autogenic cyclic events and the longer-term trajectory in hydraulic variables and morphology. Here we report those trends and the associated trends in landform evolution and sedimentary stacking.

6.1.1 General Morphodynamic Behavior

The goal of this section is to present general fan behavior including flow organization and the depositional elements associated with avulsion cycles. As to terminology used herein, at any particular juncture during a submarine fan experiment the flow field could typically be delineated into a trunk channel, distributary channel, and lobe. These flow-field categories progress from proximal to distal though the absolute location of each transition was dynamic. Modifications in the distributary channel-to-lobe transition location was due to the mechanics of autogenic submarine avulsion. The flow field throughout the experiments can be summarized as either having a single or multiple distributaries (fig. 6.1). The single distributary configuration persisted when there was minimal flow outside of the well-channelized portion and the well-channelized portion was directly connected to the unchannelized flow field over the lobe (fig. 6.1A). The alternative was multiple distributary channels (fig. 6.1B). In this situation there existed a bifurcation or bifurcations that partitioned the flow properties along different distributaries, e.g., Q, Q_s. Though not a ubiquitous occurrence, the multiple distributary configuration often included a region of weakly

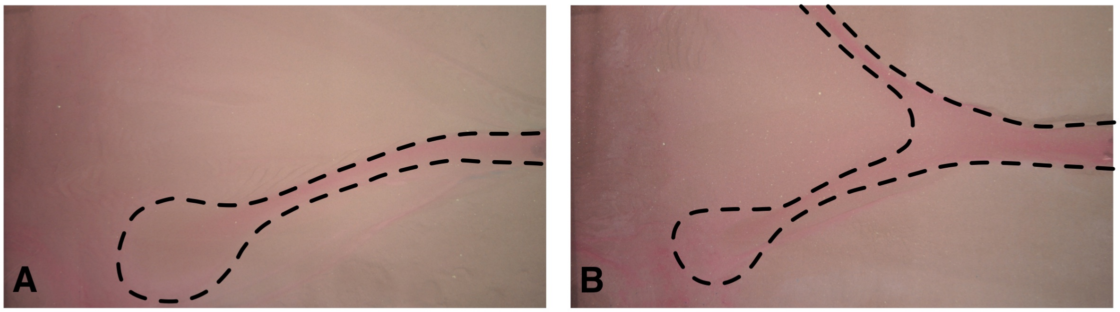

Figure 6.1: Typical hydraulic configurations: (A) single distributary channel connected to the trunk channel and (B) multiple active distributary channels not directly connected to the trunk channel.

channelized or unchannelized flow in the transition between the trunk channel and the distributary channels. Since this was a region of reduced velocity, there was often deposition in this area (fig. 6.1B).

The mechanics of supercritical autogenic avulsion were studied by Hamilton et al. (2015a); here we consider how those mechanics are translated into depositional bodies. Figure 6.2 shows a schematic view of erosion and deposition during avulsion cycles. There were three primary phases of avulsion cycles as it applies to the depositional record: (1) progradation, (2) aggradation, and (3) retrogradation (fig. 6.2). Progradational deposits (yellow in fig. 6.2) came from frontal splay deposition ahead of the prograding channel that downlapped the prior bathymetry. This mode of deposition was a relatively minor component of avulsion deposits. The flow field ahead of the extending channel was disperse and therefore cast sediment over a span multiple channel widths wide. The second stage of the cycle was aggradation (red in fig. 6.2). The progression of sedimentary stacking was not solely in the vertical direction as there was a component of lateral accretion during this phase. During this stage of the cycle, space was filled ahead of the stagnated distributary channel by aggrading the mouth bar to the choked flow condition and initiating the hydraulic jump. Lastly, retrogradational deposits (blue in fig. 6.2) were those associated with hydraulic jumps that filled and capped the scoured channel body with a steer-head type geometry. This retrogradational deposition created steep backset bedding indicative of hydraulic jumps. The depositional package outlined in figure 6.2 pertained to each avulsion cycle and therefore each lobe emplaced.

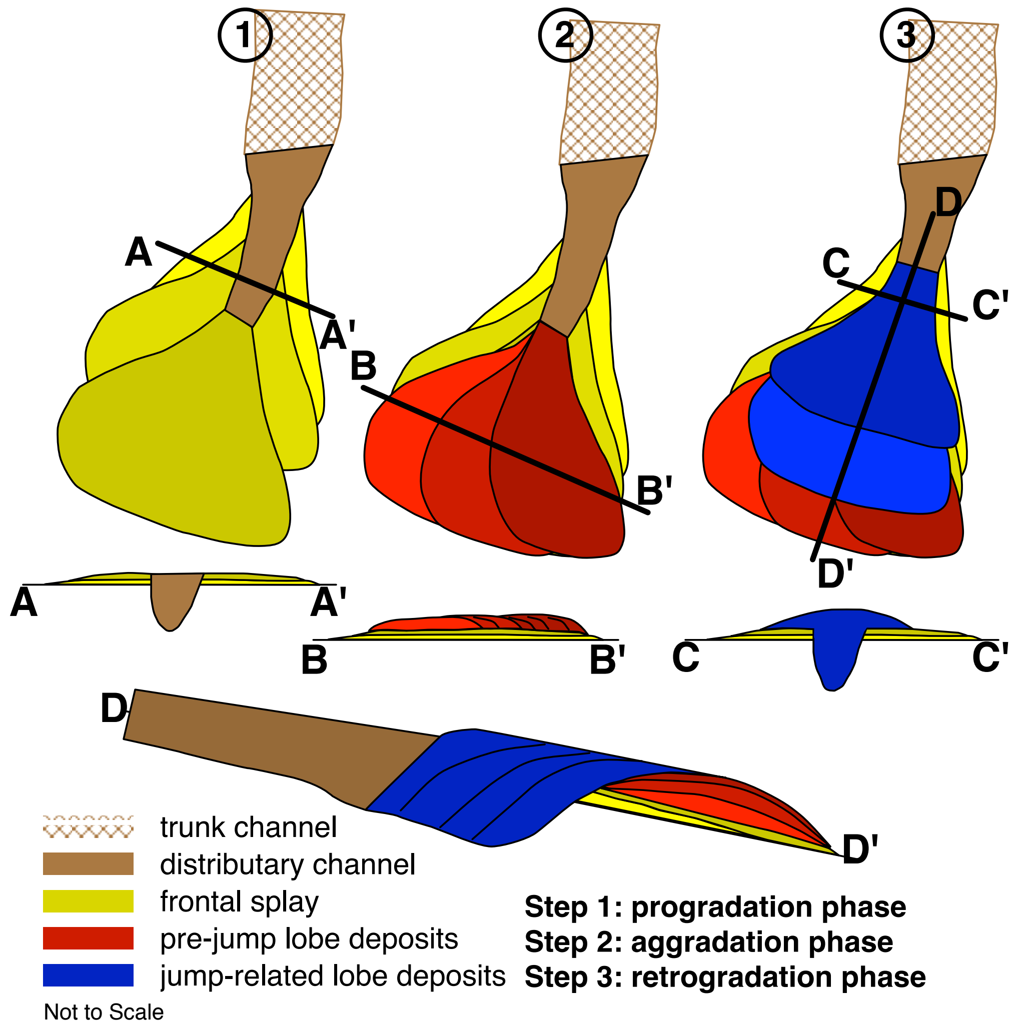

Figure 6.2: Cartoon of depositional packages through autocyclic events arising from: (1) progradation, (2) aggradation, and (3) retrogradation.

In looking at the trajectory of the system over multiple avulsion cycles, the most common behavior of each subsequent cycle was progradation beyond the previously emplaced lobe (fig. 6.3A). This was dominant when there was only one active or dominant distributary. A different behavior is shown in figure 6.3B when there were multiple distributaries active. These tended to have progradational behavior toward

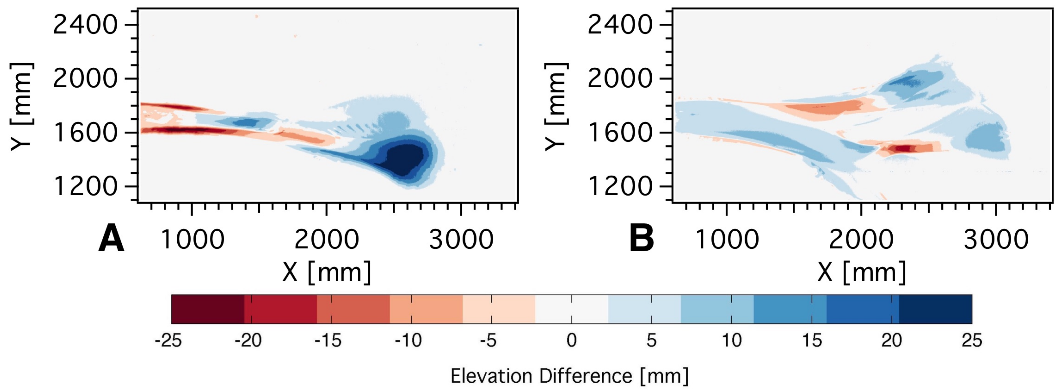

Figure 6.3: Bathymetric difference maps (Δt = 20min.) showing different stacking tendencies between avulsion cycles: (A) lateral and progradational stacking and (B) multiple distributaries with dispersed aggradation upstream.

the fan front and dispersed deposition behavior toward the fan apex (fig. 6.1B). Here the trunk channel was not directly connected to a particular distributary formed on the steep fan front. Each active distributary concurrently underwent the same incision, extension, stagnation, backfilling cycle that otherwise occurred with a single distributary. However, here the multiple distributaries were not always completely infilled as they were in the single distributary case. This was because the flow and sediment could be repartitioned from the upstream direction prior to completing a cycle.

6.1.2 Landform Evolution

In this section we will consider various aspects of the experimental submarine fan development and evolution. The location within the experimental domain of the data presented in the various graphs is shown in figure 6.4. Within the figure: (A) stars indicate the locations for data shown in figure 6.5, (B) location of transverse section shown in figure 6.11, and (C) location of the imposed depression for Fan10-B and the locations for the longitudinal and transverse sections shown in figure 6.8.

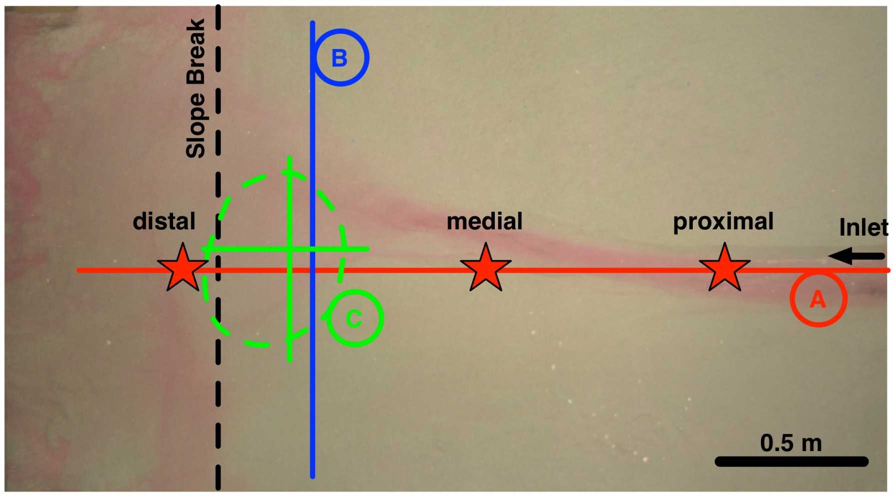

Figure 6.4: Location within the experimental domain of data shown in figures 6.5, 6.8, and 6.11.

Spatio-Temporal Variation in Slope

To consider the temporal evolution of slope on the fan surface, we looked at a few discrete locations. Figure 6.5 is an example of this type of analysis. This figure shows the variability in the longitudinal slope ($S = -d\eta/dx$) with respect to time. At $t = 0$ min, the slope at the proximal and medial locations was that of the initial imposed plate slope. This slope persisted up until the fan front reached that point into the basin when the slope began to increase in time. This was due to the particular point being on the basinward side of the active lobe deposits. The system was generally progradational meaning subsequent lobes were emplaced beyond the current depocenter which made the point of interest progressively more proximal on lobe deposits. This made the slope lower in time as the point of interest transitioned to the apex side of the lobe. As the system continued to prograde, the point of interest became the location of distributary channels and/or unconfined flow where the slope depended on the current flow configuration but was near an equilibrium slope.

Though the system tends toward the equilibrium slope where sediment was efficiently transmitted from the inlet to the depocenter, there where still fluctuations.

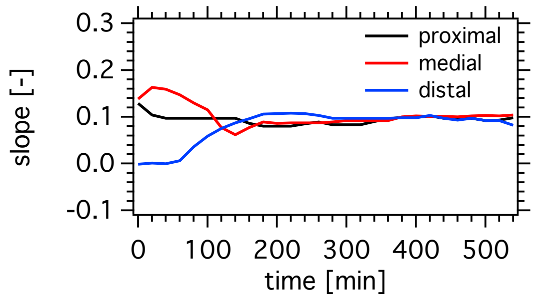

Figure 6.5: Local slope at a proximal, medial, and distal locations along the centerline of Fan02-B as a function of time. See figure 6.4 for the data locations.

Table 6.1: Long-term submarine fan evolution properties including equilibrium slope, S_{eq}, and average progradation rate, $\overline{u_{prog}}$.

Run	S_{eq} [-]	$\overline{u_{prog}}$ [mm/sec]
Fan01-B	0.086	2.14
Fan02-B	0.107	1.22
Fan03-B	0.128	1.03
Fan04-B	0.135	0.86
Fan05-B	0.145	0.96
Fan06-B	0.159	1.20
Fan07-B	0.172	0.57
Fan08-B	0.198	-
Fan09-B	0.208	0.54

This was often due to temporary sediment storage. The primary cause of sediment storage on the fan surface was associated with unchannelized deposition between the trunk channel and the resumption of well-defined channelization as was common during periods of multiple active distributaries (fig. 6.1B). Though sediment was contemporaneously deposited in the mid-fan region, much of that sediment was subsequently re-eroded and fed toward the fan front.

Overall Fan Trajectory

Each discrete avulsion cycle during these experimental fans contained progradational, aggradation, and retrogradational features. In considering the longer-term evolution of the system, the interest turns to how multiple cycles stack up. One way

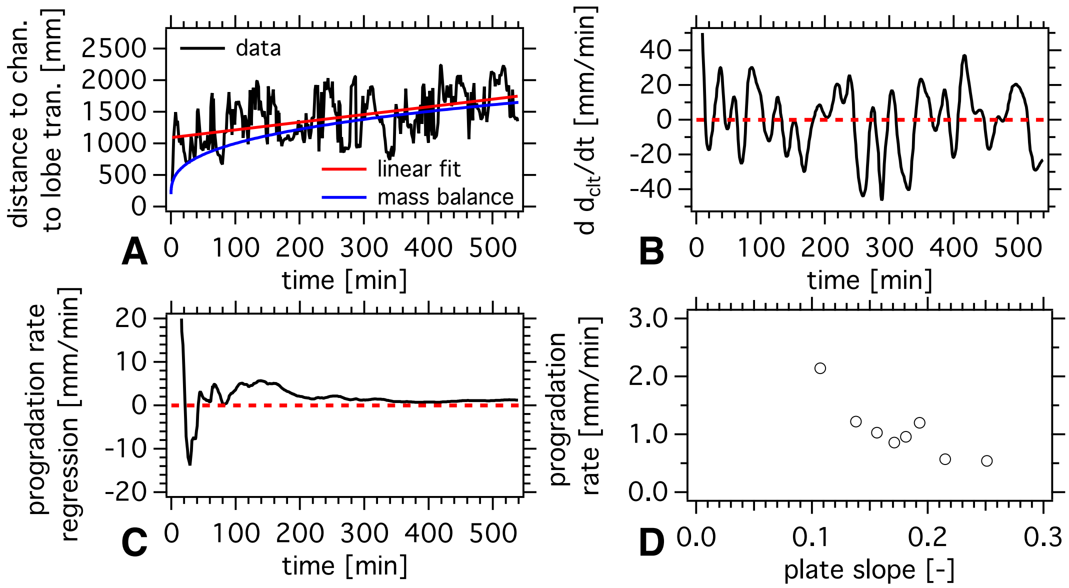

Figure 6.6: Trends in fan experiment progradation during Fan02-B.

to investigate the trajectory of the system is by plotting the distance to the channel to lobe transition, $d_{clt} = d_{clt}(t)$, as a function of time (fig. 6.6A). The trajectory of the system can be thought of two ways: as an instantaneous property or an average property. System trajectory, if considered as an instantaneous property, is shown in figure 6.6B. This is simply $d(d_{clt})/dt = u_{prog}(t)$, where u_{prog} is the rate of progradation. For this case, $u_{prog} > 0$ indicates progradation, $u_{prog} \approx 0$ indicates aggradation or lateral stacking, and $u_{prog} < 0$ indicates retrogradation. The forward and back nature of the avulsion cycles is apparent in the instantaneous sense of system trajectory.

The trajectory of the system can also be considered as a time-averaged property of the fan. Linear regression was done on each time series with a fit taking the form $\overline{d_{clt}} = d_0 + \overline{u_{prog}}t$ where $\overline{d_{clt}}$, where d_0 is the y-intercept of the time series regression and $\overline{u_{prog}}$ is the slope of the d_{clt} versus t regression which is the average rate of progradation. The value for d_0 was not forced to zero as was obviously the case since the channel did not exist at $t = 0$. However, letting d_0 self-stipulate was the more realistic solution given that the system quickly advanced beyond the inlet in the first few minutes of the experiment and was then dynamic from there.

For this case $\overline{u_{prog}} > 0$ indicates overall system progradation, $\overline{u_{prog}} \approx 0$ indicates net aggradation or lateral stacking, and $\overline{u_{prog}} < 0$ indicates overall system retrogradation. All the experiments in this study were net progradational. Taking the values for $\overline{u_{prog}}$ from each experiment, there is an inverse relationship with imposed slope, S_p (fig. 6.6D). This means that systems with larger imposed slopes advanced down-dip more slowly and remained perched on the imposed slope for a longer period of time. This mimics the inverse relationship between the distance of initial channel advance and slope demonstrated by Hoyal and Sheets (2009a). That all experiments were net progradational is not meant to imply that the depocenter was always progressing basinward in time (fig. 6.6B), but that in an overall sense the systems trended basinward (fig. 6.6A). Given that, it is of interest to consider over what sort of time scale the instantaneous forward/back behavior of individual cycles is effectively washed out and only the long-term behavior remains.

To consider this question, we did linear regression on the data in figure 6.6A over variable amounts of time as, $\widetilde{d_{clt}} = d_0 + \widetilde{u_{prog}}t$, where $\widetilde{u_{prog}}(t)$ is the time-dependent average rate of system progradation. $\widetilde{u_{prog}}$ was obtained for each value of t throughout the experiments by doing linear regression only on the data at and preceding t. The result is shown in figure 6.6C. There are two important times: where $\widetilde{u_{prog}}$ is never negative again and where $\widetilde{u_{prog}}$ begins to level off. For the former, $\widetilde{u_{prog}}$ is not negative after $t \approx 40$ min. This means that 40 min is an estimate of the amount of elapsed time needed such that the system would be viewed as overall progradational, i.e., the system moves forward enough that the movement backward does not make the system appear overall retrogradational. However, the effects of extension/backfilling cycles are still present in that there are oscillations in $\widetilde{u_{prog}}$. These oscillations are damped out and additional incremental data does little to change $\widetilde{u_{prog}}$ after $t \approx 200$ min. It was after this point in time that individual extension/backfilling cycles had little effect on the long-term average system trajectory, i.e., $\widetilde{u_{prog}}(t > 200) \approx \overline{u_{prog}}$.

Another way to consider the time evolution of the system is with mass balance using the known sediment supply rate, Q_s, and the known equilibrium slope, S_{eq}. In all our experiments $S_{eq} < S_p$ such that the domain was overall depositional. There was an angle, θ_{fan}, that describes the theoretical expansion half angle of the overall fan (see fig. 6.7 for definition sketch). The initial longitudinal slope of the domain is S_p, however if the direction of interest is not directly down-slope but is deflected by an angle of θ_{fan}, the slope is reduced to S_{eq}. Therefore θ_{fan} is the angle along which the system is effectively at equilibrium before the experiment starts and is given by $\theta_{fan} = \arccos(S_{eq}/S_p)$. Given this fan angle, the width of the fan, W_{fan}, at any distance x from the inlet is given as $W_{fan}(x) = W_0 + 2x\tan(\theta_{fan})$, where W_0 is the initial width. If the fan was at equilibrium before the experiment starts along the angle θ_{fan}, the system was furthest from equilibrium down the centerline of the basin. To reach equilibrium at each point a distance x from the inlet the system must fill a distance $H_{fill}(x) = (S_p - S_{eq})x$. From there, the cross-sectional area to be filled at each distance x from the inlet can be calculated as the section of a circle, $A(x) = R_{cir}(x)^2/2(\phi_{cir}(x) - \sin(\phi_{cir}(x)))$, where R_{cir} is the radius of the circular section given by $R_{cir}(x) = H_{fill}(x)/2 + W_{fan}(x)^2/(8H_{fill}(x))$, and ϕ_{cir} is the angle over which the circle circumscribing the deposit is above the initial sediment bed given by $\phi_{cir} = 2\arcsin(W_{fan}(x)/(2R_{cir}(x)))$. The volume within the equilibrium deposit is then, for any distance x from the inlet, $V_{fan}(x) = \int_0^x A(x)dx$. Using the known sediment supply rate, Q_s, the time required to fill to a particular point x is given by $T(x) = V(x)/Q_s$. This trend is shown on figure 6.6A. The relationship is not set to start at $x = 0$ at $t = 0$ but is instead started slightly offset downstream to account for the short ($\sim 10 - 20$ cm) clearing ahead of the inlet.

The mass balance curve lags both the linear regression and the data early in the experiment. The mass balance relationship assumes that the basin was filled in progressively from the inlet. This was not the case. The extension length of the

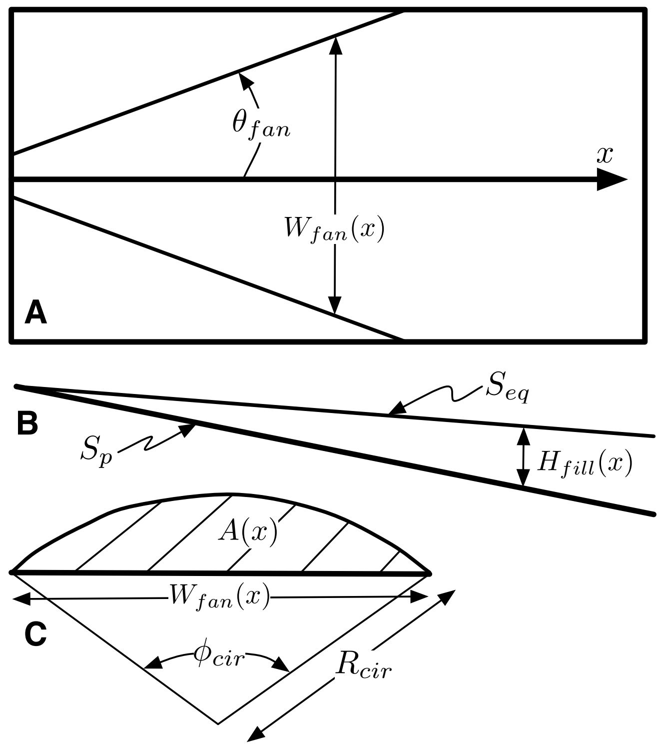

Figure 6.7: Definition sketch for mass balance basin filling: (A) plan view of basin, (B) longitudinal section of basin down the centerline, and (C) transverse section through the basin at any point x.

initial channel was typically to the middle of the plate or beyond and thus deposition commenced at a basinward location rather than just downstream of the inlet. Though initially set apart from the linear trend and data, the mass balance relationship catches up at $t \approx 200$ min for the example in figure 6.6A. Interestingly, this is approximately equivalent to the time were the individual avulsion cycles were washed out from the overall landform trend (fig. 6.6C). Therefore the time after which the effects of individual avulsion were overwhelmed by the overall system trend marked the transition to a landform building regime where the mass balance relationship works. Since the mass balance relationship is predicated on exclusive basinward extension, the primary implication is that most of the morphologic work was toward the fan front where the system was being incrementally advanced.

Compensational Stacking

To consider the propensity for compensational stacking, we ran a final experiment wherein the initial sediment bed was disturbed such that there was a large depression along the centerline of the domain near the slope break. The question was simple: would the system fill in the imposed depression first or just at some point during the experiment? Figure 6.8 shows a longitudinal and transverse profile through the middle of the depression with the bathymetry at 20 min increments up to 120 min. Interestingly, this depression is not the initial depocenter during the experiment. The first bathymetric scan to see any real change in morphology at this location was at $t = 80$ min. This is not statistically meaningful but offers an interesting look at how these supercritical fans fill space over time. Though the depression was located toward the middle of the domain, and was substantially lower than the surrounding sediment bed, it was not filled preferentially early during the experiment.

6.1.3 Variation in Hydraulic Properties

Here we look at the temporal and spatial variation in the hydraulic and sediment transport properties as F_r, τ^*, Q_t. As mentioned previously, the flow field can be generally delineated into the trunk channel, distributary channel, and lobe. The trunk channel is the area from the inlet unto the transition to a distributary channel or channels. The difference between the upstream trunk channel and the distributaries is that the distributary channels are narrower and deeper. The channel to lobe transition marks the transition from the well-defined distributary channel flow to the dispersed and unconfined over-lobe flow.

Figure 6.9 shows the hydraulic properties and slope of a single-channel configuration. This is a particular example that is indicative of single channel behavior during the various experiments. The slope starts just outside the inlet at the plate slope (fig. 6.9B). Flow was on the non-erodible plate for the first < 10 cm before transitioning to

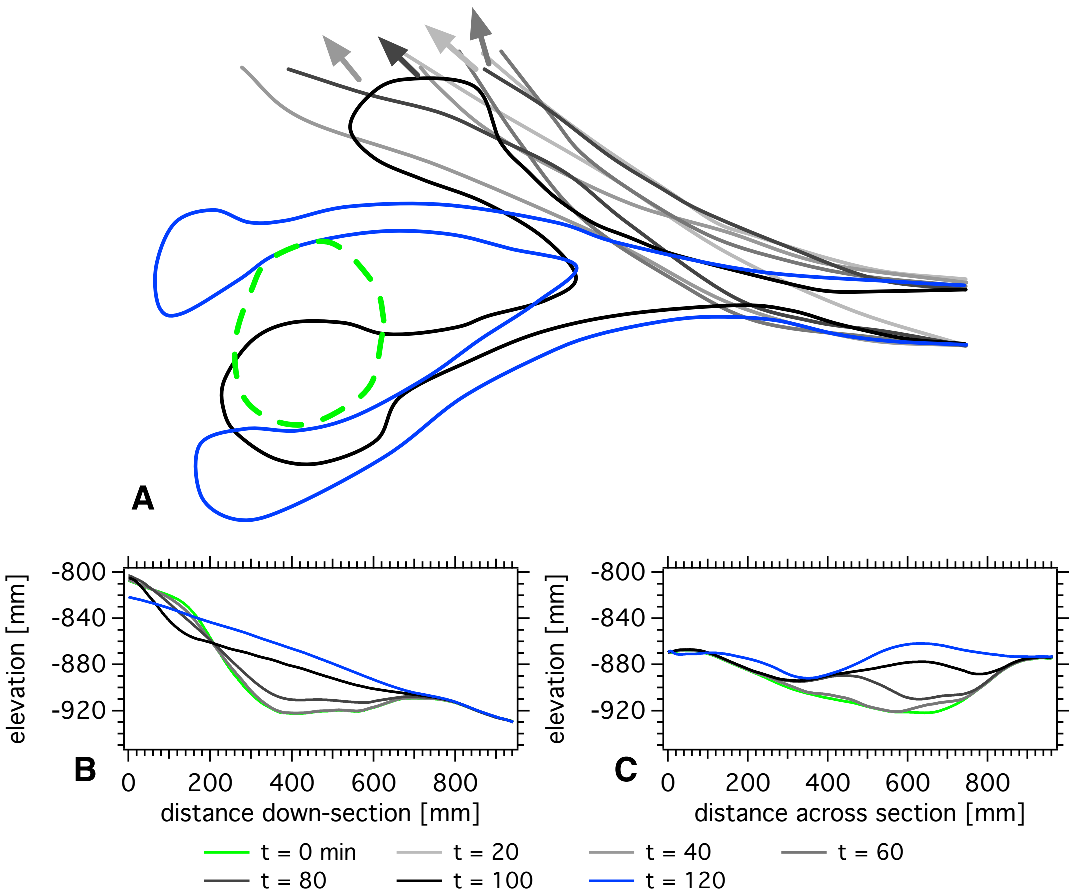

Figure 6.8: Overview of Fan10-B behavior: (A) plan view with the flow field marked, (B) longitudinal profile, and (C) transverse profile.

the self-formed channel with sediment substrate. From there, the channelized slope slightly increased in the downstream direction up until the channel-to-lobe transition where the slope began to decrease (fig. 6.9B). The slope hits a minimum in the mid-lobe region and the slope began to increase in the downstream direction on the basinward side of the lobe. The dramatic slope reduction shown in figure 6.9B toward the end of the plot is associated with the transition from perched lobe to the horizontal plate at the end of the domain.

The Froude number was gently modified along the channel in response to slope changes (fig. 6.9C). The sediment transport capacity was relatively constant along the channel before decaying through and ahead of the channel-to-lobe transition (fig.

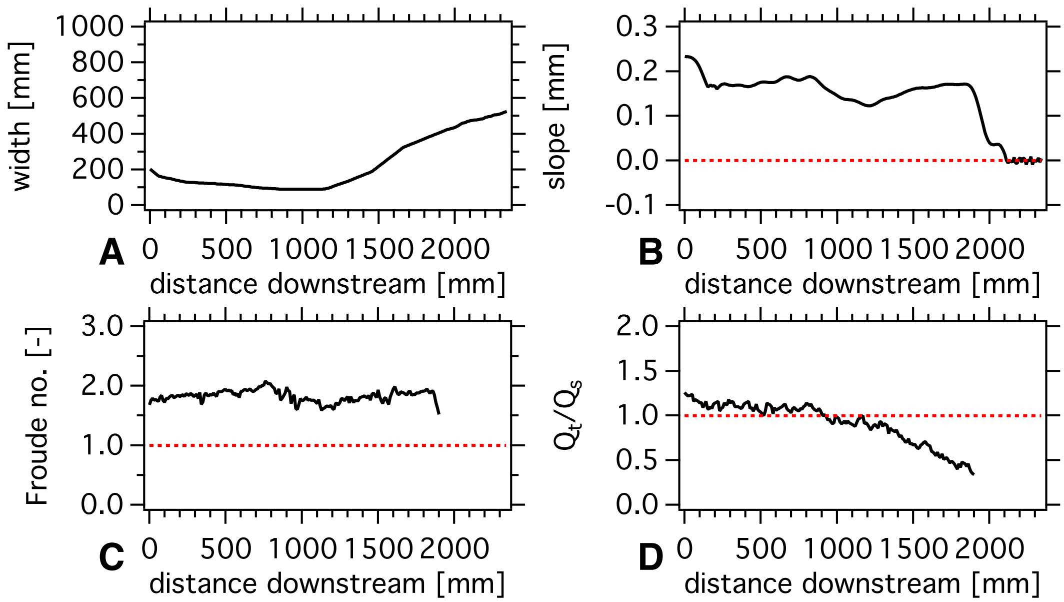

Figure 6.9: Hydraulic properties of the flow field for an example case of a single distributary channel: (A) flow width, (B) slope, (C) Froude number, and (D) ratio of sediment transport capacity to sediment supply.

6.9D). There was a region of higher Q_t/Q_s near the inlet where the flow was directly on the non-erodible plate. Through the self-formed channel there were two processes which counteracted each other to maintain a nearly constant Q_t/Q_s value at approximately bypass conditions: (1) reduction in Q_t due to ambient entrainment and (2) increase in Q_t due to increased velocity in response to increased slope. Both of these adjustments were slight and resulted in a net maintenance of Q_t in the downstream direction.

Figure 6.10 shows the hydraulic properties and slopes for a case with multiple distributary channels. There is a discontinuity in the curves at the trunk to distributary transition due to the relative fuzziness as to the exact location. The example shown in figure 6.10 is indicative of typical behavior throughout the various experiments, however the behavior was not as universal as that in the single channel case. There was much more variability due to the partitioning of hydraulic and sediment transport variables at the bifurcation. A Q_t/Q_s value can be calculated for these

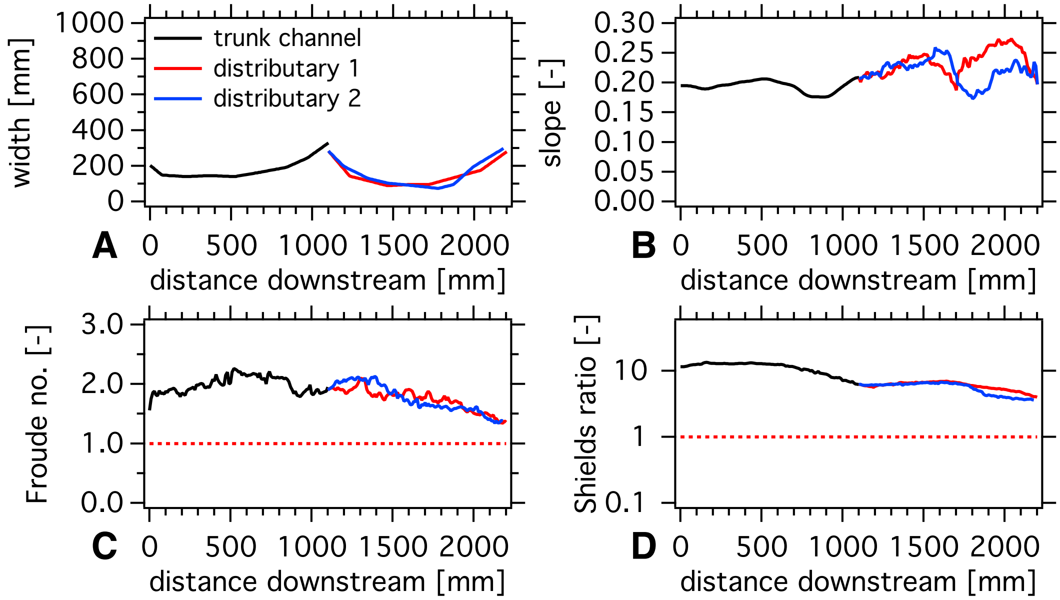

Figure 6.10: Hydraulic properties of the flow field for an example case of multiple distributary channels: (A) flow width, (B) slope, (C) Froude number, and (D) ratio of Shields stress to critical Shields stress.

channels, but for the case of multiple distributaries it can only be based on the Q_s values at the inlet. For the common case where there are multiple active distributaries incised on the fan front the sediment supplied to each was dependent on how much sediment was transported through the bifurcation since a portion is deposited, and how the remaining amount was partitioned between the active channels. The essentially unknown upstream boundary conditions preclude the existence of a typical hydraulic state for these fan-front distributaries. Since Q_t/Q_s values are difficult to determine reliably for the case of multiple distributaries, τ^*/τ^*_{cr} was plotted in figure 6.10D. As was the case with a single distributary, the distal portions of the fan retained sediment mobility, i.e., $\tau^*/\tau^*_{cr} > 1$, however there is solely deposition.

Whether there was a single or multiple distributaries active at a particular time, the over-lobe flow was similar. For most cases sediment remained mobile, i.e., $\tau^* > \tau^*_{cr}$, however the sediment transport capacity was far below sediment supply, i.e., $Q_t << Q_s$.

Experiments were not either single distributary or multiple distributary experiments. All experiments had periods of both. When there were multiple distributaries, the bifurcation was typically in the mid-fan region and the distributaries were formed on the steeper fan-front portion of the fan. The case of multiple active distributaries typically occurred later in the experiments while a single channel typically persisted early. The transition from multiple active distributaries to a single distributary happened quickly during the experiments and was not directly captured. There were two observed behaviors for transitioning to a single channel. The first was channel incision initiated from the upstream direction. This appeared to essentially be preferential treatment of a single distributary by the system, i.e., one distributary was better defined and eventually took over. Once the majority of flow was sent to the one channel, it would deepen and widen to accommodate the extra flow. The other observed behavior was headward erosion of one distributary channel that intersected the trunk channel and captured the flow. As mentioned, these behaviors occurred relatively quickly and were not captured in the data. These descriptions are based on observation during experiments.

6.2 DISCUSSION

6.2.1 Trends in Sedimentary Stacking

Experiments by Cantelli et al. (2011) exhibited cycles of extension and retreat but with an overall trend toward aggradation and progradation. This is qualitatively very similar to the observations in this study. Each avulsion cycle includes both extension and backfilling yet the overall trend was one of basinward progradation and aggradation. This is an important outcome given the mechanical differences between the studies - the Cantelli et al. (2011) fans used subcritical turbidity currents with copious suspension, while we used supercritical density currents dominated by bedload. These are fundamentally different hydraulic and sediment transport conditions that nevertheless give rise to similar landform response. The persistence of extension/backstepping avulsion cycles is not particularly surprising; the generic sequence of events during avulsion is similar regardless of hydraulic regime. The main difference is the presence of backwater in subcritical flows or hydraulic jumps in supercritical flows. This alters the spatial scale and depositional pattern expected during backfilling portions of the cycle; backwater will produce within-channel aggradational beds over longer scales while hydraulic jumps produce steeply inclined backset bedding over shorter scales.

As to the question of whether these systems behave compensationally, that the imposed bathymetric depression in the middle center of Fan10 was not filled immediately during the experiment is an interesting outcome. If the system would have been seeking the bathymetric low points, this region would certainly have been it. Distributary channel extension is a process which is initiated from the upstream direction. For supercritical flows, the extending channel has little information about the downstream conditions prior to reaching that location. In this way the extending channel is ignorant to the perturbed downstream bathymetry. The combination of a process initiated from the upstream direction and uninformed supercritical flow are perhaps reasons why a prominent downfan depression would not be preferentially filled early in the experiment. Though potentially not a flow attractor, a depression such as this could act to "lock in" the depocenter for a period while the depression is filled.

6.2.2 Preservation Potential

The complicating factor for any study of contemporaneous flow and deposit interaction is the potential for that deposit to be preserved. Deposits are subsequently reworked via avulsion and the sediment redistributed to different parts of the fan. The thickness of lobe deposits is typically much thicker than the channel body thickness of subsequently incised channels (fig. 6.11). Hydraulic jumps often mark the channel-to-lobe transition during the channel backfilling portion of supercritical avulsion cycles and are responsible for copious sedimentation (Hamilton et al., 2015a) (Chapter 4). The thickness of the lobes emplaced by hydraulic jump behavior roughly mimics the sequent depth of the jump (Hamilton et al., 2015b) (Chapter 5). The sequent depth is tied to the upstream flow thickness and upstream Froude number. As Froude number increases, the ratio between the maximum lobe thickness, H_l, and the upstream flow depth, h_1, also increases.

Subsequent channel incision has a depth similar to that of the channel that previously emplaced the lobe. This means that for a particular lobe deposited somewhere within the domain a thickness $H_l - h_1$ is preserved. Furthermore, because the width of the lob, W_l, is several times the flow width,W, only a portion of the previously emplaced lobe is dissected. An interesting implication is that as Froude number increases, sedimentary preservation should also increase. Since H_l/h_1 is Froude number dependent, and if we assume for comparison sake that h_1 is similar between two cases, the higher F_r, the greater multiple of h_1 H_l will be and the higher $H_l - h_1$ will be. As an example, consider two channel 25 m thick, one with $F_r = 1.2$ and one with $F_r = 1.5$. If we use the classic hydraulic jump equation to estimate H_l for both cases (eq. 2.15), we get H_l estimates of 31.8 m and 42 m respectively. Since h_1 is the same in both cases, $H_l - h_1$ is 10.2 m more in the case with the higher F_r and more of the previously deposited lobe is preserved.

6.2.3 Hierarchical Scale Considerations

Submarine fans are typically delineated into hierarchical elements (e.g., Deptuck et al., 2008; Prélat et al., 2010; Straub and Pyles, 2012). It is worth considering the hierarchical equivalent at field scales of sedimentary bodies deposited during our experiments. What we will consider is how different the different processes potentially

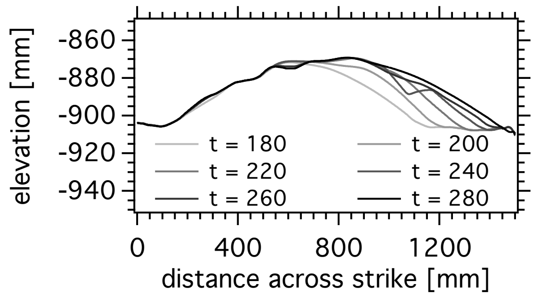

Figure 6.11: Strike section at various times during Fan03-B at $X = 2250$mm.

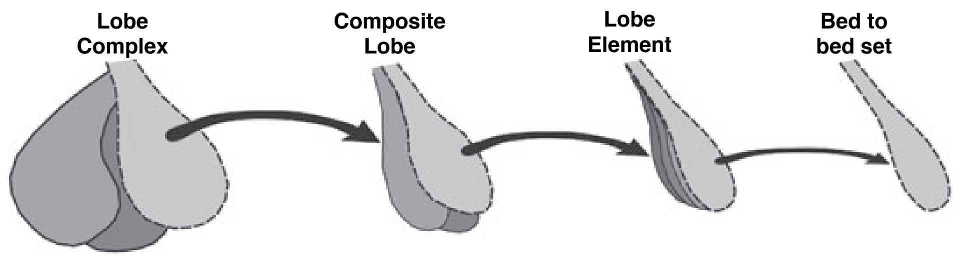

Figure 6.12: Planform schematic view of hierarchical terminology used by Deptuck et al. (2008) (after Deptuck et al., 2008).

translate to field scale based on process interpretations in the literature of the various hierarchical levels. This is to say that we will not be doing a dynamic similarity scaling procedure to consider the spatial or temporal scale of a similar field-scale equivalent, but looking at the processes involved.

Much of this discussion will be based on the process interpretation by Deptuck et al. (2008) of the Golo Fan system, as it is a system we think is similar to our laboratory scale experiments. We will also use their terminology. The progradational and aggradational deposits associated with the avulsion cycles are beds to bed sets (fig. 6.2). Lobe elements are depicted to include lateral accretionary beds which is indicative of the aggradation phase of the cycle. Additionally, the feeder channel rather stationary during over this scale. The main question is where in the bed to bed set, lobe element, and composite lobe spectrum does the hydraulic jump behavior fall. A signature of the experimental hydraulic jumps was backstepping and the remnant backset beds. Deptuck et al. (2008) observed this type of channel filling during composite lobe deposition, however since a composite lobe is a compilation of lobe elements, it could also be associated with the lobe elements. We do know based on lobe geometry work comparing the hydraulic jump sequent depth to maximum lobe thickness that the jump scaling works rather well for both lobe elements (such as the "proximal isolated lobes") as well as the composite lobes. To answer the question as to what scale of features are downstream of hydraulic jumps, it could be either lobe elements or composite lobes. Whatever the hierarchal level, we know in our experiments that the jumps all occur at the same level and only at that level. We also know that these experiments created 2-3 of the next higher hierarchical level.

The ambiguity regarding where exactly within a field-based hierarchy scheme these jumps exist is perhaps due to the constant flow nature of the experiments as well as the sole presence of autogenic dynamics. Since natural systems are often intermittent, sustain hydrographs of varying intensity and duration, and have variable sediment supply according to the hydrographs, lobe switching and transitions in scale are less clear cut than in a laboratory setting. Our experiments break out into 3 distinct scales based on the processes at work: (1) the bar scale, (2) the lobe scale, and (3) the lobe complex scale. The bar scale is associated with the progradational frontal splays and aggrading mouth bars. The lobe scale is associated with everything fed during a particular avulsion cycle, i.e., the bar scale plus everything after hydraulic jump formation but before avulsion and the lobe complex scale is essentially an amalgamation of lobes.

Chapter 7. Comparison of Avulsion Cycles from Subaerial and Subaqueous Fan Experiments with Supercritical Channels

7.1 OVERVIEW OF ALLUVIAL FAN EXPERIMENTS

To consider how similar or dissimilar subaerial and subaqueous avulsion cycles are, we compare data from experiments on alluvial (Hamilton, 2011; Hamilton et al., 2013) and submarine fan (Chapter 4) development. Both sets of experiments had constant boundary conditions such that the autogenic morphodynamic behaviors could be isolated without the influence of external variables. The data collected throughout the alluvial fan experiments were the same as the data types collected in this research.

There was a fundamental difference between these two sets of experiments in terms of setup that we will try to account for throughout this comparison. This was due to a difference in experimental objectives. The submarine fan experiments were run to expressly consider autogenic avulsion cycles and the experiments were relatively short (~ 1 hr). By contrast, the alluvial fan experiments (Hamilton et al., 2013) were run for an extended period of time and autogenic cycles were examined within the context of fan formation. The alluvial fan experiments were run with water and poorly sorted sediment ($d_{50} = 0.38$ mm) fed into a gently sloping basin initially devoid of sediment. The submarine fan experiments by contrast had much higher basin slopes and and the experimental domain was graded to a uniform thickness with sediment ahead of each experiment. The density contrast was created by dissolved salt and plastic sediment was used instead of silica sand to help with mobility (e.g., Metivier et al., 2005; Hoyal and Sheets, 2009a).

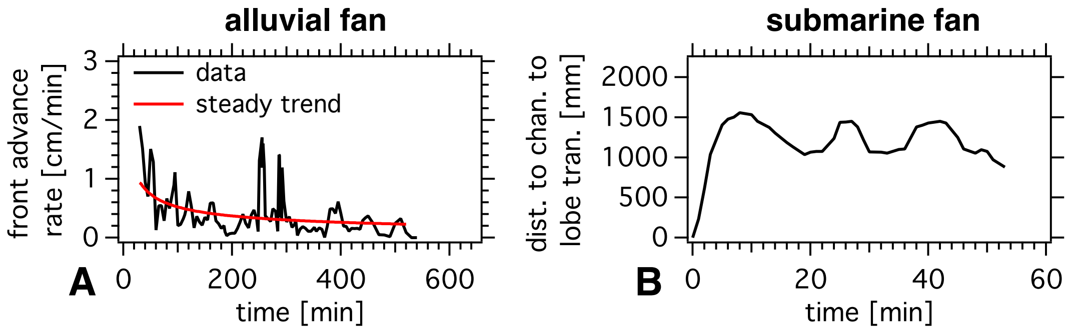

Figure 7.1: Evidence of cyclic behavior in: (A) alluvial fans as evidenced by pulses in the average fan front location and (B) submarine fans as shown by the advance and retreat in the distance from the inlet to the channel-to-lobe transition.

7.2 AVULSION CYCLE COMPARISON

7.2.1 General Overview

Herein we discuss the similarities and differences between the alluvial fan and submarine fan experiments. Long-term landform evolution can often be described based on an equilibrium slope and sediment discharge such that the landform, in an overall sense, incrementally fills its basin. However, below the resolution of such a macroscopic view, the landform is built by discrete avulsion cycles that redistribute sediment. Figure 7.1 shows an example of the temporal recurrence of cyclic behavior for the two experimental cases. One identifying signature for the alluvial fan case was oscillations in the fan front advance rate about the value which would otherwise be predicted sediment supply and a characteristic slope (fig. 7.1A). The landform does not build smoothly basinward, but is instead built over time by pulses of sediment delivered to the fan front (e.g., Kim and Jerolmack, 2008). Since the submarine case had a pre-graded sediment bed, the concept of a fan front is a little ambiguous. The time evolution of the distance between the inlet and the channel-to-lobe transition was tracked to demonstrate submarine cycles (fig. 7.1B).

Figures 7.2 and 7.3 show overhead images from a typical autocyclic event in the alluvial fan and submarine fan experiments respectively. The two cycles are similar in that they both exhibit the same generic sequence of events outlined in the introduction, i.e., channel formation, extension, stagnation, backfilling, and reorganization. Erosional channels incised into the existing sediment bed and extended basinward. Initial channel extension fed a frontal splay ahead of the distributary channel that eventually stagnated. At some point the extension ceased and the system began depositing a mouth bar. Lateral migration tended to occur as the channel ceased progradation as a way of filling space within the basin (figs. 7.2B, 7.3C). As the mouth bars aggraded they caused the system to begin to retreat upstream, i.e., the channel-to-lobe transition moved progressively back toward the inlet. After retreating upstream, the channel would avulse and reinitiate the cycle in a different location (fig. 7.2C-D, 7.3D-E).

7.2.2 Channel Hydraulics

Figure 7.4 shows example hydraulic and sediment transport conditions for the two cases while figure 7.5 shows an example cross-section of the channels themselves. The channels in each system are relatively similar. Because of the high slopes, both cases sustain supercritical flow ($F_r > 1$) (fig. 7.4A-B). In both cases the sediment transport capacity met or exceeded the sediment supply to the system (fig. 7.4C-D). This means that in neither case were the channels depositional unto themselves but transitioned to deposition beyond the channel-to-lobe transition. Both were bedload transport dominated systems with minimal suspension. This led to erosional channels which were incised into the pre-existing fan surface and did not have, or had very small, channel levees (fig. 7.5). In both cases the channelized flow had relatively steady and uniform flow conditions up to the channel-to-lobe transition. This makes sense for these supercritical flows as the behavior within the channel is only in response to the constant boundary condition signal from the upstream direction.

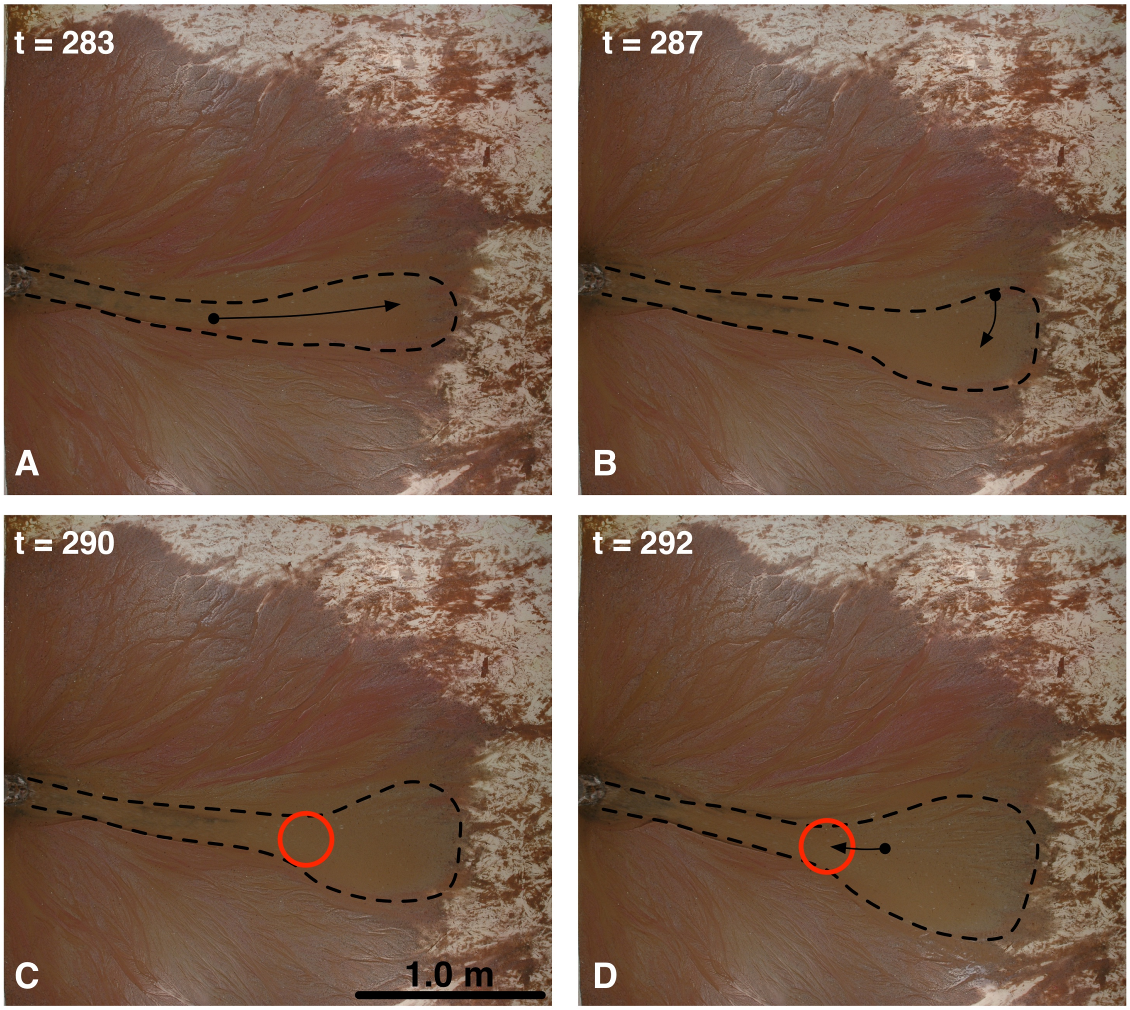

Figure 7.2: An overhead view of cyclicity in an alluvial fan experiment.

Since inertial forces exceed gravitational forces, waves are propagated solely downstream and supercritical flow has no information about the downstream boundary until getting to it.

The primary difference in the channel hydraulics is simply a product of the difference in ambient fluid density. Developing density currents entrain ambient fluid along their length such that, all other things equal, the current thickness, and therefore discharge, increase in the downstream direction. This is particularly significant for supercritical density currents were entrainment is more substantial than in subcritical density currents (Ellison and Turner, 1959; Parker et al., 1987). Ambient

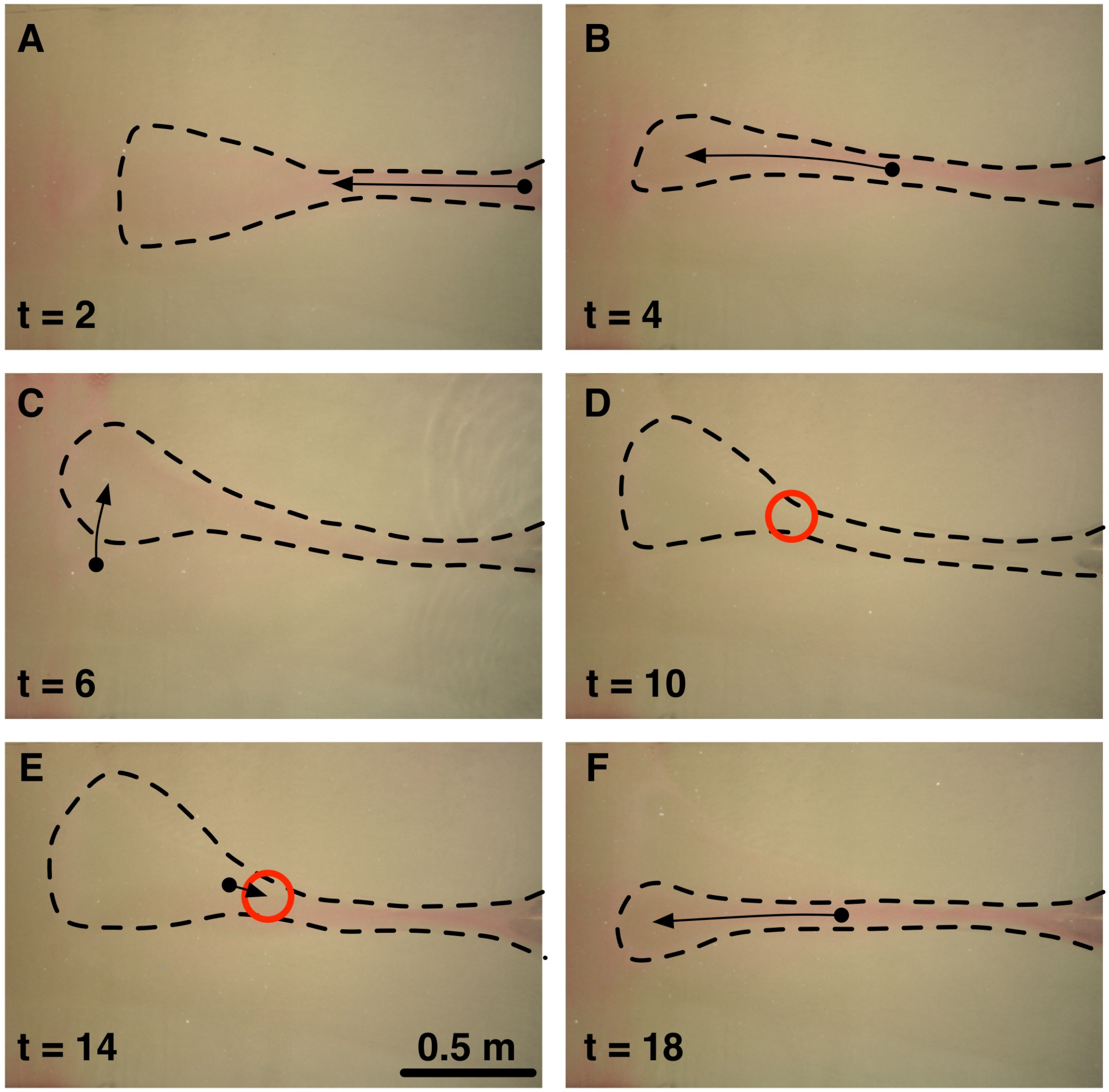

Figure 7.3: An overhead view of the typical cyclicity in a submarine fan experiment.

entrainment, though an important process, does not appear to have a profound impact on the downstream trajectory of the channel hydraulic variables (fig. 7.4B and D).

7.2.3 Initial Lobe Deposition, Migration, and Aggradation

Following distributary channel formation and basinward extension, at some point downstream the channels ceased extension and mouth bar deposition ensued. These mouth bars aggraded over time to lower the slope at the channel-to-lobe transition

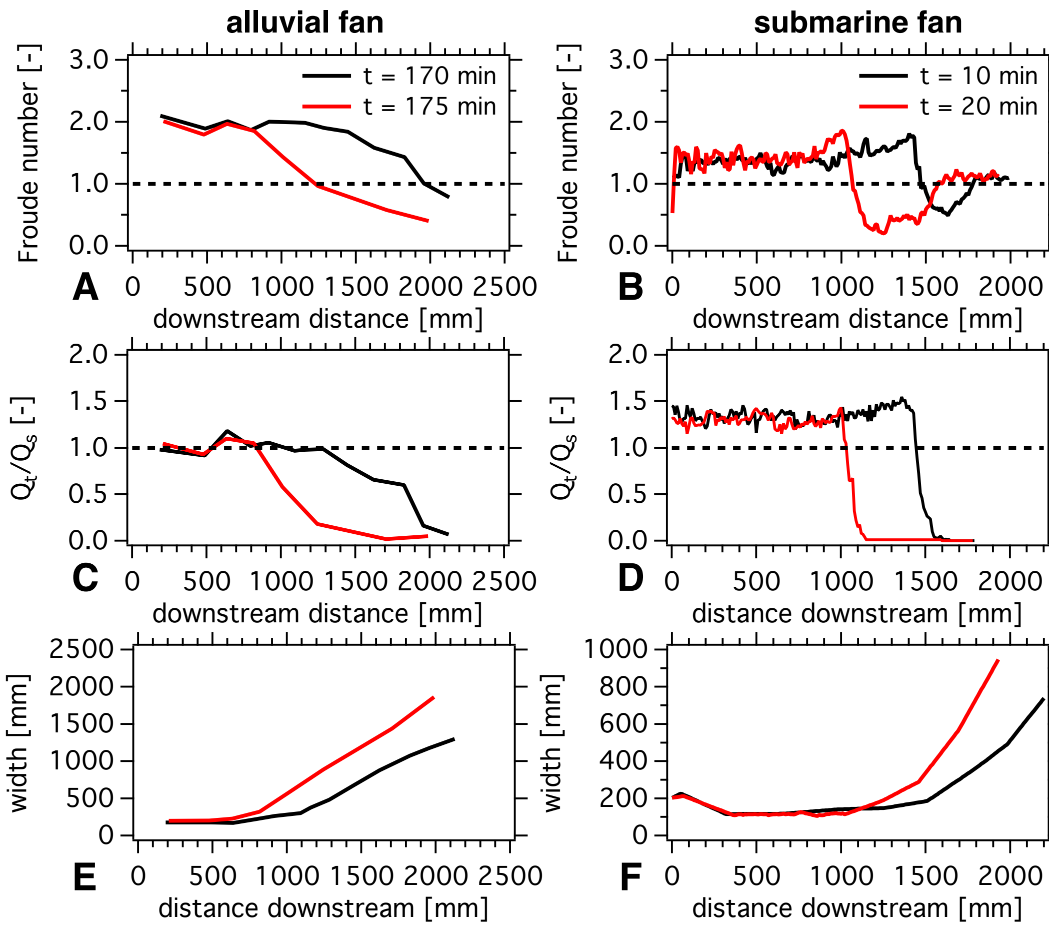

Figure 7.4: Downstream trends in hydraulic and sediment transport variables for two times during upstream retreat for an alluvial fan experiment (left side) and a submarine fan experiment (right side).

and created an obstacle to the flow. It was in this region of unchannelized flow downstream of the channel that both systems transitioned from erosion or bypass to deposition (fig. 7.4C-D).

The location of the channel-to-lobe transition was in both cases somewhere on the pre-existing fan surface and not at their respective slope breaks. This behavior was most apparent in the submarine fan experiments where the domain included a slope break that reduced the slope from the imposed basin slope to zero. Despite there being a dramatic slope break that would restrain the system, the system restrained itself on the imposed slope. This seemed to occur due to a reduced sediment transport

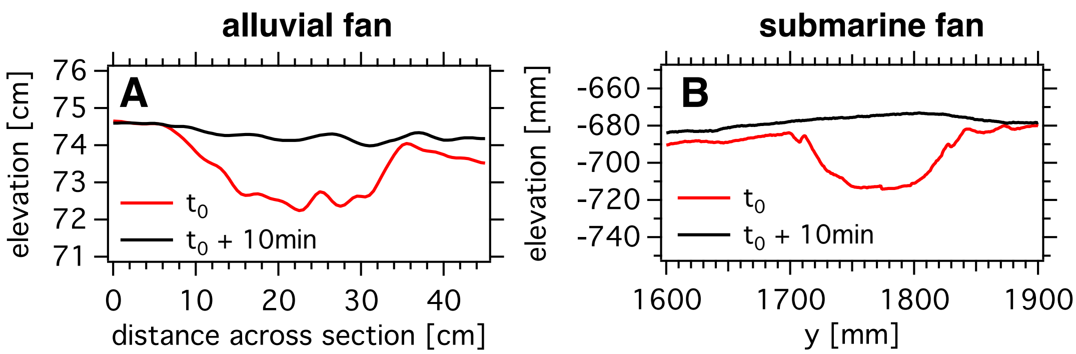

Figure 7.5: Proximal cross section showing erosional channels created by steep bedload dominated reaches for: (A) an alluvial fan and (B) a submarine fan.

capacity in the expanded flow region ahead of the extending channel. The transition from channelized flow to unchannelized flow for the alluvial fan case was associated with the difference in slope between the graded-channel slope and the prior overall fan slope. This made the transition from channelized flow to unchannelized flow typically occur somewhere on the fan surface rather than at the fan front where the slope transitions to the basin slope. Therefore in both cases the system restrained basinward extension and transitioned to deposition without an imposed transition in slope. There was some residual sediment transport that extends to the fan front in the alluvial fan case, if there were not the system would never move basinward, but the bulk of deposition was initiated before reaching the fan front.

The common process between the two cases was deceleration in the unchannelized flow field. The primary difference between the two cases, as was the situation for the channelized flow, was the presence of ambient entrainment in the subaqueous case. We know from equation 2.10 that $Q_t \propto U^3$, $Q_t \propto W$, and $Q_t \propto 1/R_s$. R_s is constant for subaerial flows, however changes in flow density make R_s dynamic for subaqueous flows and for conservative density currents will always act to decrease Q_t as R_s increases. This is an extra source of diminished sediment transport capacity, however deceleration appeared to be the dominant process in causing deposition.

After initial deposition in the expanded flow region, for both cases the lobes began to aggrade and commonly migrated laterally. This phase in the cycle acted to fill space ahead of the distributary channel. The aggraded lobe became an obstacle to the channelized flow and initiated retreat of the system back toward the inlet. An interesting aspect of these two systems, in contrast to deltas, is the absence of a downstream boundary condition. In this way the sedimentary system is free to set its own downstream boundary that it subsequently interacted with. For the subaqueous case the mechanism that initiated subsequent channel change was choked flow in the channel-to-lobe transition and the response was a hydraulic jump. Choked flow is the hydraulic condition where the specific energy available in a flow is insufficient to traverse an imposed obstacle, i.e., a step in bed elevation would cause the specific energy to drop below the critical specific energy.

As to whether there was a choked flow condition in the subaerial case, the answer is a little ambiguous. We know that the aggrading lobe deposits ahead of the channel built to a thickness sufficient for choked flow. It could have been a choked flow condition or another mechanism by which upstream retreat ensues. Unlike the subaqueous case where there was an obvious hydraulic jump marked by an abrupt reduction in Froude number (fig. 7.4B), the hydraulic transition was more gradual in the subaerial case (fig. 7.4A). Though not as dramatic of a transition as the subaqueous case, there was a transition from supercritical to subcritical flow nonetheless. It is within this zone of hydraulic transition where velocity was reduced via flow expansion and slope reduction to diminish sediment transport and causes deposition.

7.2.4 Upstream Retreat

After the channel extended basinward, aggraded the lobe ahead of the channel, and initiated hydraulic transition, the system retreated upstream as sediment was progressively deposited upstream of the initial obstacle. Figure 7.4 shows the propensity for these systems to feedback in the upstream direction via the hydraulic

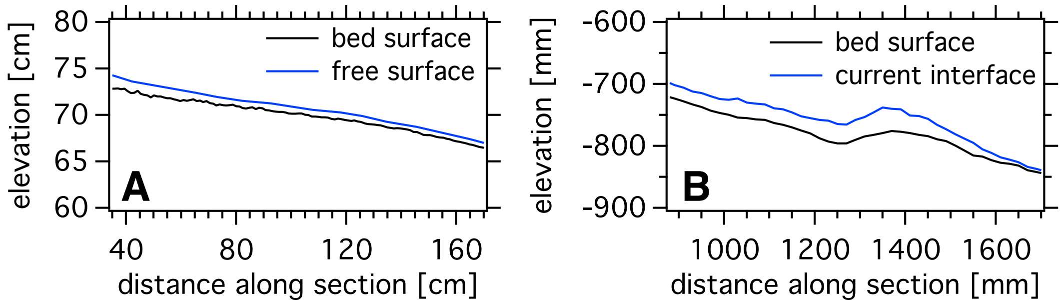

Figure 7.6: Longitudinal profile through the channel-to-lobe transition region for: (A) alluvial fans and (B) submarine fans.

and sediment transport variables. The aggraded mouth bar acts to impose a hydraulic transition that becomes an effective locus of deposition. This then forces the system to retreat upstream within each avulsion cycle. One point of contrast between the two environments is seen by zooming in on the transition region. Figure 7.6 shows longitudinal profiles of the sediment bed and water surface. As mentioned previously, the channel to lobe transition in alluvial fans (fig. 7.6A) was more subtle than in submarine fans (fig. 7.6B) both in the sediment bed and water surface. Since the transition to depositional lobe also entails transition from supercritical to subcritical flow (fig. 7.4A,B), the subtlety of hydraulic transition parallels the sedimentary transition. The abrupt transition realized in figure 7.6B is more indicative of a "classic" hydraulic jump in an open channel flume, i.e., a strong vertical disconnect in water surface.

Despite a difference in the hydraulic transition associated with the channel-to-lobe transition region, the channel fills associated with the backstepping were similar. A common signature for this type of channel infilling through supercritical retreat is a mounded deposit that can be described as the "steer-head" geometry. In this way the channels were completely infilled when passed over by the retreating channel-to-lobe transition. This effectively erased the channel as a topographic low on the fan surface.

The rate of backstepping was similar between the two experiments. The rate of channel-to-lobe transition retreat was in both cases a function of the sedimentary volume excavated by channel incision and basinward extension and sediment supply. Each cross-section through the channel had an area associated with in that was relatively constant along the downstream direction. As a particular point was backed over by the retreating channel-to-lobe transition, a cross-sectional area was filled with sediment, A_{fill}. Given the known sediment supply rate, Q_s, the rate of retreat was known to be $U_{fill} = Q_s/A_{fill}$. Since A_{fill} was relatively constant along the channel and Q_s was constant, U_{fill} remained relatively constant. This works because the system were very efficient in trapping sediment in the channel-to-lobe transition and therefore backfilling erosional features and maintaining upstream retreat.

7.2.5 Avulsion

The point and time of channel relocation differs between the two experiments. Alluvial fan experiments would go through a searching period between channel retreat and new channel initiation. This period seemed to be a way for the fan to aggrade itself to a slope where a channel could be incised. It was hypothesize that a small topographic depression would collect the flow and initiate a deepening feedback causing more and more flow to be collected. This renewed the cycle with channel extension.

The point of channel relocation behaved differently during submarine fan experiments. This was most likely due to the difference in experimental setup. The channels retreated upstream but always avulsed far before reaching the inlet. There was no searching period as in the alluvial fan experiments; new channel extension commenced as soon as retreat ended. The exact moment of avulsion was not captured experimentally though we hypothesize the mechanics to be similar to that of alluvial fans. It was common for new channels to form along the margin of the previous lobe. Because of the high transverse slopes, depositional lobes shed flow away from the longitudinal axis and toward the lobe margin. As flow collected along the margin it formed small erosional rills that deepened over time to collect more and more flow. These rills appeared to erode upstream and at some point intersect the distributary channel and capture the flow. This caused incision of a new channel and a new cycle of basinward extension followed by retreat.

Though the location of avulsion and sequence of events were different, both are hypothesized to be related to a deepening feedback triggered by small rill formation and flow collection. This behavior was hypothesized in both cases as channel incision happened rapidly compared to other portions of the cycle. Overall, though there is a difference in avulsion location, the mechanics of flow collection and new channel initiation seem to be similar.

Chapter 8. Conclusions

A series of submarine fan experiments were run to better understanding the underlying mechanics of the system and the landform response with time. Both the bathymetry and hydraulics were measured in time and space to investigate autogenic avulsion, lobe geometry, and longer-term fan evolution.

With respect to autogenic avulsion cycles, it was found that the cessation of channel extension was due to a drop in sediment transport capacity below sediment supply in the dechannelized flow regions ahead of a prograding channel. Reduced sediment transport capacity was primarily due to deceleration from the expansion and a slight lowering of the local channel slope as the channel progrades over previous frontal splay deposits. To a lesser extent, the decrease in capacity was further driven by ambient entrainment and the associated reduction in the buoyant force acting on the sediment. Following channel stagnation, the mouth bar deposited ahead of the channel aggraded over time to impose a choked flow condition and initiate a hydraulic jump. Once initiated, the jumps were maintained at the channel-to-lobe transition. Rapid deposition on the subcritical side of the jump results in the migration of both the channel-to-lobe transition and the jump upstream with time. This migration filled the channel with steep backset beds and capped the filled channel with a laterally expansive lobe. The interplay between the expansion-driven decrease in sediment transport capacity and the choke flow hydraulics allowed all but one of the set A experimental fans to be self-constructed above the basin slope break on a slope that naturally produced supercritical normal flow.

Each of the autogenic avulsion cycles are responsible for depositing an associated lobe. Lobe geometry has oft been cast as the inter-relationship between geometric properties or as a function of confinement. In terms of these more common relationships, correlations between L_l and W_l were similar between our experiments and other data sets across multiple scales. Other geometric relationships appeared particular to specific systems or spatial scales. Setting aside these type of purely geometric trends, we considered process-based relationships based on known avulsion mechanics. Avulsion cycles created lobe deposits comprised of three components: (1) thin progradational frontal splay deposits, (2) aggradational and laterally accreting mouth bar deposits that impose choked flow, and (3) hydraulic jump related deposits. The most significant source of deposition within each lobe was from the hydraulic jump. The ratio between maximum lobe thickness and upstream flow depth, H_l/h_1, persists as a function of upstream Froude number as dictated by the hydraulic jump experienced at the channel-to-lobe transitions. Since this relationship is based on conservation of momentum through rapidly varied flow, it is perhaps a scale and location independent relationship that can be applied in different environments. Though the "classic" hydraulic jump equation is not explicitly for density currents and the circumstances violate many of the assumptions, equation 2.15 works relatively well in representing H_l/h_1 as a function of F_r (fig. 5.4).

The conclusions thus far pertain to the properties of individual avulsion cycles. The set B series of experiments were run to investigate how supercritical submarine fan systems evolve over multiple avulsion cycles. Each cycles has progradational, aggradational, and retrogradational features. This forward/back behavior was evident over shorter time-scales but became washed out over longer times scales. Over longer time scales, all submarine fans were net progradational, i.e., the fans built basinward in an average sense. The trajectory of the system could be approximated by a mass balance approach that incorporates the sediment supply rate and the volume to be filled by the system based on the equilibrium slope. The F_r is manipulated over time in response to changes in slope and the system maintains sediment transport capacity at near the rate of sediment supply from the inlet up to the channel-to-lobe transition.

Finally, the autogenic avulsion cycles observed throughout this study were compared to similar cycles during alluvial fan experiments. Though the setting was different, both were supercritical systems with primarily bedload sediment transport. Both subaerial and subaqueous settings have a supercritical-to-subcritical flow transition in conjunction with their channel-to-lobe transitions but with two distinct flavors. Alluvial fans tended toward a more subtle transition region while submarine fans exhibited an abrupt hydraulic jump. Both alluvial and submarine fans demonstrated a propensity for upstream retreat during avulsion cycles. A majority of sediment was detained in the transition region that was progressively propagated upstream. One difference between the systems in terms of sediment transport relates to the above point regarding subtle versus abrupt transitions. Alluvial fans showed a continuous decay in Q_t/Q_s while submarine fans realize an abrupt drop at the hydraulic jump location. Furthermore, both systems show a propensity toward mounded channel fills above the banks of the incised channel. The cross-sectional area of this channel fill dictated the rate of channel-to-lobe transition retreat. This was similar between the two experiments as the as the sediment supplied to each system was constant and the channel-to-lobe transition detained significant sediment. Overall, the experimental data seems to indicate that the morphodynamic differences during avulsion cycles between alluvial and submarine fans with supercritical distributaries are relatively superficial given the overall mechanistic similarity. Both systems adhere to the generic avulsion cycle of channel extension, stagnation, aggradation, and upstream feedback with supercritical-to-subcritical transitions associated with channel-to-lobe transitions. These systems appear to be two flavors of the same cycle underpinned by similar mechanics. This lends credence toward the hypothesis that hydraulic regime is a more dominant control on autocyclic mechanics than subaerial or subaqueous environment.

References

Alexander, J. (2008). "Bedforms in Froude-supercritical flow." *Marine and River Dune Dynamics*.

Ashida, K. and Egashira, S. (1975). "Basic study on turbidity currents." *Proceedings of Japanese Society of Civil Engineers*, 37–50.

Brevis, W., Niño, Y., and Jirka, G. H. (2011). "Integrating cross-correlation and relaxation algorithms for particle tracking velocimetry." *Experiments in Fluids*, 50, 135–147.

Cantelli, A., Pirmez, C., Johnson, S., and Parker, G. (2011). "Morphodynamic and stratigraphic evolution of self-channelized subaqueous fans emplaced by turbidity currents." *Journal of Sedimentary Research*, 81, 223–247.

Carbonneau, P. E., Lane, S. N., and Bergeron, N. E. (2006). "Feature based image processing methods applied to bathymetric measurements from airborne remote sensing in fluvial environments." *Earth Surface Processes and Landforms*, 31, 1413–1423.

Carollo, F. G., Ferro, V., and Pampalone, V. (2007). "Hydraulic jumps on rough beds." *Journal of Hydraulic Engineering*, 133, 989–999.

Cartigny, M. J. B., Ventra, D., Postma, G., and van den Berg, J. H. (2014). "Morphodynamics and sedimentary structures of bedforms under supercritical-flow conditions: New insights from flume experiments." *Sedimentology*, 61, 712–748.

Chow, V. T. (1959). *Open-Channel Hydraulics*. The Blackburn Press.

Clauser, F. H. (1956). "The turbulent boundary layer." *Advances in Applied Mechanics*, 42, 1–51.

Covault, J. A. and Romans, B. W. (2009). "Growth patterns of deep-sea fans revisited: Turbidite-system morphology in confined basins, examples from the California borderland." *Marine Geology*, 265, 51–66.

Deptuck, M. E., Piper, D. J., Savoye, B., and Gervais, A. (2008). "Dimensions and architecture of late Pleistocene submarine lobes off the northern margin of east Corsica." *Sedimentology*, 55, 869–898.

Deptuck, M. E., Steffens, G. S., Barton, M., and Pirmez, C. (2003). "Architecture and evolution of the upper fan channel-belts on the Niger delta slope and in the Arabian Sea." *Marine and Petroleum Geology*, 20, 649–676.

Edmonds, D. A., Hoyal, D. C. J. D., Sheets, B. A., and Slingerland, R. L. (2009). "Predicting delta avulsions: Implications for coastal wetland restoration." *Geology*, 37(8), 759–762.

Ellison, T. H. and Turner, J. S. (1959). "Turbulent entrainment in stratified flows." *Journal of Fluid Mechanics*, 6, 423–448.

Ferguson, R. I. and Church, M. (2004). "A simple universal equation for grain settling velocity." *Journal of Sedimentary Research*, 74, 933–937.

Fernandez, R. L., Cantelli, A., Pirmez, C., Sequeiros, O., and Parker, G. (2014). "Growth patterns of subaqueous depositional channel lobe systems developed over a basement with a downdip break in slope: Laboratory experiments." *Journal of Sedimentary Research*, 84, 168–182.

Flint, S. S., Hodgson, D. M., Sprague, A. R., Brunt, R. L., Van der Merwe, W. C., Figueiredo, J., Prelat, A., Box, D., Di Celma, C., and Kavanagh, J. P. (2011). "Depositional architecture and sequence stratigraphy of the Karoo basin floor to shelf edge succession, Laingsburg depocentre, South Africa." *Marine and Petroleum Geology*, 28, 658–674.

Fujita, I., Muste, M., and Kruger, A. (1998). "Large-scale particle image velocimetry for flow analysis in hydraulic engineering applications." *Journal of Hydraulic Research*, 36(3), 397–414.

Fukuoka, S. and Fukushima, Y. (1980). "Mechanics of gravity currents advancing into stratified reservoir." *Proceedings of Japanese Society of Civil Engineers*, 65–77.

Garcia, M. and Parker, G. (1989). "Experiments on hydraulic jumps in turbidity currents near a canyon-fan transition." *Science*, 245, 393–396.

García, M. H. (1993). "Hydraulic jumps in sediment-driven bottom currents." *Journal of Hydraulic Engineering*, 119(10), 1094–1117.

M. H. García, ed. (2008). *Sedimentation Engineering: Processes, Measurements, Modeling, and Practice.* ASCE Manuals and Reports on Engineering Practice No. 110. ASCE.

García, M. H. and Parsons, J. D. (1996). "Mixing at the front of gravity currents." *Dynamics of Atmospheres and Oceans*, 24, 197–205.

Gervais, A., Savoye, B., Mulder, T., and Gonthier, E. (2006). "Sandy modern turbidite lobes: A new insight from high resolution seismic data." *Marine and Petroleum Geology*, 23, 486–502.

Gervais, A., Savoye, B., Piper, D. J. W., Mulder, T., Cremer, M., and Pichevin, L. (2004). "Present morphology and depositional architecture of a sandy confined submarine system: the Golo turbidite system (eastern margin of Corsica)." *Confined Turbidite Systems, Special Publication 222*, S. A. Lomas and P. Joseph, eds., Geological Society, London, 59–89.

Goring, D. G. and Nikora, V. I. (2002). "Despiking acoustic doppler velocimeter data." *Journal of Hydraulic Engineering*, 128(1), 117–126.

Gran, K. and Paola, C. (2001). "Riparian vegetation controls on braided stream dynamics." *Water Resources Research*, 37(12), 3275–3283.

Gray, T. E., Alexander, J., and Leeder, M. R. (2005). "Quantifying velocity and turbulence structure in depositing sustained turbidity currents across breaks in slope." *Sedimentology*, 52, 467–488.

Greimann, B., Lai, Y., and Huang, J. (2008). "Two-dimensional total sediment load model equations." *Journal of Hydraulic Engineering*, 134(8), 1142–1146.

Guy, H., Simons, D., and Richardson, E. V. (1966). "Summary of alluvial channel data from flume experiments, 1956-61." *Report No. 462-1*, USGS Professional Paper.

Hamilton, P. B. (2011). "Hydraulics and morphodynamics of autogenic cycles during subaerial fan development." M.S. thesis, University of Houston, Houston, TX.

Hamilton, P. B., Strom, K., and Hoyal, D. C. J. D. (2013). "Autogenic incision-backfilling cycles and lobe formation during the growth of alluvial fans with supercritical distributaries." *Sedimentology*, 60(6), 1498–1525.

Hamilton, P. B., Strom, K. B., and Hoyal, D. C. J. D. (2015a). "Hydraulic and sediment transport properties of autogenic avulsion cycles on submarine fans with supercritical distributaries." in review.

Hamilton, P. B., Strom, K. B., and Hoyal, D. C. J. D. (2015b). "Linking hydraulic properties in supercritical submarine distributary channels to depositional lobe geometry." in prep.

Hamilton, P. B., Strom, K. B., and Hoyal, D. C. J. D. (2015c). "Non-invasive methods for hydraulic characterization of density currents with application to submarine fan experiments." *Journal of Hydraulic Engineering*, 141(1), 06014018.

Hauet, A., Creutin, J. D., and Belleudy, P. (2008). "Sensitivity study of large-scale particle image velocimetry measurement of river discharge using numerical simulation." *Journal of Hydrology*, 349, 178–190.

Hetland, R. D. (2010). "The effects of mixing and spreading on density in near-field river plumes." *Dynamics of Atmospheres and Oceans*, 49(1), 37 – 53.

Hetland, R. D. and Macdonald, D. G. (2008). "Spreading in the near-field merrimack river plume." *Ocean Modelling*, 21, 12–21.

Holbrook, J. (2001). "Origin, genetic interrelationships, and stratigraphy over the continuum of fluvial channel-form bounding surfaces: an illustration from middle Cretaceous strata, southeastern Colorado." *Sedimentary Geology*, 144, 179–222.

Hooke, R. L. (1968). "Model geology: Prototype and laboratory streams: Disscussion." *Geological Society of America Bulletin*, 79, 391–394.

Hoyal, D., Van Wagoner, J., Adair, N., Deffenbaugh, M., Li, D., Sun, T., Huh, C., and Giffin, D. (2003). "Sedimentation from jets: A depositional model for clasic deposits of all scales and environments." *AAPG Search and Discovery*.

Hoyal, D. C. J. D. and Sheets, B. A. (2009a). "Hydraulic jumps as controls on the evolution of distributary channel networks on experimental submarine fans." *The 33rd International Association of Hydraulic Research Congress*.

Hoyal, D. C. J. D. and Sheets, B. A. (2009b). "Morphodynamic evolution of experimental cohesive deltas." *Journal of Geophysical Research*, 114, F02009.

Jegou, I., Savoye, B., Pirmez, C., and Droz, L. (2008). "Channel-mouth lobe complex of the recent Amazon fan: The missing piece." *Marine Geology*, 252, 62–77.

Johnson, S. D., Flint, S., Hinds, D., and De Ville Wickens, H. (2001). "Anatomy, geometry and sequence stratigraphy of basin floor to slope turbidite systems, Tanqua Karoo, South Africa." *Sedimentology*, 48, 987–1023.

Kennedy, J. F. (1969). "The formation of sediment ripples, dunes, and antidunes." *Annual Review of Fluid Mechanics*, 1, 147–168.

Kim, W. and Jerolmack, D. J. (2008). "The pulse of clam fan deltas." *Journal of Geology*, 116(4), 315–330.

Kleinhans, M. G., van Dijk, W. M., van de Lageweg, W. I., Hoyal, D. C. J. D., Markies, H., van Maarseveen, M., Roosendaal, C., van Wessep, W., van Breemen, D., Hoendervoogt, R., and Cheshier, N. (2014). "Quantifiable effectiveness of experimental scaling of river- and delta morphodynamics and stratigraphy." *Earth-Science Reviews*, 133, 43–61.

Kneller, B. and Buckee, C. (2000). "The structure and fluid mechanics of turbidity currents: A review of some recent studies and their geological implications." *Sedimentology*, 47, 62–94.

Kneller, B. C., Bennett, S. J., and McCaffrey, W. D. (1999). "Velocity structure, turbulence and fluid stresses in experimental gravity currents." *Journal of Geophysical Research*, 104(C3), 5381–5391.

Komar, P. D. (1971). "Hydraulic jumps in turbidity currents." *Geological Society of America Bulletin*, 82, 1477–1488.

Kostic, S., Parker, G., and Marr, J. G. (2002). "Role of turbidity currents in setting the foreset slope of clinoforms prograding into standing fresh water." *Journal of Sedimentary Research*, 72(3), 353–362.

Kostic, S., Sequeiros, O., Spinewine, B., and Parker, G. (2010). "Cyclic steps: A phenomenon of supercritical shallow flow from the high mountains to the bottom of the ocean." *Journal of Hydro-environment Research*, 3, 167–172.

Lajeunesse, E., Malverti, L., Lancien, P., Armstrong, L., Metivier, F., Coleman, S., Smith, C., Davies, T., Cantelli, A., and Parker, G. (2010). "Fluvial and submarine morphodynamics of laminar and near-laminar flows: a synthesis." *Sedimentology*, 57, 1–26.

Lofquist, K. (1960). "Flow and shear stress near an interface between stratified liquids." *Physics of Fluids*, 3(2), 158–175.

Luthi, S. (1981). "Experiments on non-channelized turbidity currents and their deposits." *Marine Geology*, 40, M59–M68.

Macdonald, R. G., Alexander, J., Bacon, J. C., and Cooker, M. J. (2009). "Flow patterns, sedimentation and deposit architecture under a hydraulic jump on a non-eroding bed: defining hydraulic jump unit bars." *Sedimentology*, 56, 1346–1367.

Mackin, J. H. (1948). "Concept of the graded river." *Geological Society of America Bulletin*, 59, 463–512.

Martin, J. E. and García, M. H. (2009). "Combine piv/plif measurements of a steady density current front." *Experiments in Fluids*, 46, 265–276.

Metivier, F., Lajeunesse, E., and Cacas, M. C. (2005). "Submarine canyons in the bathtub." *Journal of Sedimentary Research*, 75, 6–11.

Meyer-Peter, E. and Müller, R. (1948). "Formulas for bed-load transport." *Proceedings of the Second Meeting*, IAHR, Stockholm, Sweden, 39–64.

Miall, A. D. (1985). "Architectural-element analysis: A new method of facies analysis applied to fluvial deposits." *Earth-Science Reviews*, 22, 261–308.

Middleton, G. V. (1966). “Experiments on density and turbidity currets i: Motion of the head.” *Canadian Journal of Earth Sciences*, 3, 523–546.

Muste, M., Fujita, I., and Hauet, A. (2008). “Large-scale particle image velocimetry for measurements in riverine environments.” *Water Resources Research*, 44, W00D19.

Normark, W. R. (1970). “Growth patterns of deep-sea fans.” *The American Association ot Petroleum Geologists Bulletin*, 54(11), 2170–2195.

Normark, W. R. (1978). “Fan valleys, channels, and depositional lobes on modern submarine fans: Characters for recognition of sandy turbidite environments.” *The American Association of Petroleum Geologists Bulletin*, 62(6), 912–931.

Normark, W. R. and Piper, D. J. (1969). “Deep-sea fan-valleys, past and present.” *Geological Society of America Bulletin*, 80(9), 1859–1866.

Normark, W. R. and Piper, D. J. (1972). “Sediments and growth pattern of Navy deep-sea fan, San Clemente basin, California borderland.” *The Journal of Geology*, 80(2), 198–223.

Paola, C. (2000). “Quantitative models of sedimentary basin filling.” *Sedimentology*, 47(Suppl. 1), 121–178.

Paola, C., Straub, K., Mohrig, D., and Reinhardr, L. (2009). “The “unreasonable effectiveness” of stratigraphic and geomorphic experiments.” *Earth-Science Reviews*, 97, 1–43.

Parker, G., Fukushima, Y., and Pantin, H. M. (1986). “Self-accelerating turbidity currents.” *Journal of Fluid Mechanics*, 171, 145–181.

Parker, G., Garcia, M. H., Fukushima, Y., and Yu, W. (1987). “Experiments on turbidity currents over an erodible bed." *Journal of Hydraulic Research*, 25(1), 123–147.

Parsons, J. D., Schweller, W. J., Stelting, C. W., Southard, J. B., Lyons, W. J., and Grotzinger, J. P. (2002). "A preliminary experimental study of turbidite fan deposits." *Journal of Sedimentary Research*, 72(5), 619–628.

Posamentier, H. W. and Kolla, V. (2003). "Seismic geomorphology and stratigraphy of depositional elements in deep-water settings." *Journal of Sedimentary Research*, 73(3), 367–388.

Prélat, A., Covault, J. A., Hodgson, D. M., Fildani, A., and Flint, S. S. (2010). "Intrinsic controls on the range of volumes, morphologies, and dimensions of submarine lobes." *Sedimentary Geology*, 232, 66–76.

Prelat, A., Hodgson, D. M., and Flint, S. S. (2009). "Evolution, architecture and hierarchy of distributary deep-water deposits: a high-resolution outcrop investigation from the Permian Karoo Basin, South Africa." *Sedimentology*, 56, 2132–2154.

Reitz, M. D. and Jerolmack, D. J. (2012). "Experimental alluvial fan evolution: Channel dynamics, slope controls, and shoreline growth." *Journal of Geophysical Research*, 117, F02021.

Saller, A., Werner, K., Sugiaman, F., Cebastiant, A., May, R., Glenn, D., and Barker, C. (2008). "Characteristics of Pleistocene deep-water fan lobes and their application to an upper Miocene reservoir model, offshore East Kalimantan, Indonesia." *AAPG Bulletin*, 92(7), 919–949.

Schmeeckle, M. W. (2014). "Numerical simulation of turbulence and sediment transport of medium sand." *Journal of Geophysical Research: Earth Surface*.

Schmeeckle, M. W. and Nelson, J. M. (2003). "Direct numerical simulation of bedload transport using a local, dynamic boundary condition." *Sedimentology*, 50, 279–301.

Sequeiros, O. E. (2012). "Estimating turbidity current conditions from channel morphology: A Froude number approach." *Journal of Geophysical Research*, 117, C04003.

Sequeiros, O. E., Spinewine, B., Beaubouef, R. T., Sun, T., Garcia, M. H., and Parker, G. (2010a). "Bedload transport and bed resistance associated with density and turbidity currents." *Sedimentology*, 57, 1463–1490.

Sequeiros, O. E., Spinewine, B., Beaubouef, R. T., Sun, T., Garcia, M. H., and Parker, G. (2010b). "Characteristics of velocity and excess density profiles of saline underflows and turbidity currents flowing over a mobile bed." *Journal of Hydraulic Engineering*, 136(7), 412–433.

Sheets, B. A., Paola, C., and Kelberer, J. M. (2007). "Creation and preservation of channel-form sand bodies in an experimental alluvial system." *Sedimentary Processes, Environments and Basins: A Tribute to Peter Friend*, G. Nichols, E. Williams, and C. Paola, eds., number 38 in Special Publications of the International Association of Sedimentologists, Blackwell, 555–567.

Sittoni, L., Paola, C., and Voller, V. (2014). "Geometry, flow, and sediment transport of alluvial deposits by topographically driven flow expansions." *Journal of Sedimentary Research*, 84, 122–135.

Straub, K. M., Paola, C., Mohrig, D., Wolinsky, M. A., and George, T. (2009). "Compensational stacking of channelized sedimentary deposits." *Journal of Sedimentary Research*, 79, 673–688.

Straub, K. M. and Pyles, D. R. (2012). "Quantifying the hierarchial organization of compensation in submarine fans using surface statistics." *Journal of Sedimentary Research*, 82, 889–898.

Strom, K. B. (2014). "Inclusion of floc growth in a simple river mouth jet model and its effect on deposition rate." *Presented at 2014 EWRI Congress, Portland, OR, 1-5 Jun.*

Sumner, E. J., Peakall, J., Parsons, D. R., Wynn, R. B., Darby, S. E., Dorrell, R. M., McPhail, S. D., Perrett, J., Webb, A., and White, D. (2013). "First direct measurement of hydraulic jumps in an active submarine density current." *Geophysical Research Letters*, 40, 5904–5908.

Van Dijk, M., Postma, G., and Kleinhans, M. G. (2009). "Autocyclic behaviour of fan deltas: An analogue experimental study." *Sedimentology*, 56, 1569–1589.

Wahl, T. L. (2000). "Analyzing adv data using winadv." *2000 Joint Conference on Water Resources Engineering and Water Resources Planning and Management.*

Weill, P., Lajeunesse, E., Devauchelle, O., Métiver, F., Limare, A., Chauveau, B., and Mouaze, D. (2014). "Experimental investigation on self-channelized erosive gravity currents." *Journal of Sedimentary Research*, 84, 487–498.

Winn, R. J. and Dott, R. J. (1977). "Large-scale traction-produced structures in deep-water fan-channel conglomerates in southern Chile." *Geology*, 5, 41–44.

Wong, M. and Parker, G. (2006). "Reanalysis and correction of bed-load relation of meyer-peter and müller using their own database." *Journal of Hydraulic Engineering*, 132, 1159–1168.

Woods, A. W., Bursik, M. I., and Kurbatov, A. V. (1998). "The interaction of ash flows with ridges." *Bulletin of Volcanology*, 60, 38–51.

Wynn, R. B., Piper, D. J., and Gee, M. J. R. (2002). "Generation and migration of coarse-grained sediment waves in turbidity current channels and channel-lobe transition zones." *Marine Geology*, 192, 59–78.

Xu, J. P. (2010). "Normalized velocity profiles of field-measured turbidity currents." *Geology*, 38, 563–566.

Yu, B., Cantelli, A., Marr, J. G., Pirmez, C., O'Bryne, C., and Parker, G. (2006). "Experiments on self-channelized subaqueous fans emplaced by turbidity currents and dilute mudflows." *Journal of Sedimentary Research*, 76, 889–902.

Appendix A. One-dimensional Model Derivation

The 1D laterally expanding density current model is based on the steady-state layer-averaged conservation equations for mass, volume, and momentum using the Boussinesq approximation. Below we outline the steps used to arrive at equations 2.19-2.22. The primary integral qualities are thickness h, width W, density ρ_f, velocity, U, and entrainment velocity u_e. All of these quantities are taken as function of x. External constants include the density of the ambient fluid ρ_o, the acceleration of gravity g, and the bottom friction coefficient, $C_f = \tau_b/(\rho_f U^2)$. Rather than working directly with ρ_f, it is convenient to work with the density anomaly, $\Delta\rho = \rho_f - \rho_o$. In all cases, the cross section area of density current is assumed to be rectangular, and top-hat profiles are use for all flow variables and scalar qualities throughout the current.

The mass of the current changes in the downstream direction due to entrainment of ambient fluid. However, conservation of mass dictates that the buoyancy flux $Q\Delta\rho$ is constant along x

$$\frac{d(Q\Delta\rho)}{dx} = 0 \tag{A.1}$$

or

$$\Delta\rho\frac{dQ}{dx} = -Q\frac{d\Delta\rho}{dx} = 0. \tag{A.2}$$

Letting $Q = UhW$ and isolating the derivative for h results in,

$$\frac{dh}{dx} = -h\left(\frac{1}{\Delta\rho}\frac{d\Delta\rho}{dx} + \frac{1}{W}\frac{dW}{dx} + \frac{1}{U}\frac{dU}{dx}\right). \tag{A.3}$$

Conservation of volume requires that the flow thicken in the downstream direction for a constant width according to

$$\frac{dQ}{dx} = \frac{d(UhW)}{dx} = u_eW. \tag{A.4}$$

Combining eq. A.4 with eq. A.2 results in an expression for the change in $\Delta\rho$ with x,

$$\frac{d\Delta\rho}{dx} = -\Delta\rho\frac{u_e}{Uh}. \tag{A.5}$$

Note, that if the reduced gravity is defined as, $g' = (\Delta\rho/\rho_o)g$,

$$\frac{1}{\Delta\rho}\frac{d\Delta\rho}{dx} = \frac{1}{g'}\frac{dg'}{dx} \tag{A.6}$$

and eq. A.5 is equivalently expressed as

$$\frac{dg'}{dx} = -g'\frac{u_e}{Uh}. \tag{A.7}$$

The 1D steady-state layer-averaged momentum equation is

$$\frac{d(U^2hW)}{dx} = -\frac{d(g'h^2W/2)}{dx} + g'\frac{h^2}{2}\frac{dW}{dx} + g'hSW - \frac{\tau_b W}{\rho_o}, \tag{A.8}$$

where the bottom slope is , $S = -dz_b/dx$ and z_b is the bed elevation. This equation can be obtained by depth and width averaging the x momentum RANS equation with application of the kinematic boundary conditions and decomposition of the pressure into a dynamic pressure due the difference in density between the ambient and current. Additional assumptions embedded in eq. A.8 are that the ambient water is stagnant and that τ_b dominates over the longitudinal gradient of the depth-averaged shear stress in the xx direction. Expanding the first term on the left- and right-hand sides of eq. A.8 and canceling terms leads to

$$UhW\frac{dU}{dx} + U\frac{d(UhW)}{dx} = -g'Wh\frac{dh}{dx} - \frac{Wh^2}{2}\frac{dg'}{dx} + g'hSW - \frac{\tau_b W}{\rho_o}. \tag{A.9}$$

Inserting eq. A.4, dividing by hW, and rearranging gives

$$U\frac{dU}{dx} = -g'\frac{dh}{dx} - \frac{h}{2}\frac{dg'}{dx} + g'S - \frac{\tau_b}{\rho_o h} - \frac{Uu_e}{h}. \tag{A.10}$$

Noting eq. A.7, taking $\tau_b = \rho_o C_f U^2$ ($\rho_f/\rho_o \approx 1$), and rearranging further, one can obtain

$$\frac{dU}{dx} = -\frac{g'}{U}\frac{dh}{dx} + \left(\frac{hg'}{2U^2} - 1\right)\frac{u_e}{h} + \frac{g'S}{U} - \frac{C_f U}{h}. \tag{A.11}$$

Using eq. A.3 for dh/dx and the definition of the bulk Richardson number, $R_i = hg'/U^2$, the momentum equation can finally be expressed as

$$\frac{dU}{dx} = \frac{U}{1-R_i}\left[\left(1+\frac{R_i}{2}\right)\frac{1}{\Delta\rho}\frac{d\Delta\rho}{dx} + R_i\left(\frac{1}{W}\right)\frac{dW}{dx} + \left(R_i S - C_f\right)\frac{1}{h}\right]. \tag{A.12}$$

Eqs. A.3, A.5, and A.12 are the governing hydraulic equations for the 1D expanding density current model based on conservation of mass, volume, and momentum. To solve the equations, dW/dx must specified using either measured experimental data or an additional function. Two potential forms for the width function are

$$\frac{dW}{dx} = 2\tan\alpha_w \tag{A.13}$$

and

$$\frac{dW}{dx} = 2R_i^{1/2}. \tag{A.14}$$

Eq. A.13 defines width using a constant spread angle, α_w, and eq. A.14 defines the rate of spread with x based on the ratio of the current speed and the speed of the interface wave $\sqrt{g'h}$. Eq. A.14 has been found to adequately fit field-scale spreading of buoyant river mouth plumes (Hetland and Macdonald, 2008). To fully close the system, the entrainment velocity musts be specified in terms of other integral parameters. Here we use the following classic formulation of

$$u_e = e_w U, \tag{A.15}$$

where

$$e_w = \frac{\alpha}{(1 + 718 R_i^{2.4})^{0.5}} \tag{A.16}$$

with $\alpha = 0.075$ (Parker et al., 1987). The resulting set of equations (eq. A.3, A.5, and A.12) along with an expression or measured data for dW/dx, eqs. A.15 and A.16, and appropriate boundary conditions can be used to solve for $\Delta\rho$, W, U, and h along the x either within a channel or expanding flow section. In addition, rather than defining a constant slope, S, experimental bed elevation data can be used to define $S = S(x) = -dz_b/dx$.